2-22-2014

Novel Metamaterials and Their Applications in Subwavelength Waveguides, Imaging and Modulation

Wangshi Zhao

R.I.T

NOVEL METAMATERIALS AND THEIR APPLICATIONS IN SUBWAVELENGTH WAVEGUIDES, IMAGING AND MODULATION

by

WANGSHI ZHAO

A dissertation submitted in partial fulfillment of the requirements
for the degree of Doctorate of Philosophy in Microsystems Engineering

Microsystems Engineering Program
Kate Gleason College of Engineering

Rochester Institute of Technology
Rochester, New York
FEBRUARY 22, 2014

Novel Metamaterials and Their Applications in Subwavelength Waveguides, Imaging and Modulation

By

Wangshi Zhao

Committee Approval:

We, the undersigned committee members, certify that we have advised and/or supervised the candidate on the work described in this dissertation. We further certify that we have reviewed the dissertation manuscript and approve it in partial fulfillment of the requirements of the degree of Doctor of Philosophy in Microsystems Engineering.

Dr. Zhaolin Lu _____
Committee Chair and Dissertation Advisor Date

Dr. Bruce W. Smith _____
Date

Dr. Jayanti Venkataraman _____
Date

Dr. Stefan F. Preble _____
Date

Dr. Behnaz Ghoraani _____
Date

Certified by:

Dr. Bruce Smith _____
Director, Microsystems Engineering Program Date

Dr. Harvey J. Palmer _____
Dean, Kate Gleason College of Engineering Date

ABSTRACT

Kate Gleason College of Engineering
Rochester Institute of Technology

Degree: Doctor of Philosophy **Program:** Microsystems Engineering

Authors Name: Wangshi Zhao

Advisors Name: Zhaolin Lu

Title: Novel Metamaterials and Their Applications in Subwavelength Waveguides, Imaging and Modulation

The development of metamaterials has opened the door for engineering electromagnetic properties by subwavelength artificial "atoms", and hence accessing new properties and functionalities which cannot be found among naturally occurring materials. In particular, metamaterials enable the flexibility of independently controlling the permittivity and permeability to be almost any arbitrary value, which promises to achieve deep subwavelength confinement and focusing of electromagnetic waves in different spectrum regimes. The next stage of this technological revolution will be focused on the development of active and controllable metamaterials, where the properties of the metamaterials are expected to be tuned by external stimuli. In this sense, some natural materials are also promising to provide the tunable capability, particularly in the near infrared and terahertz domains either by applying a voltage or shining light on the materials. The objective of this dissertation is to investigate novel metamaterials and explore three important applications of them: subwavelength waveguiding, imaging and modulation. The first part of this dissertation covers the theory, design and fabrication of several different types of metamaterials, which includes artificially designed metamaterials and some naturally existing materials. The second part demonstrates metal gratings functioning as designer surface plasmonic waveguides support deep subwavelength surface propagation modes at microwave frequency. The third part proposes multilayered metal-insulator stack as indefinite metamaterial that converts evanescent waves to propagating waves, hence deep subwavelength image can be observed. The fourth part explores the tunability of several natural materials – gallium (Ga), indium tin oxide (ITO) and graphene, and demonstrates electro-optical (EO) modulators based on these materials can be achieved on nano-scale. The final part summarizes the work presented in this dissertation and also discusses some future work for photodetection, photovoltaics, and modulation.

ACKNOWLDEDGMENTS

I felt so fortunate to be surrounded by many loving people and now it is my pleasure to thank all of them for their love, encouragement, support and blessings.

First of all, I would like to express my sincerest gratitude to my advisor Professor Zhaolin Lu, for his valuable guidance and generous support throughout my entire graduate studies at RIT. His pioneering vision in optical science, abundance of knowledge and hard-working spirit inspired and motivated me. Without his insightful suggestions and persistent help, this dissertation would not have been possible.

I would like to express my deepest appreciation to Professor Bruce W. Smith, Professor Jayanti Venkataraman, Professor Stefan F. Preble, and Professor Behnaz Ghoraani for serving as my dissertation committee, willing to share their invaluable opinions and their useful critiques on my research.

I would like to thank the staff members in the Semiconductor & Microsystems Fabrication Laboratory (SMFL), especially Mr. Sean O'Brien and Mr. Bruce Tolleson. Their willingness to give their time and help so generous have been appreciated. At the same time, I would like to thank the staff members at Cornell NanoScale Science & Technology Facility (CNF), especially Mr. Aaron Windsor. For his expertise and instruction to me. My grateful thanks are also extended to Professor Karl Hirschman and Ms. Patrica Meller, for their kindness and help to me.

I want to express my gratitude to Dr. Ruoxi Yang, Dr. Rami Wahsheh, Mr. Andrew Estroff and Mr. Liang Cao, for their help in offering me useful technical discussions. Special thanks should be given to Ms. Fan Yang and Mr. Chih-Yu Jen. As my best friends, they gave me encouragement all the time and accompanied me during my ups and downs.

Finally, I would like to express my appreciation to my dearest parents, Mr. Zongpei Zhao and Ms. Shuwen Liu. Thanks for their unconditional love to me, trust me and always being on my side.

TABLE OF CONTENTS

LIST OF FIGURES

LIST OF TABLES

LIST OF ACRONYMS

AFM ..... Atomic Force Microscopy

ATR..... Attenuated Total Reflection

AZO ..... Aluminum-doped Zinc Oxide

CVD ..... Chemical Vapor Deposition

DSP ..... Designer Surface Plasmon

DUV ..... Deep Ultraviolet

EA ..... Electro-Absorption

EM..... Electromagnetic

EMT ..... Effective Medium Theory

ENZ..... Epsilon-Near-Zero

EO ..... Electro-Optic

FDTD ..... Finite-Difference Time-Domain

FWHM ..... Full Width at Half Maximum

ITO..... Indium Tin Oxide

MMI ..... Multilayer Metal-Insulator

NIMs ..... Negative Index Metamaterials

NIR..... Near-Infrared

PEC ..... Perfect Electric Conductor

PECVD ..... Plasma-Enhanced Chemical Vapor Deposition

SPPs ..... Surface Plasmon Polaritons

SRRs ..... Split Ring Resonators

TCOs ..... Transparent Conductive Oxides

TE..... Transverse Electric

TM..... Transverse Magnetic

TMM ..... Transfer-Matrix Method

VNA ..... Vector Network Analyzer

1 INTRODUCTION

1.1 Motivation

Electromagnetic (EM) metamaterials, with their extraordinary properties which cannot be obtained in most naturally existing materials, have been shown tremendous potentials in many fields of science and technology. Many scientific breakthroughs, for example, invisible cloaking [1-3] and super lenses [4-7], have been experimentally demonstrated with metamaterials. Generally, metamaterials can be treated as effective media, where their extraordinary properties depend on their periodic structure rather than their composition [8]. The periodicity of each unit cell in a metamaterial is significantly smaller than the wavelength of interest. Therefore, each unit can be viewed as a microscopic building block of the metamaterial, in analogy to the atoms in the naturally occurring conventional materials. Figure 1.1 illustrates a three-dimensional (3D) flat lens and its unit cell, with which subwavelength resolution imaging can be observed at microwave frequency regime [9].

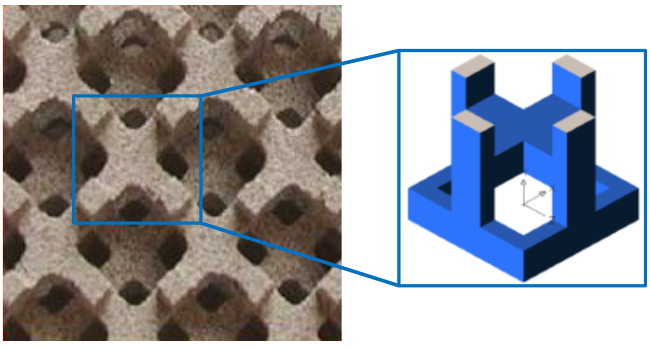

Figure 1.1 A three-dimensional metamaterial and its unit cell, where the unit cell is arranged in a body-centered-cubic structure. [9]

The history of metamaterials dates back to 1968, when a Russian scientist, Veselago, theoretically investigated [10] the electromagnetic consequences of a material which has both negative ε and negative μ, and made a conclusion that the refractive index of the material should be revised and expressed as $n = -\sqrt{\varepsilon\mu}$. Materials with negative refractive index *n* have numerous interesting applications and many classical physical phenomena associated with EM wave propagation need to be reexamined. For example, Doppler shift is reversed, and Cherenkov radiation is emitted in the opposite direction to the charge's motion rather than in the forward direction [10]. However, Veselago's theoretical work on the negative refractive index material had not been experimentally demonstrated for a long time since materials with negative index do not exist in nature. In 1990s, John B. Pendry and his colleagues proposed, for the first time, to use artificial materials to realize negative permittivity [11] and negative permeability [12], which opened up a completely new research area -- metamaterials.

At the early stage, the research on metamaterials was focused on microwave region to demonstrate negative refractive index [13] and superlenses [14]. In recent years, most efforts were focused on the engineering and extension of the functionalities of metamaterials at terahertz [16-18] and optical [5,13,19,20] frequencies. More recently, researchers focus on the metamaterial design which leads to the realization of tunability in metamaterials [19,21,22]. Tunable metamaterials are designed for switching and modulating EM waves if the properties of the metamaterials can be controlled by applying external stimulus. Some natural materials, such as graphene and transparent conductive oxides (TCOs), have already shown their outstanding properties as tunable metamaterials [23-25]. In this dissertation, I have explored the field of novel metamaterials and addressed three important applications of metamaterials: subwavelength waveguiding, imaging and modulating. These applications have been explored in an integrated

approach: starting from a fundamental study of subwavelength waveguiding with a designer surface plasmon (DSP) waveguide at microwave frequency regime, then extending the exploration to imaging beyond diffraction limit and modulating at optical frequencies.

1.2 Metamaterials

From a theoretical concept proposed several decades ago, the research on the topic of metamaterials is now rapidly expanding. With the fast development of nano-fabrication techniques, metamaterial are not limited to the microwave region, more complex structures working at higher frequencies can be fabricated and a wider range of materials can be selected. In this section, several different types of metamaterial designs, as well as their properties and applications will be introduced.

1.2.1 Background

Materials play key roles in the development of optics and photonics, since the main objective in these fields is to obtain the control on light propagation and light-matter interaction. In a conventional material, the propagation of light is influenced by the local refractive index $n = \sqrt{\varepsilon\mu}$. The EM response of a metamaterial can be described with two frequency-dependent macroscopic parameters, permittivity $\varepsilon(\omega)$ and permeability $\mu(\omega)$. Figure 1.2 shows a "material parameter space", which includes all types of materials, as far as EM properties are concerned. Region I represents materials with both permittivity and permeability positive, which covers most conventional dielectric materials. Region II includes metals and heavily doped semiconductors, which exhibit negative permittivity at some frequency regimes. In the microwave spectrum regime, negative permittivity can also be achieved by artificially designed wire structures [11] as illustrated in the top left. The first man-made material with negative permeability is the split ring resonators (SRRs) [12], as shown in the top right of region IV. Region III is the most interesting one, in which

permittivity and permeability are simultaneously negative. No such material can be found in nature. The representative negative index metamaterial (NIM) at microwave frequency is constructed by the SRRs and metallic wires [15]. On the subwavelength scale, the electric and magnetic fields are decoupled, so the permittivity $\varepsilon(\omega)$ could be the only parameter to be considered to fulfill the requirements of the metamaterials with desired EM properties, while disregarding the permeability $\mu(\omega)$. In this dissertation, the focus will be put on the manipulation of the frequency-dependent permittivity $\varepsilon(\omega)$, and the related novel metamaterial designs as well as their properties and applications.

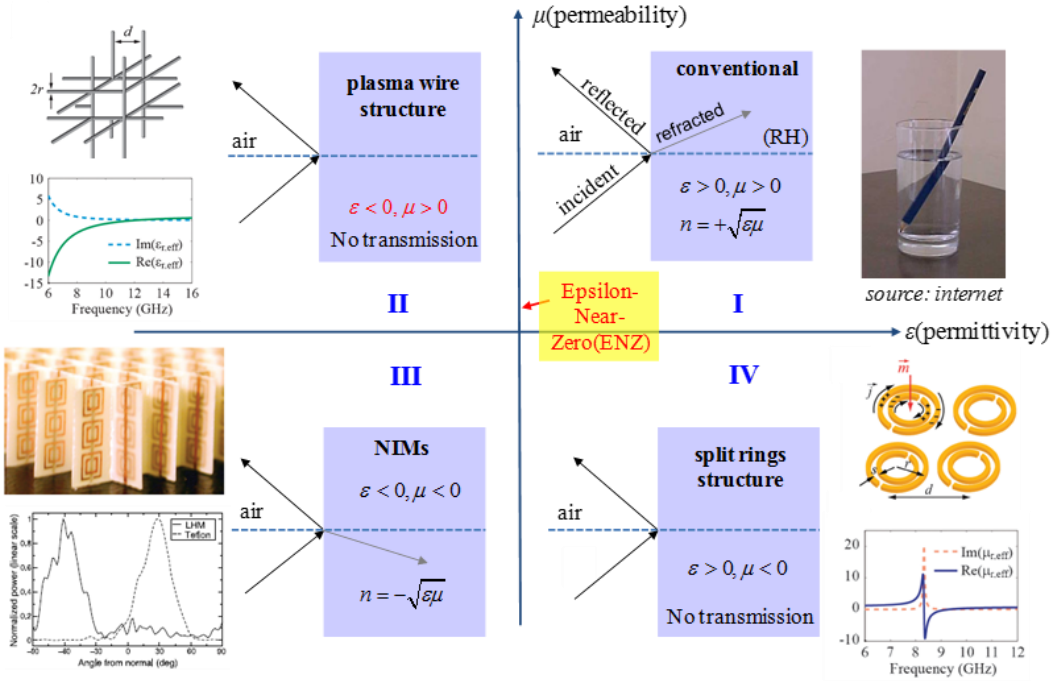

Figure 1.2 Material parameter space. [11,12,15]

One of the greatest potentials of metamaterials is the possibility to create negative refractive index, and the associated application is super lenses with imaging resolution beyond the diffraction limit [4]. Besides the negative refractive index, advanced developments in metamaterials [11,12,14,15,26] promise unprecedented flexibility in providing the artificial

materials with very complex specifications, including independent control of the permittivity and permeability with positive, negative, or near zero values, and with desired anisotropy and designed gradients. Tunable metamaterials attract more attention in recent years since they show variable response to an incident light beam, hence they are promising candidates to achieve nanometer-scale modulators on chip. The tunability of metamaterials has been demonstrated with different approaches, for example, electrically or optically pumping the semiconductor constituent of the metamaterials [21,22], and external DC magnetic field tuning [19].

One of the significant challenges researchers have to face is the high loss in the metamaterials at telecommunication and optical frequencies, which is usually caused by the metals, metal alloys or heavily doped semiconductors in those metamaterials. These large losses seriously limit the practicality of metamaterials for many novel applications, which is also a major obstacle in the design of efficient devices. Hence, new materials with relatively low loss are desirable. The introduction of alternative materials, for example, graphene and transparent conductive oxides (TCOs), can overcome the major bottleneck and improve the performance of the devices. Graphene, the two-dimensional atomic crystal, combines its exceptionally high electronic and thermal conductivities, as well as many other supreme properties, all of which make it highly attractive for numerous applications. The carrier concentration in TCOs is in the range of 10^{20}~10^{21}/cm^3, which will shift the plasma frequency into the near infrared (NIR) regime for telecom applications.

1.2.2 Negative refraction and subwavelength imaging

The original interest in metamaterials was triggered by Pendry's work in 2000 [4], where he claimed "negative refraction makes perfect imaging". In a conventional medium, the maximum resolution of an image cannot be smaller than the diffraction limit, because the evanescent waves

which carry the subwavelength feature information decay exponentially in that medium. However, in a metamaterial with a negative refractive index, the amplitudes of the evanescent waves can be amplified [4]. After emerging from the medium, the amplitudes will reach to the original level [27], as shown in Fig. 1.3(a). The propagating waves pass through the NIM with both negative refraction and a reversed phase front [as shown in Fig. 1.3(b)], which leads to zero phase change at the image plane [27]. Therefore, both propagating and evanescent waves are recovered in phase and amplitude, and a perfect image can be obtained.

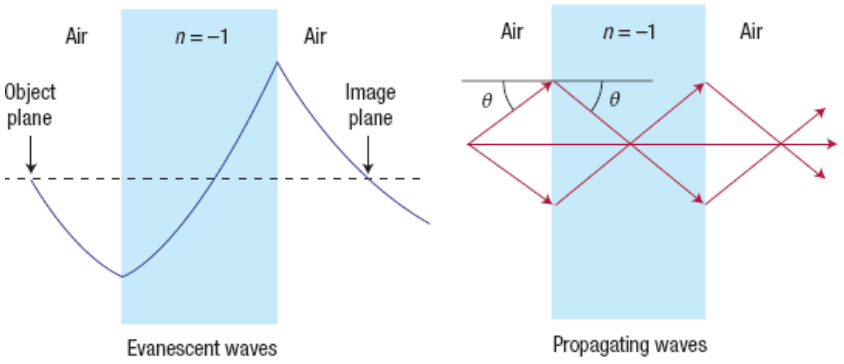

Figure 1.3 (a) Evanescent waves can be enhanced by a negative refractive index metamaterial, so the amplitudes of the evanescent waves are identical at the object and the image plane. (b) Propagating waves in the metamaterial. [27]

Metamaterials with negative permittivity or permeability or both can be used as a superlens in the form of a thin slab, which has been experimentally demonstrated at microwave [6], mid-infrared [7], and optical frequencies [5] with different designs, as shown in Fig. 1.4. The planar transmission-line lens, as shown in Fig. 1.4 (a), consisting of a grid of printed metallic strips loaded with series capacitors and shunt inductors, can form a subwavelength image of 0.21 effective wavelengths [6]. Figure 1.4 (c) illustrates the experimental setup for a near-field imaging system with an ultra-thin SiO_2-SiC-SiO_2 superlens, in which 1200nm and 860nm holes can be resolved at a mid-infrared wavelength of 11 μm [7]. At optical wavelengths, the inherent resonances of a metal

can lead to negative permittivity. Thus, a very thin layer of metal can act as a superlens at some specific wavelengths. A representative example of a superlens at optical frequency is shown in Fig. 1.4 (h-k), where a 40nm-thick Ag film substantially improves the image resolution to one-sixth of the illumination wavelength [5].

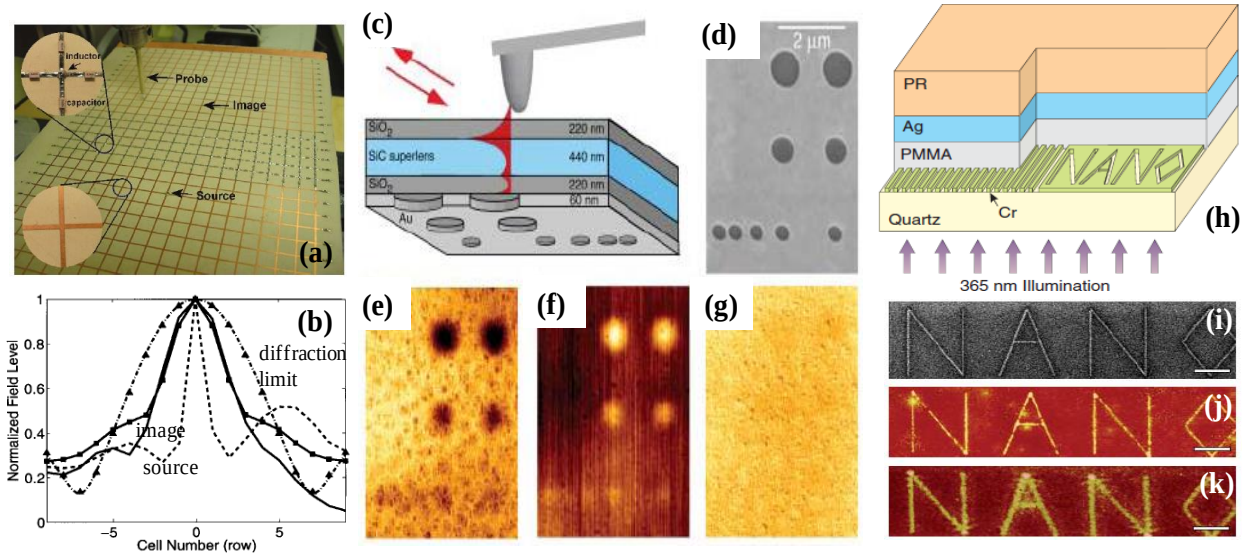

Figure 1.4 Superlens at microwave frequencies with a loaded transmission-line structure [6] (a-b). (a) The planar transmission-line lens. (b) The measured electric field at source (dashed curve), image (solid curve), and diffraction limit (dash-dotted curve with triangles). Superlens at mid-infrared frequencies with an 880nm-thick SiO_2-SiC-SiO_2 structure [7] (c-g). (c) Experimental setup. (d) Scanning electron micrograph of the object plane, showing the holes in the Au film. (e) Infrared amplitude in the image plane at λ=10.85μm. (f) Infrared phase contrast at λ=11.03μm. (g) Control image of amplitude at λ=9.25μm. Superlens at optical frequencies with a thin Ag film [5] (h-k). (h) Experimental setup. (i) Focused ion beam (FIB) image of the object. (j) Atomic force microscopy (AFM) image of the developed image on photoresist with a silver superlens. (k) Control image on the photoresist when the silver was replaced by PMMA.

Three dimensional (3D) optical metamaterials and negative refraction were demonstrated more recently [13,20], but the fabrication process was complicated. Thus, 3D metamaterials at longer wavelength become a very attractive means for fundamental research. It might be easier to construct resonant elements at microwave frequency since constructing resonant elements that are far smaller than the operating wavelength is relatively straightforward, but there are only few experimental demonstrations of 3D metamaterials at these wavelengths yet, due to the challenges

faced by the fabrication of 3D periodic structures. Actually, metamaterials were initially proposed as a 3D structure by Pendry *et al* in 1996 [11], as the wired structure on top left of region II shown in Fig. 1.2. The structure dilutes the average concentration of electrons and considerably enhances the effective electron mass through selfinductance. Therefore, such a structure can depress the plasma frequency into the far infrared or even into the GHz band. One advantage of the structure is that different plasma frequencies can be achieved by varying the lattice constant. Non-uniform periods will introduce anisotropic property to the metamaterial and hence it will be a potential candidate for the application of invisible cloaks [1-3].

1.2.3 Indefinite metamaterial

In addition to the negative index metamaterials, negative refraction and subwavelength imaging can also occur in a simple but important metamaterial, which is constructed by a multilayer metal-insulator stack and widely used for superlens design [28-31], optical lithography [32], and subwavelength sensing/detecting [33].

Considering a particular anisotropic material, where the permittivity component along the propagation direction (*z*-axis) is negative, i.e., $\varepsilon_z < 0$, and all other permittivity and permeability components are positive (assuming a non-magnetic material, i.e., μ=1), the dispersion diagram is in a hyperbolic form

$$\frac{k_z^2}{\varepsilon_x} - \frac{k_x^2}{-\varepsilon_z} = k_0^2, \tag{1.1}$$

where the *z* axis is the light propagation direction. This kind of artificial material is named as "indefinite metamaterial" since not all the components of permittivity and permeability has the same sign [1].

The refraction behavior of an indefinite metamaterial can be determined by the rules as below [26,34]: (1) The group velocity, $v_g \equiv \nabla_k \omega(k)$, specifies the direction of energy flow, which must be normal to the equifrequency surface and in the direction where ω is increasing; (2) The component of the group velocity which is along *z*-axis, v_{gz}, must have the same sign in both media (the air and the metamaterial), since the energy must be carried away inside the metamaterial; (3) The wave vector k_x, which is along the transverse *x*-axis, is continuous across the interface of the air and the metamaterial.

Re-writing Eq. (1.1), the wave vector along the propagation direction k_z can be expressed as

$$k_z = \sqrt{\varepsilon_x \left(k_0^2 - \frac{k_x^2}{\varepsilon_z} \right)} \tag{1.2}$$

Given $\varepsilon_z < 0$ and $\varepsilon_x > 0$ there is no cutoff for any spatial frequency k_x in the metamaterial. In other words, the indefinite metamaterial can convert the evanescent waves which would normally decay in conventional materials into propagating waves, which enables the metamaterial functions as a superlens to form subwavelength images [35-37].

The effective medium theory (EMT) [38] can be applied to approximate the macroscopic behavior of the indefinite metamaterial if only thin alternating layers are included [35]. An alternating Ag-SiO_2 stack is shown in Fig. 1.5(a). The effective permittivity tensor of an indefinite metamaterial can be determined by

$$\begin{cases} \varepsilon_x = \varepsilon_y = \frac{\varepsilon_i + \eta \varepsilon_m}{1+\eta} \\ \varepsilon_z^{-1} = \frac{\varepsilon_i^{-1} + \eta \varepsilon_m^{-1}}{1+\eta} \end{cases}, \tag{1.3}$$

∀

where ε_i and ε_m are the permittivity of the dielectric and the metal, respectively, $\eta = d_m/d_i$ is the ratio of the two layers width. For the layered material, the desired effective permittivity ε_z and ε_x can be tuned either by varying the thickness ratio η or by changing the incident wavelength λ. The permittivity of a metamaterial constructed by the Ag-SiO_2 alternating layers as functions of η (at a fixed λ=630nm) and λ (at a fixed η=1.5), respectively, are demonstrated in Fig. 1.5(b) and (c). The permittivity data of Ag and SiO_2 are taken from the book of Palik [39]. The yellow shadowed regions highlighted in both figures represent that the real parts of ε_z and ε_x having opposite signs, which imply that the possibility to construct the indefinite metamaterial is available over a broad spectral region. The imaginary parts of ε_z and ε_x also need to be taken into consideration, in order to get a low-loss metamaterial.

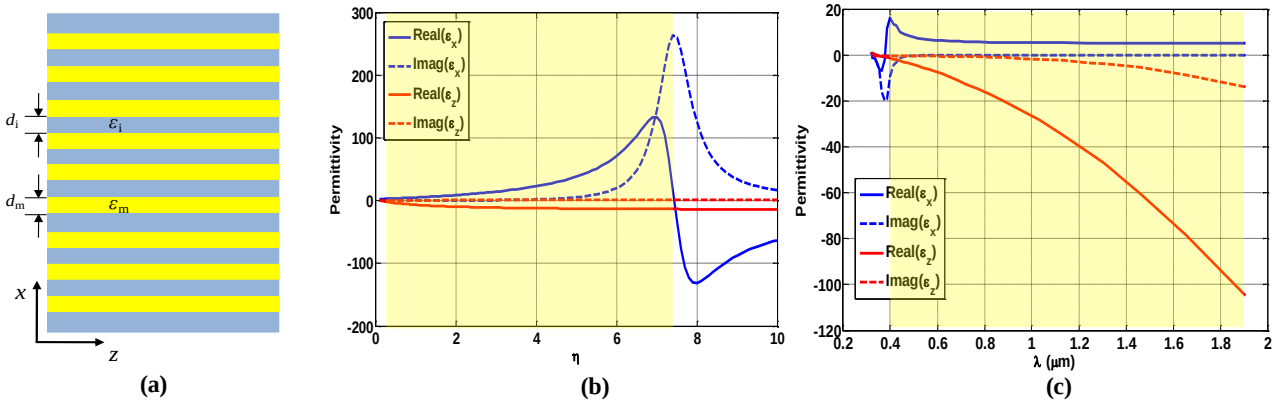

Figure 1.5 (a) A sample of indefinite metamaterial with the coordinates, in which ε_i(ε_m) and d_i(d_m) are the permittivity and the thickness of dielectric material(metal), respectively. (b) The permittivity of a metamaterial constructed by Ag and SiO_2, at λ=630nm, with a varying thickness ratio η. (c) The permittivity of the metamaterial with a fixed thickness ratio η=1.5, at varying thickness. The real of ε_z and ε_x have opposite signs in the yellow shadowed areas in both figures.

Figure 1.6 shows the transmitted electric field intensity $|E_x|^2$, plotted as a function of x, for various different layer widths [35]. Decreasing the width of the layers that make up the metamaterial stack, while keeping the total stack width as a constant, causes the principle peak to

narrow. As the layers get thinner, the transmitted image more closely resembles the effective medium result.

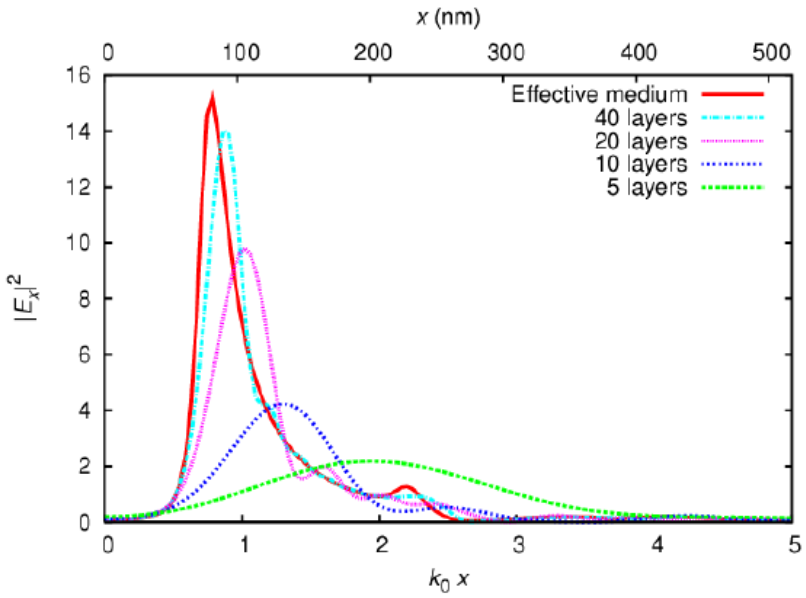

Figure 1.6 The transmitted electric field intensity for a line source, imaged by a metamaterial slab of thickness $1/k_0$. The material parameters used correspond to layers of Ag and ZnS-SiO_2, embedded in crystalline $Ge_2Sb_2Te_5$ (a phase-change material used in optical storage devices), for light of wavelength 650nm. The corresponding total slab width is around 105nm. [35]

1.2.4 Designer surface plasmonic metamaterials

Light hitting a metamaterial is transformed into electromagnetic waves of a different variety [40], namely surface plasmon polaritons (SPPs) [41,42]. The fundamental plasma frequency can be expressed as

$$\omega_p = \sqrt{\frac{N e^2}{\varepsilon_0 m^*}} \tag{1.4}$$

which is proportional to the density of free carriers N, and effective electron mass m^*. For metals, the plasma frequency falls in the ultraviolet part of the light spectrum, due to the high carrier density. The transverse mode size supported by a plasmonic waveguide is mainly determined by the skin depth in the dielectric [43], which can be calculated as

$$\delta_d = \frac{\lambda_0}{2\pi} \sqrt{\frac{-(\varepsilon_m + \varepsilon_d)}{\varepsilon_d}} \tag{1.5}$$

where λ_0 is the wavelength in vacuum, ε_d and ε_m are relative permittivity of the dielectric and the metal (metal is treated as a dielectrics with complex-value permittivity), respectively. Near the plasma frequency (in the ultraviolet regime for most metals), ε_m is comparable to ε_d, resulting in a small transverse mode size. Recent breakthroughs have produced a wide range of nanoplasmonic devices that generate, guide and detect light [44-51]. As the frequency decreases from the near infrared and even down to microwave regime, most metals may be treated as perfect electric conductors (PECs), and the penetration of the EM fields in the dielectric material extends to the distance of the order of many wavelengths and almost completely excluded from the metal surface. The EM waves are weakly localized at the metal-dielectric interface, and the SPPs eventually acquire the characters of Sommerfeld or Zenneck waves [43], which are essentially grazing-incidence light fields.

This problem can be solved by patterning a metal surface texture (e.g. periodic grooves or holes) with subwavelength features, as shown in Fig. 1.7(a) and (b). This approach can be date back to Goubau [43], Mills and Maradudin [52], who discovered that designed surface textures can result in highly bounded surface waves. In those cases, the EM boundary conditions are altered and strongly localized field radiation can be obtained at longer wavelengths. The dispersion relation of the localized modes obtained by the one-dimensional array of grooves is shown in Fig. 1.7(c), which is similar as the one associated with the SPPs supported by the surfaces of real metals. Therefore, this highly localized EM wave on a textured metal slab is called ‘spoof’ or ‘designer’ surface plasmons [53-55].

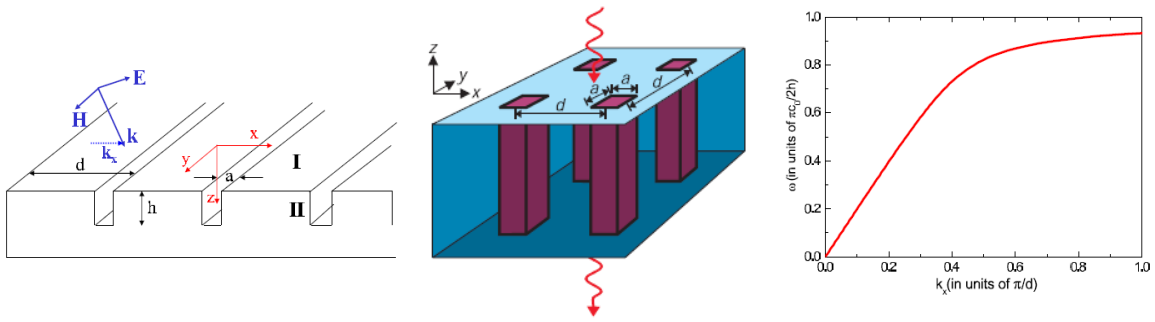

(a) **(b)** **(c)**

Figure 1.7 (a) A one-dimensional array of grooves of width *a*, depth *h*, and periodicity *d*. [53] (b) An $a \times a$ square holes arranged on a $d \times d$ lattice are cut into the surface of a perfect conductor, in which localized surface plasmon modes can be induced by the structure. [54] (c) The dispersion relation [$\omega(k_x)$] of the surface bound states supported by the one-dimensional array of grooves [Fig. 1.7(a)], with geometrical parameters a/d=0.2 and h/d=1. [53]

The existence of designer surface plasmons has recently been verified both in the microwave and THz regimes [56-62]. Figures 1.8(a-b) show at THz frequencies, deep subwavelength energy concentration can be obtained in cylindrical structure and superfocusing in conical structure [60]. The strong localized confinement is achieved by either gradually increasing the depth of the grooves or reducing the radius of the cylindrical cone while keeping a constant groove depth. More recently, simple metal gratings as designer surface plasmon waveguides have been investigated [63]. The basic structure is just a periodic arrangement of grooves patterned on the top surface of metallic slabs. The properties of the guided modes are mainly controlled by the geometrical parameters defining the grooves, as shown in Fig. 1.8(c), the blue curve and the overlapped black curves present the dispersion of the waveguides with different groove heights. One extraordinary property of the waveguide is the modal effective index is almost insensitive to the change of the lateral widths. This enable the structure can be used as a tapered waveguide to obtain subwavelength light concentration at the far-end taper tip, as illustrated in Fig. 1.8(d).

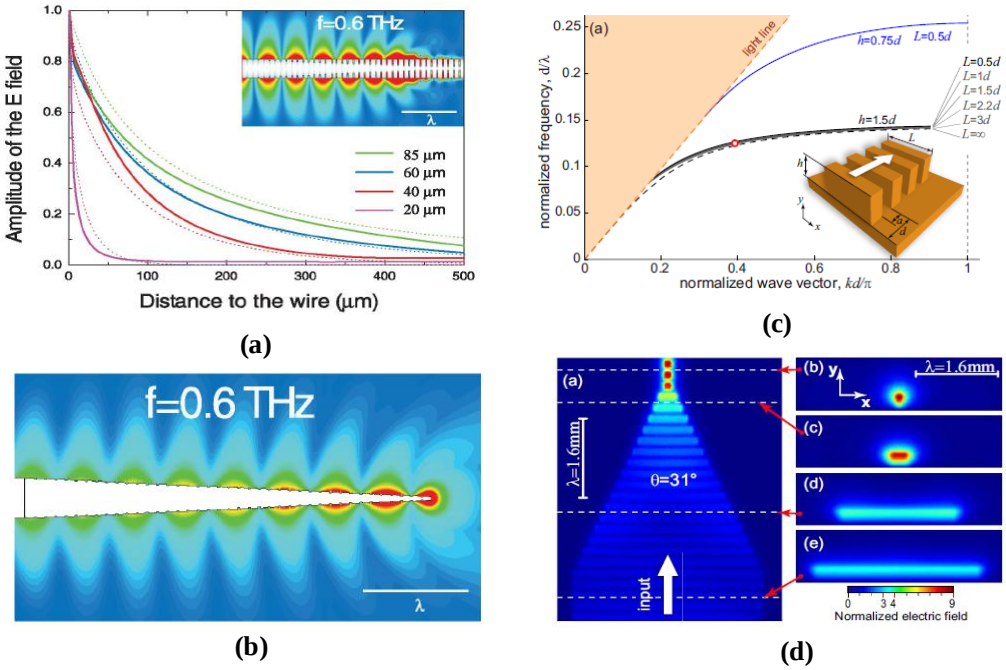

Figure 1.8 (a) Field concentration via adiabatically increased groove depth. Distribution of the E field, evaluated at *f*=0.6 THz, along the radial direction at different locations of the wire corresponding to different depth. The inset shows the distribution of the *E* field on a logarithmic scale. [59] (b) Superfocusing on a corrugated cone of length 2mm (shown in the magnitude of E field on a logarithmic scale), with constant groove depth 5 μm and groove period 50 μm. The radius of the cone is reduced from 100 to 10 μm. [59] (c) Dispersion relation of designer surface plasmon waveguides for various lateral widths *L*. Inset: diagram of the structure and geometric parameters. [63] (d) Left: Poynting vector field distribution in a horizontal plane of the tapered waveguide. Right: Amplitude of electric field in transverse vertical planes at locations shown by white dashed lines in left. [63]

Another advantage of the designer surface plamsonic devices is that since metals are treated as PECs at low frequency regime, there is no difficulty to scale the structure to work at other frequencies based on the ratio of wavelengths. The ability to engineer a surface plasmon at almost any frequency, where metals are nearly PECs from DC up to the threshold of the terahertz regime, provides opportunities to control and direct radiation at surface over a wide spectral range.

1.2.5 Graphene

Graphene as the first 2D atomic crystal available to us [64] and has a nick name ‘miracle material’ due to its many supreme properties, such as mechanical stiffness, strength, elasticity,

very high electrical and thermal conductivity. These properties suggest that graphene could replace other materials in existing applications. The combination of impermeability, transparency and conductivity will find use in transparent protective coatings and barrier films, while transparency, elasticity and conductivity will find application in flexible electronics, and this list of the combinations is continuously growing [64]. One reason that the research on graphene has progressed so fast is the much easier access to high-quality graphene synthesized by laboratory procedures. Various methods have been used for graphene synthesis, for example, liquid phase [65,66] and thermal exfoliation [67], and chemical vapor deposition (CVD) [68,69].

Graphene has been proposed as a new platform for plasmon waveguiding at infrared frequencies [70-74] and can be considered as terahertz (THz) metamaterial [75]. Photons in NIR or THz domain can be readily coupled to surface plasmon polariton (SPP) surface wave with many attractive properties, such as tunability by chemical doping or electrical gating, which is the most important advantage of graphene over metal thin films. The tunability of SPP waves in graphene originates from its complex dynamic conductivity determined from the Kubo formula [73,76,77], which largely depends on the radian frequency ω, scattering rate Γ, and chemical potential μ_c. The imaginary part of the dynamic conductivity, which may have a negative or positive sign at different frequency ranges depends on the chemical potential, plays a key role in supporting different types of surface waves. The dynamical tuning by gate voltage – E_{bias} is in real time, locally and inhomogeneously. By using different values of E_{bias} at different locations across the single graphene layer, desired conductivity patterns can be created [77], as shown in Fig. 1.9. In the simulation result shown in Fig. 1.9(a), the conductivity of the graphene are segmented by two different voltage bias. The imaginary of conductivity of the "farther" half is positive, which supports a TM SPP, while the "closer" half with a negative imaginary part doesn't support TM

SPP. As a TM SPP is launched from the farther half, it reflects back at the boundary, which forms the pattern observed in Fig. 1.9(a). Graphene-based waveguide and splitter can be proposed based on the similar idea, as shown in Fig. 1.9(b) and (c), respectively. In both simulations, an uneven ground plane is used to achieve two different chemical potentials that segment the conductivity of graphene.

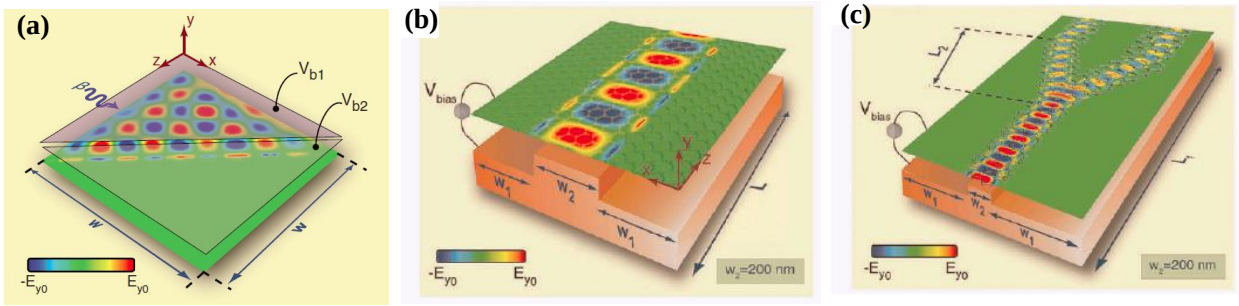

Figure 1.9 Simulation results showing: (a) TM SPP wave pattern on graphene with two different voltage bias; (b) graphene waveguide; and (c) graphene beam splitter. The launched TM SPP is with a frequency *f*=30THz. [77]

Reference [78] shows an example of graphene-based long-wave infrared modulator at *f*=30THz, as illustrated in Fig. 1.10(a). The switching between the ON (high transmitted power, as shown in Fig. 1.10(b)) state and the OFF (low transmitted power, as shown in Fig. 1.10(c)) state is controlled by changing the carrier density in the graphene monolayer via adjusting the bias voltage on a gate contact affixed to the graphene. The interband absorption of the plasmon energy is blocked at high carrier densities resulting in low-loss propagation of the plasmon and a high optical throughput. At low carrier densities, interband absorption is allowed resulting in high-loss propagation of the plasmon and low optical throughput [78].

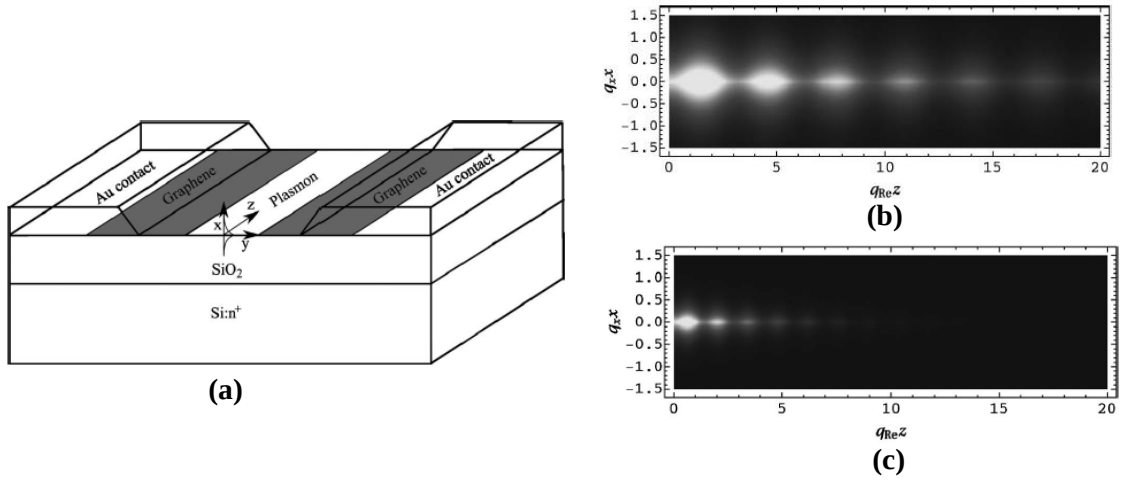

Figure 1.10 (a) Illustration of the plasmon modulator. A gate bias is applied to the graphene monolayer by applying a voltage from the Au contacts to the doped Si substrate. (b) Low-loss state. (c) High-loss state. [78]

By integrating graphene with silicon optical waveguide, graphene could be used as the active medium in an optical electro-absorption modulator [79], as shown in Fig. 1.11(a). The optical modulation phenomenon can be observed in optical bandwidth from 1.35 to 1.60μm. The coupling strength between the evanescent waves and graphene can be controlled by adjusting the Fermi level by using an externally applied gate voltage, which induces the changes in the transmission of the graphene-based optical modulator, as shown in Fig. 1.11(b). Changing the gate voltage bias, the Fermi level will be shifted above or below the threshold value ($\hbar\omega/2$), therefore the optical modulator can be switched "on" or "off" status. In other work [80], where an optical modulator is constructed with two graphene layers separated by an oxide layer, the modulation depth can be further increased to ~0.16dB/μm. These results are comparable to the modulation efficiency observed in traditional optical modulators made of Si [81], GeSi [82], and InGaAs.

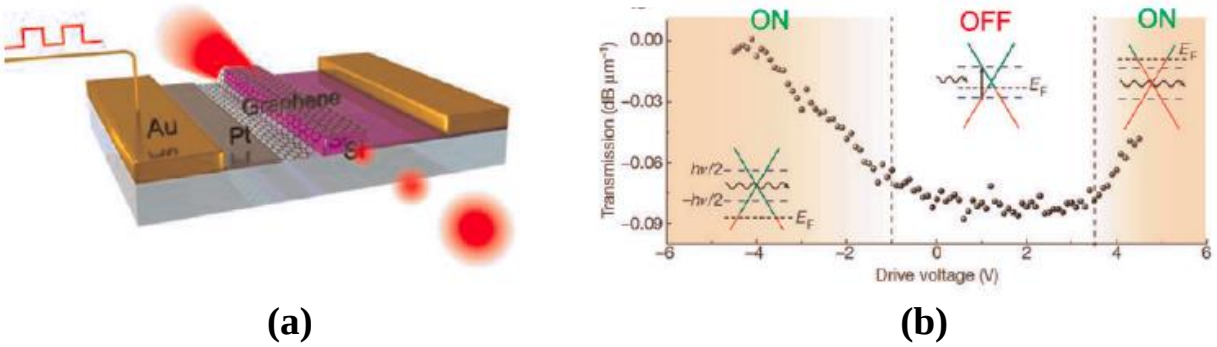

(a) **(b)**

Figure 1.11 (a) Graphene-based electro-optical modulator, where a monolayer graphene is put on top of a silicon waveguide. (b) Static electro-optical response of the modulator at different drive voltages. [79]

1.2.6 Transparent conductive oxides (TCOs)

Transparent conductive oxides (TCOs) are doped metal oxides used in optoelectronic devices such as flat panel displays and photovoltaic [83]. Indium tin oxide (ITO), is a representative of TCOs, which is a solid solution of typically 90% indium oxide (In_2O_3) and 10% tin oxide (SnO_2) by weight. ITO is widely used in industry due to its low resistivity of ~10^{-4} Ω cm and a transmittance greater than 80% [83]. Another representative of TCOs is aluminum-doped zinc oxide (AZO), which is also a degenerately doped semiconductor.

In recent years, TCOs as alternative and promising plasmonic metamaterials for NIR applications have been explored [23,25]. Generally, the characteristic penetration depths to either metal (m) or dielectric (d) $l_{d,m} = \frac{1}{Im(k_{d,m}^z)} = Im\left(\frac{\lambda}{2\pi}\sqrt{\frac{\varepsilon_d+\varepsilon_m}{\varepsilon_{d,m}^2}}\right)$ determines the compactness of the SPP, where z is the direction perpendicular to the interface, $k_{d,m}^z$ is the wavevector in a medium (d or m) in z direction, and λ is the vacuum wavelength. Comparing with Ag and Au, TCOs showed more compact SPPs mode at NIR, as illustrated in Fig. 1.12(a). For a single-sided metal-dielectric (air) structure, the penetration depths in the air are much shorter when the adjacent materials are TCOs at NIR regime. The penetration depth l_d exceeds $\lambda/2$ at 539nm in silver and 660nm in gold,

where the modes are not well confined any more [23]. Note that at proper doping and processing conditions, low loss TCOs have cross-over wavelengths (at which the real part of the dielectric constant is zero) at the telecommunication range, shown in Fig. 1.12(b-c). ITO is demonstrated as a promising material to reduce the footprint of electro-optical (EO) modulator with a cross-over wavelength near the telecom wavelength, as present in Chapter 5.

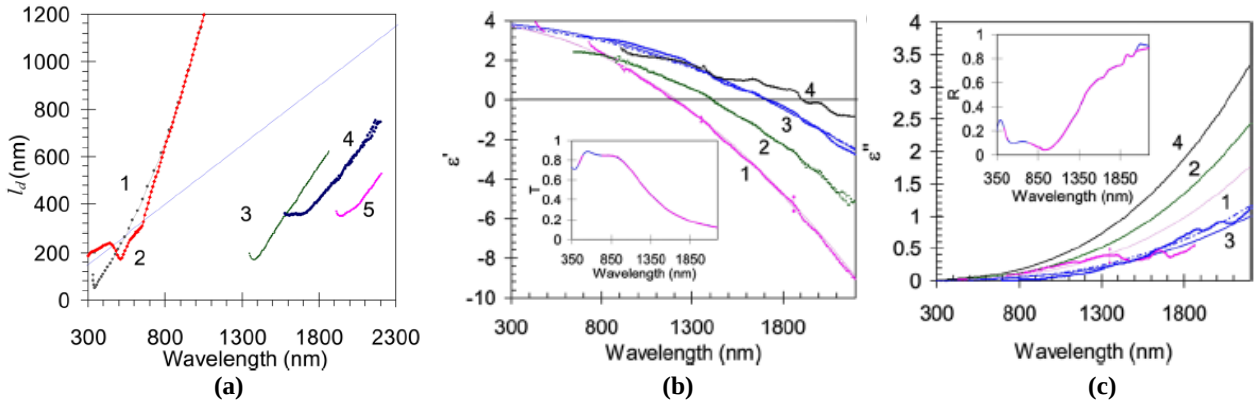

Figure 1.12 (a) SPP penetration depth l_d to an adjacent dielectric medium (air) for silver (1), gold (2), ITO (3), ZITO [$\{ZnO\}_{0.05}$:$\{SnO2\}_{0.05}$:$\{In_2O_3\}_{0.9}$, by weight] (4), and AZO (5). Grey solid line is for $l_d = \lambda/2$. Experimental spectral of real (b) and imaginary (c) part of permittivity for ITO (1), ZITO (2), AZO (3), and ITZO (4). [23]

Another advantage of TCOs is the tunable optical properties, since a small change in carrier density in the accumulation layer may result in a significant change in the dielectric constant with a suitable applied voltage. In Ref. [24], a unity-order index change in ITO at visible frequencies has been experimentally demonstrated in a metal-oxide-semiconductor (MOS) structure, as shown in Fig. 1.13(a). In the MOS-like structure, the semiconductor is replaced by an active material with a higher carrier density. Under an applied field, the structure in Fig. 1.13(a) forms an accumulation layer at the dielectric/conductive oxide interface. The resulting excess carrier density and the local change of the refractive index are shown in Fig. 1.13(b) and (c), respectively. The thickness of the experimentally measured accumulation layer was found to be 5 ±1nm [24] for all applied voltages. For an applied voltage of 2.5 V, at λ_0 = 500nm the index change is Δn_{index} = 0.41 and at λ_0 = 800nm

the index change is Δn_{index} = 1.39. This change in index is accompanied by an increase in the carrier concentration from 10^{21} to 10^{22} cm^{-3} in the accumulation layer. Moreover, the same degree of refractive index modulation was observed even the thickness of the ITO layer was decreased by half, which means for such a thick ITO film, its thickness change would not affect the accumulation layer. Without the SiO_2 layer, no refractive index modulation phenomenon was observed in the experiments. The same modulation effect could be observed in the heterostructure with indium zinc oxide (IZO) replacing the ITO, which indicates that the origin of the refractive index change is related to the formation of an accumulation layer at the SiO_2/TCO interface [24]. This work gave us a hint for designing an ITO-based multilayer modulator, where we also employed an electrolyte gel to replace SiO_2, to provide strong electric field.

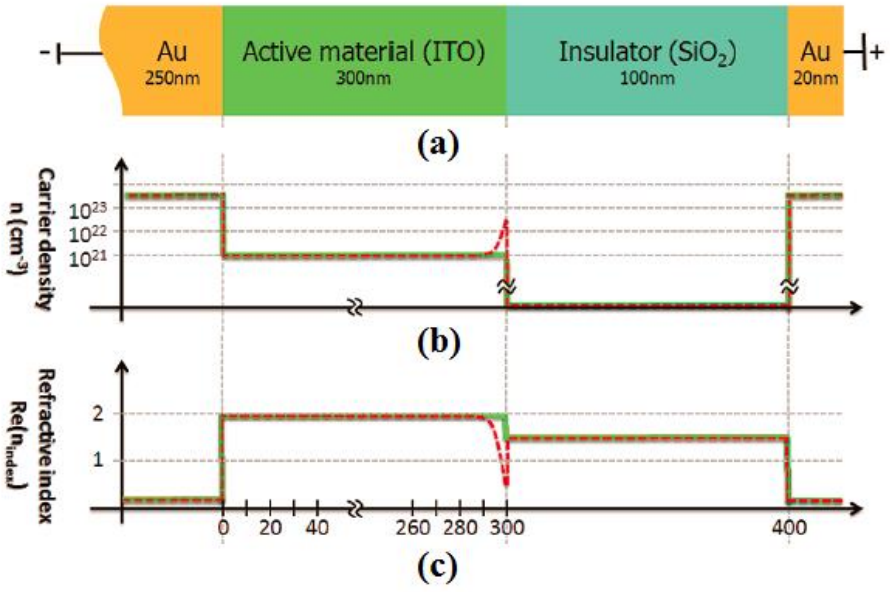

Figure 1.13 (a) Structure schematics. When a voltage is applied to the MOS device, an accumulation layer forms. (b) The carrier density are modified by an applied voltage across the insulator/active material interface. (c) Refractive index modulation. Dashed red/solid green: with/without charge accumulation. [24]

1.3 Fabrication of Metamaterial Samples

Since metamaterials gain the novel properties based on their artificial structures, the fabrication schemes are determined by the functionalities as well as the working frequencies of interest of the metamaterials. Hence, metamaterials could be fabricated in a cleanroom by a series of nano fabrication processes [84], or in a machine shop patterning periodic features [85], or even with electronic textile technology to build 3D cubic structure [86]. In this section, a general introduction of fabrication methods of man-made metamaterials will be presented, as well as those of the naturally existing metamaterials – graphene and ITO.

1.3.1 Metamaterial with artificially designed structures

At the early stage, metamaterials were experimentally demonstrated at microwave frequency regime, because it is relatively easy and straightforward to construct resonant elements at longer wavelengths. Metamaterials have been successfully shown their applications in invisible cloak as shown in Fig. 1.14(a) [87], flat lens [86] and subwavelength waveguiding and focusing [85] at microwave frequency. Usually, these metamaterials are fabricated in a layer-by-layer fashion, then assemble all the layers together to form the metamaterial sample. Designer surface plasmonic (DSP) metamaterials are fabricated by patterning periodic features, for example, holes or grooves, on the surface of metal slabs.

The fast development of nano fabrication techniques as well as the advancement of material research enable the dimension of the unit cells down to terahertz, near-infrared and optical frequency regimes. Figures 1.14(b)-(d) show the SEM images of metamaterials [84] fabricated by a series of nano/micro fabrication processes, including thin film deposition, patterning and etching. It is easily seen that for optical metamaterials [84], the fabrication processes are complicated and time-consuming.

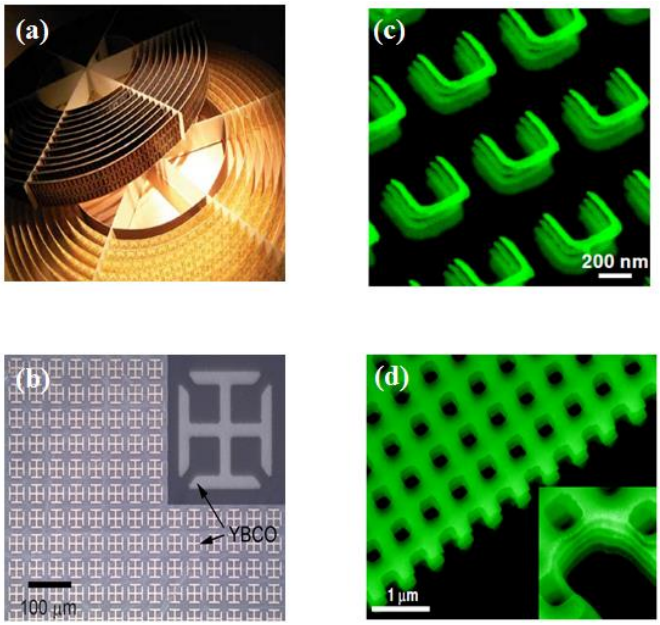

Figure 1.14 (a) Microwave invisible cloaks [87]. (b) Terahertz metamaterial [88]. (c) and (d) Optical metamaterials. [84]

1.3.2 Graphene synthesis, transfer and characterization

In order to practically implement graphene to devices, reliable, stable and economical process techniques should be developed. One of the most successful methods that results in isolation of single layer graphene (SLG) is the mechanical exfoliation [89]. Beside the mechanical exfoliation, other promising techniques as epitaxial growth on metal substrates [68,90-92,94], epitaxial growth on silicon carbide [94,95], growth from metal-carbon melts [69], and chemical synthesis [96,97]. Figure 1.15 illustrates some of these methods, their cost and the quality of graphene film synthesized by each corresponding method.

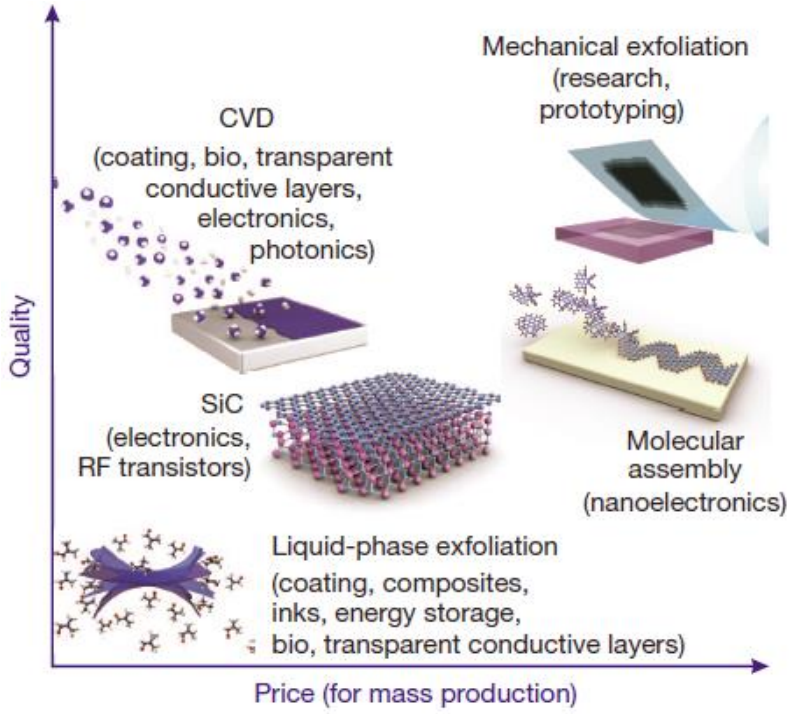

Figure 1.15 Several methods of mass-production of graphene, which allow a wide choice in terms of size, quality and price for any specific application. [64]

Epitaxial growth of graphene on metal substrates uses the atomic structure of metal substrates to seed the growth of the graphene [68,90-92,94]. Ni and Cu thin films deposited on top f SiO_2/Si wafers are usually used as the substrate. After the graphene growth, instantaneous etching of metal films and polymer-supported transfer onto other substrates are followed. These methods are using mixed gas of Methane, Hydrogen, Argon or Helium in a high temperature furnace for the growth of graphene. It is shown that mono- and bi-layer graphene grows predominantly on a Cu substrate, while on Ni, the layers of graphene range from three to eight, which depends on the reaction time and cooling rate [90]. Cooling rate significantly affects the amount and quality of the carbon segregated on the metal substrates. With a 10 ℃/s cooling rate, high quality graphene with well-controlled thickness can form on a Ni substrate.

Large and homogeneous layers of graphene can also be obtained by annealing silicon carbide in a dense noble gas atmosphere, so silicon will sublimate from SiC surface. During the

process, graphene nucleates along the $\left(110n\right)$ plane, which is known as terrace step edges, on the silicon carbide surface. The nucleation and growth of monolayer graphene on the Si-face of SiC is highly dependent on growth conditions, SiC surface morphology, and SiC surface defects. The quality of the graphene films can be improved with a higher synthesis temperature (1425 ℃) [95].

Graphene may also grow from metal-carbon melts [69]. This process involves dissolving carbon inside a molten metal at a specified temperature and then allowing the dissolved carbon to nucleate and grow on top of the melt at a lower temperature. Similarly as the epitaxial growth methods, Ni and Cu could be used as the molten metal. First, the metal is melt and in contact with a carbon source. The source could be graphite chunk or powder temperature results in dissolution and saturation of carbon atoms in the melt. Upon lowering the temperature, the solubility of carbon in the molten metal decreases and the excess amount of carbon precipitates on top of the metal. High-quality single layer graphene is obtained in the Ni melt [69].

Graphene can be produced by direct chemical synthesis. Common laboratory reagents ethanol and sodium are used and single layer graphene is synthesized by low-temperature flash pyrolysis of solvothermal product of the two reagents, followed by gentle sonication of the nanoporous carbon product [96]. Graphene nanoribbons (GNR) with width below 10nm are solution-phase-derived, stably suspended in solvents with noncovalent polymer fictionalization, and exhibited ultra-smooth edges with possibly well-defined zigzag or armchair-edge structure [97].

Graphene-transferring process is a key as well as challenging step in the fabrication of devices [98-100], since the thin graphene film is very delicate and easily broken during the process. The process shown in Fig. 1.16 is the as-grown graphene transferring to a desired substrate in a

step-by-step fashion. The graphene sample is synthesized by chemical vapor deposition (CVD) technique [68,69]. Polymethyl-methacrylate (PMMA) as a supporting and protection layer will be coated on top of graphene. Then the PMMA/graphene/nickel/SiO_2/Si chip will be immersed into buffered oxide etch (BOE) solution to etch SiO_2 layer first. After the long etching process in BOE, the film will be transferred to $FeCl_3$ solution to remove nickel residue. The following step after the transfer (shown in Fig. 1.16(b)) is to remove the PMMA by acetone. Then the graphene sheet on the target substrate will be rinsed in IPA and dry. Figure 1.16(c) shows the 'active' graphene after lithography/oxygen plasma etching, in which the graphene region is 11μm long in the light propagation direction.

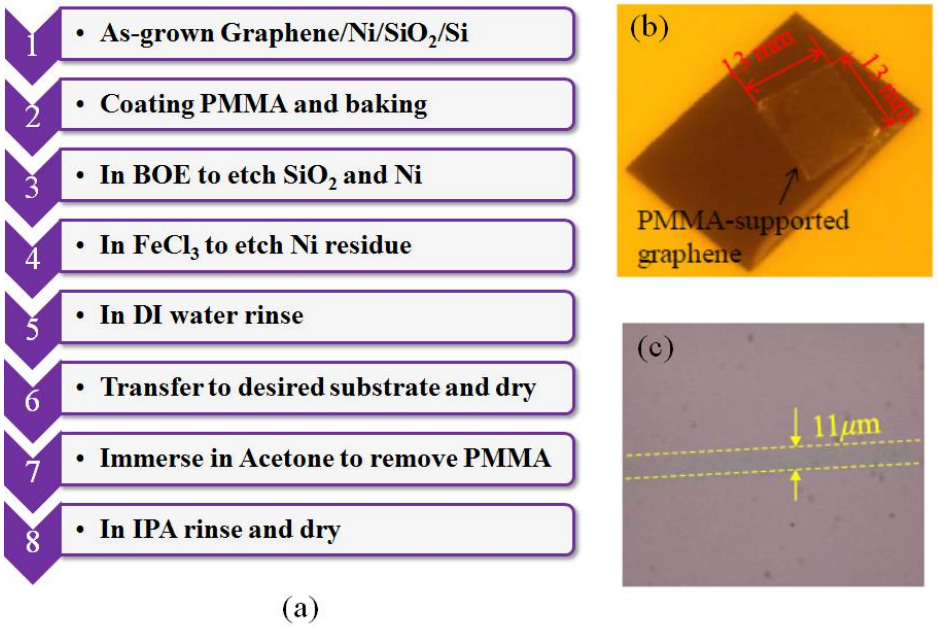

Figure 1.16 (a) Process for transferring as-grown graphene to a desired target. (b) PMMA-supported graphene on the target. (c) After oxygen etching, the graphene region is highlighted by the yellow dashed lines.

Accurately determining the numbers of layer of a graphene sample is critical for its applications. Raman spectroscopy is a noncontact, reflective technique, which provides a fast, nondestructive means of determining layer thickness of graphene thin films. The Raman spectrum

of graphene exhibit a relatively simple structure characterized by three principle bands designated as the G-band at ~1582 cm^{-1}, D-band at ~1350 cm^{-1} and 2D-band at ~2685 cm^{-1}, as an example of the Raman spectrum of highly ordered pyrolytic graphite (HOPG) is shown in Fig. 1.17(a).

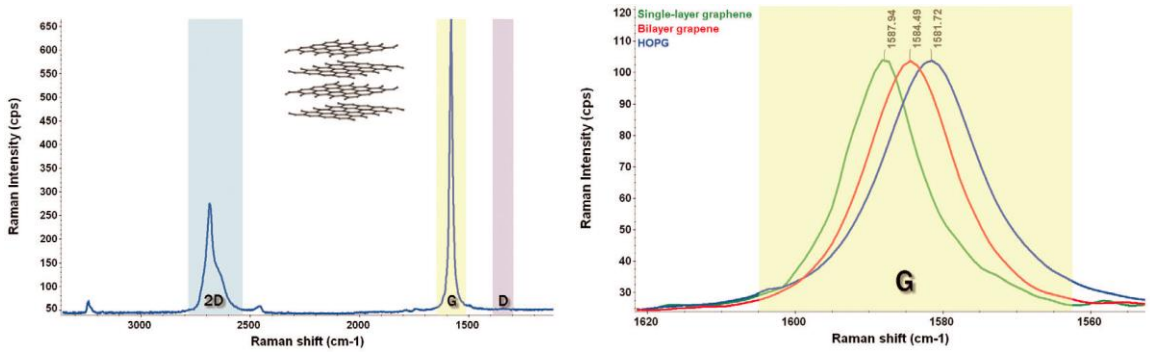

(a) **(b)**

Figure 1.17 (a) Raman spectrum of highly ordered pyrolytic graphite (HOPG). (b) Illustration of as layer increases, the G-band shifts. [101]

The most important information contains in G-band is used to determine the layer numbers in graphene. Figure 1.17(b) demonstrates the effect of layer numbers of graphene on the shifting of G-band. As the layer number increases, the peak of the G-band shifts to lower energy, which represents a slight softening of bonds [101,102]. The D-band is known as the defect band, and its intensity is proportional to the defect level in the graphene sample, which is typically weak in high quality graphene. The 2D-band is the second order of the D-band, but it does not represent of defects in the sample. This band is also used to determine the layer numbers of graphene. Comparing with the G-band method, the 2D-band method depends on both the band position and the band shape, which is clearly demonstrated in Fig. 1.18. For single layer graphene, the shape of the 2D-band is symmetrical. As the layer number increases, the 2D-band could be split into several overlapping modes [102].

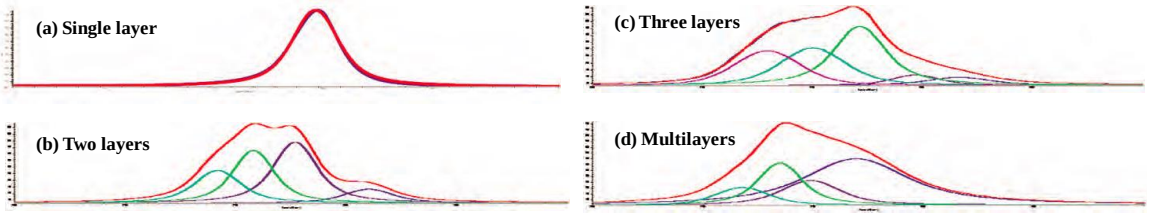

Figure 1.18 The significant different band shapes (red curves) of 2D-band with the number of layers on each. [102]

1.3.3 ITO deposition and annealing

The optical property of ITO mainly depends on its deposition and post-deposition annealing conditions, which includes the ambient gases and the temperature [103]. The deposition method could either be sputtering or laser ablation [104]. In Semiconductor & Microsystems Fabrication Laboratory (SMFL) of RIT, ITO thin film can be deposited by sputtering process with CVC601. The basic idea of sputtering is using accelerated particles to bombard the target and knock the target atoms out. Then these free atoms will be deposited on the surface of the substrate. During the sputtering process, plasma is usually used since it contains charged particles, this low-pressure gas is easily directed by electric fields. To obtain plasma, a voltage will be applied on a pair of electrodes. Free electrons which gain energy from the electric fields will collide with gas particles, eventually cause ionization. This is known as direct-current (DC) glow discharge [105]. The sputtering process using a $(In_2O_3)_{0.9}(SnO_2)_{0.1}$ weight percentage target, was done at room temperature and at 7.3mTorr pressure within the chamber. Argon is the only gas used in the deposition process. With a deposition time of 12 mins, the ITO thin film has a high sheet resistance around 3000 ~ 4000 Ω/□. And the thickness of ITO film is measured and turned out in the range of 22-25nm.

Significant changes in the conductivity of ITO film can be observed with post-deposition annealing process in different ambient, for example, film annealed in nitrogen showed more

conductive and in oxygen less conductive but more transparent [106]. In Ref. [107], the change of the dielectric function of the e-beam evaporated ITO film is observed with different annealing ambient environments, as shown in Fig. 1.19. A higher annealing temperature increases the conductivity of ITO film and reduces the loss within the wavelength range of interest [107]. The post-annealing process is carried out in a vacuum oven – Heraeus oven – at 350˚C for 4 hours. After the annealing process, the sheet resistance of the ITO film decreased significantly, which was in the range of 60-100Ω/□. The optical property of the ITO film will be introduced in Chapter 5.

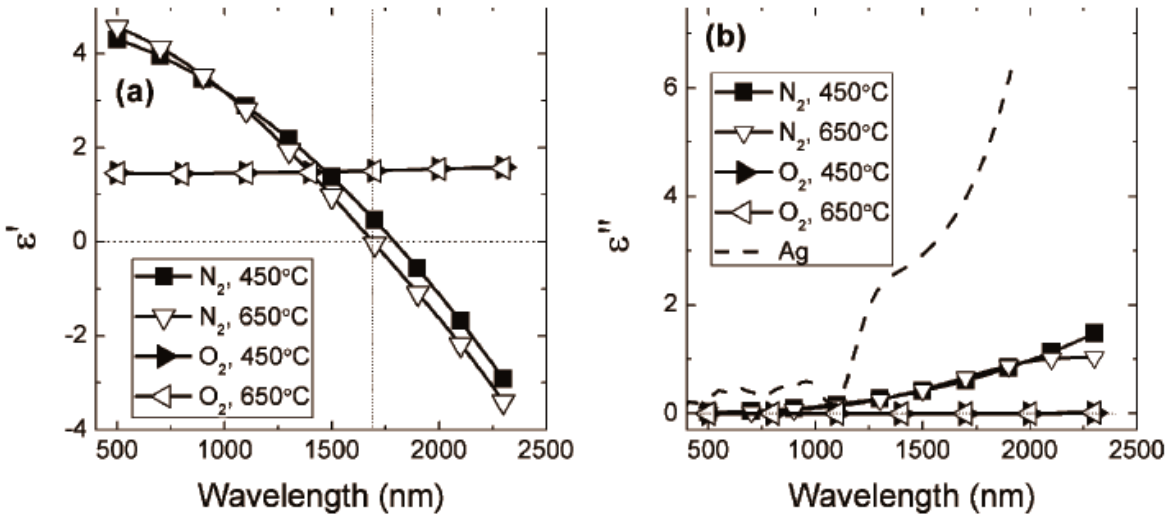

Figure 1.19 Real (a) and imaginary (b) parts of permittivity of ITO annealed at various conditions (N_2, 450˚C; N_2, 650˚C; O_2, 450˚C; O_2, 650˚C). [107]

1.4 Finite-Difference Time-Domain (FDTD) Modeling

The FDTD method [108] is one of the most important and effective numerical methods to study metamaterials, which was proposed by Yee in 1966 [109]. Since FDTD is a time domain solver, it is convenient to investigate the characteristics of metamaterials over a wide frequency regime. The basic idea of Yee algorithm is simultaneously dealing with both electric and magnetic

fields in time and space using coupled form of Maxwell's curl equations. The Maxwell's curl equations in linear, isotropic, nondispersive materials can be written as

$$\frac{\partial \vec{H}}{\partial t} = -\frac{1}{\mu}\nabla \times \vec{E} - \frac{1}{\mu}\sigma^* \vec{H} \tag{1.5}$$

$$\frac{\partial \vec{E}}{\partial t} = \frac{1}{\varepsilon}\nabla \times \vec{H} - \frac{1}{\varepsilon}\sigma \vec{E} \tag{1.6}$$

where σ* is equivalent magnetic loss, σ is the electric conductivity, $\vec{E}$ is the electric field, $\vec{H}$ is the magnetic field, ε is the medium permittivity and μ is the permeability. Expanding the vector components of the curl operators of Eq. (1.5) and (1.6) yields the following six coupled scalar equations under Cartesian coordinate, which are the basis of the FDTD numerical algorithm for modeling electromagnetic wave interactions with arbitrary three-dimensional objects [110]

$$\frac{\partial H_x}{\partial t} = -\frac{1}{\mu}\left[\frac{\partial E_z}{\partial y} - \frac{\partial E_y}{\partial z}\right] - \frac{\sigma^*}{\mu} H_x \tag{1.7}$$

$$\frac{\partial H_y}{\partial t} = -\frac{1}{\mu}\left[\frac{\partial E_x}{\partial z} - \frac{\partial E_z}{\partial x}\right] - \frac{\sigma^*}{\mu} H_y \tag{1.8}$$

$$\frac{\partial H_z}{\partial t} = -\frac{1}{\mu}\left[\frac{\partial E_y}{\partial x} - \frac{\partial E_x}{\partial y}\right] - \frac{\sigma^*}{\mu} H_z \tag{1.9}$$

$$\frac{\partial E_x}{\partial t} = -\frac{1}{\varepsilon}\left[\frac{\partial H_z}{\partial y} - \frac{\partial H_y}{\partial z}\right] - \frac{\sigma}{\varepsilon} E_x \tag{1.10}$$

$$\frac{\partial E_y}{\partial t} = -\frac{1}{\varepsilon}\left[\frac{\partial H_x}{\partial z} - \frac{\partial H_z}{\partial x}\right] - \frac{\sigma}{\varepsilon} E_y \tag{1.11}$$

$$\frac{\partial E_z}{\partial t} = -\frac{1}{\varepsilon}\left[\frac{\partial H_y}{\partial x} - \frac{\partial H_x}{\partial y}\right] - \frac{\sigma}{\varepsilon} E_z \tag{1.12}$$

In Yee's algorithm, $\vec{E}$ and $\vec{H}$ components are positioned at the centers of the grid lines and surfaces such that each $\vec{H}$ component is surrounded by four $\vec{E}$ components, and vice versa, as shown in Fig. 1.20.

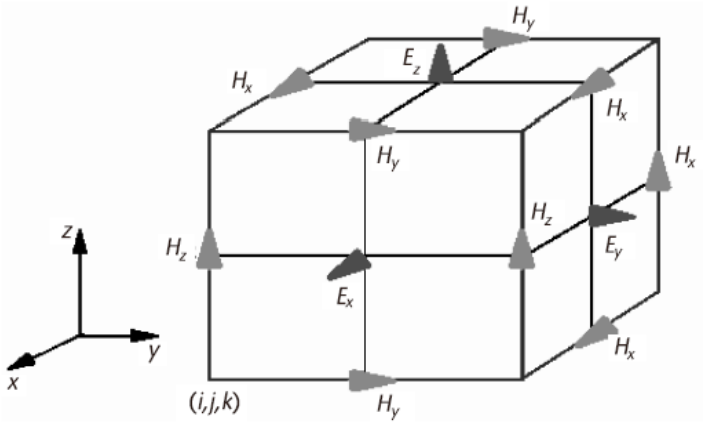

Figure 1.20 Yee's spatial grid. (Internet)

In Yee's algorithm, all of the $\vec{E}$ components in the modeled space are computed and stored in memory by using the previously computed values of $\vec{E}$ and the newly updated $\vec{H}$ field data. In the next step, $\vec{H}$ is recomputed in a similar way. This process stops when the time-stepping is terminated [110].

In order to get numerical stability of the Yee algorithm, an upper bound on the time step Δt should be set, which is determined by the spatial increments Δx, Δy, Δz in accordance with the Courant-Friedrich-Levy (CFL) stability condition [110]. In three dimensions the condition is given by

$$\Delta t \leq \Delta t_{max} = \frac{1}{c\sqrt{\frac{1}{\Delta x^2}+\frac{1}{\Delta y^2}+\frac{1}{\Delta z^2}}} \tag{1.13}$$

1.5 Dissertation Overview

This dissertation presents numerical and experimental results of novel metamaterials and their applications in subwavelength waveguiding, imaging and modulating. These results are structured as follows.

Chapter 2 presents the motivation, numerical modeling and the experimental demonstration of a metal grating functioning as a designer surface plasmonic waveguide, which can support deep subwavelength surface modes and the width of the modes can be squeezed also into deep subwavelength by tapering the width of the waveguide.

Chapter 3 introduces a re-visit of classical optical phenomenon – Talbot effect, in indefinite metamaterial. The 2D and 3D numerical simulations show that the "super" Talbot effect can be achieved in the indefinite metamaterial, even without the paraxial approximation.

Chapter 4 presents the numerical modeling of optical switch based on a metal-insulator-metal plasmonic waveguide with Si_3N_4 core sandwiched between two gallium (Ga) metal layers. Combing the unique structural phase transition property of gallium, within a total length of 400nm, an extinction ratio as high as 7.68 dB can be achieved in the proposed nanoplasmonic structure.

Chapter 5 proposes active plasmonic metamaterials for electro-optical modulator applications. When applying external voltages on these ITO-based multilayer structures, electric double layers are formed at the interfaces of ITO and electrolyte gel. Based on attenuated total reflection (ATR) measurement results, modulation depth up to 38.8% can be achieved. Preliminary result is present for the real time response of an ITO/electrolyte gel/doped-Si modulator.

Chapter 6 continues the work in Chapter 5 and investigates a novel waveguide, namely "TCO-slot waveguide", which combines both the tunable property of a TCO and field enhancement of a slot waveguide. In this work, light absorption can be sharply enhanced when the slot dielectric constant is tuned close to zero. Based on TCO-slot waveguides, efficient electro-absorption modulation can be achieved within 200nm with small insertion loss.

Chapter 7 experimentally demonstrates greatly enhanced light absorption by monolayer graphene over a broad spectral range, from visible to near infrared, based on the attenuated total reflection. In the experiment, graphene is sandwiched between two dielectric media referred as superstrate and substrate. Based on numerical calculation and experimental results, the closer the refractive indices of the superstrate and the substrate, the higher the absorption of graphene will be. The light absorption of monolayer graphene up to 42.7% is experimentally achieved.

Chapter 8 continues the work in Chapter 7 and presents the recent exploration of graphene electro-optic modulators based on graphene sandwiched in dielectric or plasmonic waveguides. With a suitable gate voltage, the dielectric constant of graphene can be tuned to be very small due to the effect of intraband electronic transition, resulting in "graphene-slot waveguides" and greatly enhanced absorption modes. Up to 3 dB modulation depth can be achieved within 800nm long silicon waveguides, or 120nm long plasmonic waveguides based on three-dimensional numerical simulations.

Chapter 9 summarizes work as well as an outlook for future work.

Chapter 10 lists all the publications.

1.6 Contributions

The following are the main contributions of this dissertation.

1) We propose to use microwave near-field imaging system, which is known to be the first time this method is used to study designer surface plasmons. The fundamental work can be extended to design DSP devices at THz frequency regime.

2) We explore the novel effects of light propagation in indefinite metamaterials and propose the applications in various operational settings, i.e. lithography, optical storage, and imaging system.

3) We investigate the epsilon-near-zero (ENZ) properties of natural materials – graphene and ITO, combining novel slot waveguides as the platform to propose ultra-compact, efficient electro-optical modulators.

4) We experimentally demonstrate the absorption of monolayer graphene can be significantly enhanced over a broad spectral range, where there is no complicated, time-consuming fabrication process involved.

2 DEEP SUBWAVELENGTH WAVEGUIDING AND FOCUSING BASED ON DESIGNER SURFACE PLASMONS

In Chapter 2, focusing and guiding electromagnetic (EM) waves in a designer surface plasmonic waveguide with deep subwavelength mode cross section was experimentally demonstrated. The experiments show that a metal grating with suitable parameters, functioning as a designer surface plasmonic waveguide, can support deep subwavelength surface modes and the width of the modes can be squeezed also into deep subwavelength by tapering the width of the waveguide. The results provide a new insight into deep subwavelength waveguiding and focusing [85]. It is the first time that microwave near-field microscopy has been used to study designer surface plasmons experimentally.

2.1 Introduction

Surface plasmons can be viewed as quasi 2D EM excitations, propagating along a dielectric-metal interface and having the field components decaying exponentially with small skin depth into both neighboring media [42,111-112]. The transverse mode size supported by a asmonic waveguide is mainly determined by the skin depth in the dielectrics [42], which can be calculated as $\delta_d = \frac{\lambda}{2\pi}\sqrt{\frac{-(\varepsilon_m+\varepsilon_d)}{\varepsilon_d}}$, where λ is the wavelength in vacuum, ε_d and ε_m are relative permittivity of the dielectrics and the metal (metal is treated as a dielectrics with complex-value permittivity), respectively. Near the plasma frequency (in the ultraviolet regime for most metals), ε_m is comparable to ε_d, resulting in a small transverse mode size. Recent breakthroughs have produced a wide range of nanoplasmonic devices that generate, guide and detect light [42,44-

47,50,51,113,114]. However, far below plasma frequency, ε_m is approximately a pure imaginary number with large magnitude, resulting in a very large transverse mode size (~$10^2\lambda$ and ~$10^3\lambda$ in the THz and microwave regimes, respectively). This limits some important applications of surface plasmons, especially in the THz regime, where deep subwavelength optical devices will be a critical technique for the integration of THz, photonic, and electronic circuits on the same chip using the CMOS compatible technology.

Nevertheless, this issue can be addressed by plasmonic metamaterials, where the dispersion of surface plasmons and spatial confinement of waves can be engineered by designed surface textures. This approach can date back to Goubau [43], and Mills and Maradudin [52], who discovered that a surface texture on metal, such as arrays of holes or grooves, can result in highly bounded surface waves. In 2004 and 2005, researchers established their similarity with surface plasmons and referred them to as "designer surface plasmons" or "spoof surface plasmons" [54-55]. The existence of designer surface plasmons has recently been verified both in the microwave and THz regimes [56,58,115]. More recently, significant progress has been made on designer surface plasmonic (DSP) devices using various types of surface textures [59-63,116]. However, most of effort has been focused on numerical investigations and the importance of designer surface plasmons is far from being demonstrated. Herein, we demonstrate the remarkable advantages of using the designer surface plasmons for deep subwavelength waveguiding and focusing.

2.2 Design and Fabrication

2.2.1 Modeling

The main structures involved in our work are simply metal gratings, specifically aluminum slabs patterned with an array of rectangular grooves. The metal gratings as DSP waveguides were investigated more recently [53,63]. Assume the width, length and depth of each groove are *w*, *a*

and h, and the period of the array is d. Pendry's pioneering work shows that a simple metal grating can work well as a DSP waveguide [54].

If only the fundamental TM-like mode (magnetic field **H** is parallel to the groove orientation) is considered, the dispersion of EM waves propagating in the DSP waveguide can be described as [45]

$$tan(k_0 h) \sum_{n=-\infty}^{\infty} S_n^2 \frac{k_0}{\sqrt{\beta_n^2 - k_0^2}} = 1, \tag{2.1}$$

where $\beta_n = \beta + \frac{2n\pi}{d}$, $S_n = \sqrt{\frac{a}{d}} \sin c(\beta_n a/2)$, β is the propagation constant, and k_0 is the wave number in free space. The dispersion curve is similar to that of widely investigated dielectric-metal plasmonic waveguides in the near infrared or visible regimes. When $k_0 h \approx \pi/2$ or equivalently $\lambda \approx 4h$, β reaches its maximum. Therefore, the surface structure can "shift" the effective plasma frequency of the textured metal into any region closer to working frequency and achieve much stronger mode binding. More precisely, due to the interference of multiple waves on the surface texture, a tightly bounded mode can be formed on the surface. In particular, based on the dispersion relation, such a metal grating can be roughly equivalent as an h-thick layer of homogeneous but anisotropic medium on PEC when $a << d << \lambda$ [53]. Consequently, if only the first order diffraction is considered, the skin depth over the grating can be estimated as

$$\delta_d = \left[k_0 \frac{a}{d} \tan(k_0 h)\right]^{-1}, \tag{2.2}$$

which can be on the deep subwavelength scale. Moreover, due to the tight binding of surface waves, the decrease of the width of the grating will reduce the mode size in another transverse direction, yet not significantly alter the dispersion of the guided modes [63]. An extreme case is that the surface texture is converted into a series of aligned rods, which can guide EM waves at ultra-deep

subwavelength scale in both transverse directions. Essentially, the aligned rods form a 3D deep subwavelength DSP waveguide, similar as arrays of nanoparticles forming nanoplasmonic waveguides in the visible light regime [44,116].

2.2.2 Fabrication and experimental setup

The 2D and 3D DSP waveguides are designed to work at microwave regime by patterning arrays of periodic surface textures on an aluminum slabs. The structure designs are using 3D CAD software SolidWorks and the fabrication is finished by Brinkman Machine Tools and Manufacturing Laboratory at RIT. Figure 2.1 shows some pictures of the designer surface plasmonic waveguides. The main parameters of the 3D waveguide shown in Fig. 2.1(a) are: period d=12.7mm, metal rod length a=6.35mm, width w=6.35mm, height h=19.05mm. A directional coupler is formed by aligning two identical 3D waveguides, as illustrated in Fig. 2.1(b). For the tapered waveguide, input 2D waveguide width W=203mm, tapered region length L=216mm. The parameters of the 3D waveguide are the same as those shown in Fig. 2.1(a).

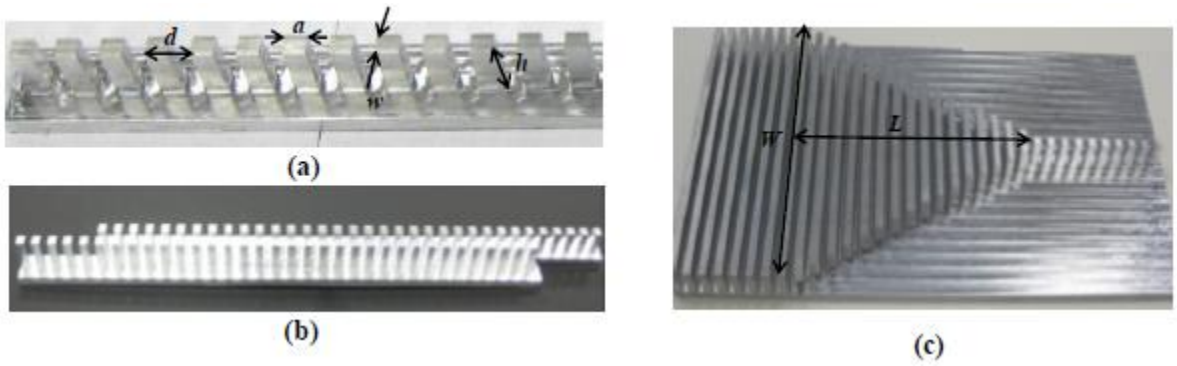

Figure 2.1 (a) 3D DSP waveguide. (b) Two identical 3D waveguides are aligned and forming a directional coupler. (c) Tapered DSP waveguide with a 2D waveguide as input. [85]

To experimentally explore its performance, a microwave near-field measurement setup based on a vector network analyzer was built [9,117,118] as shown in Fig. 2.2, where the propagation of EM waves in a waveguide can be measured by the raster scan of a 1-mm microwave

monopole to detect the evanescent tails. One monopole was fed as the source and another was used as the detector. The movement of the detector in *x* and *y* directions was controlled by a motion controller. In order to show the mode profiles rather than in *x*-*y* plane, a manual stage (along *z*-axis moving range: 25mm, minimum resolution: 0.025mm) was used in the experiments to control the movement of the detector in *z* direction. The precise control of the motion of the detector and the small size of the detector ensured that the experimental results were reliable [119]. To get accurate results, the maximum pixel size was set to be 0.5mm by 0.5mm in the measurements related to the calculations of mode sizes along different directions. Both the amplitude and phase of each measurement point were recorded by the E8362A PNA vector network analyzer.

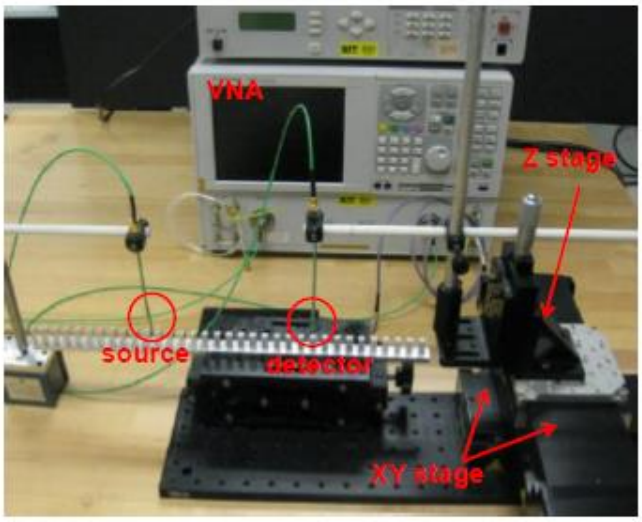

Figure 2.2 Experimental setup based on VNA and XYZ stages.

2.3 Experimental results and analysis

2.3.1 3D DSP waveguide

Figure 2.3 plots the dispersion diagram of the supported modes. When the working frequency varies from 1.4 GHz to 3.3 GHz, the effective index of the corresponding guided modes increases, and then jumps to the second band starting at 8.39 GHz, which is not shown in the figure.

Compared with the dispersion relation of the 2D DSP modes (infinite width), the finite width of the 3D DSP waveguide imposes a lower-side cutoff frequency when the dispersion curve is located inside the light cone. After a raster-scan of the detector at different locations over the structure, good guided modes at frequencies between 1.5 GHz and 3.5 GHz were observed, which respectively coincide with the lower and upper cutoffs of the numerical results as shown in Fig. 2.3. Furthermore, according to the phase distribution along the waveguide, we can calculate the propagation constants at different frequencies. As shown in Fig. 2.3, the measured dispersion curve is in good agreement with the simulated one. Figure 2.4 shows the intensity of the mode profile in different directions at f = 2.25GHz. Figure 2.4(a) is the fabricated 3D DSP waveguide. As shown in Figs. 2.4(b)-2.4(d), the guided mode is tightly "nailed" on the metal rods of the grating and slightly diverges between the rods. The slightly beating of the intensity shown in Fig. 2.4(d) is due to the back reflection. The maximum of the mode size can be mapped in the middle plane of two neighboring rods. The mode size slightly varies with different frequencies and minimizes at 5.5mm-by-4.5mm (or 0.04λ-by-0.03λ) by intensity full width at half maximum (FWHM) at 2.25 GHz, as shown in Fig. 2.4(e). Over the metal rod, the mode size is 7.00mm-by-1.00mm as shown in Fig. 2.4(c). And the mode size measured along the side wall of the rod shown in Fig. 2.4(f) is 15mm-by-1.3mm. Therefore, the overall mode size relies on the dimensions of rods and can go into the deep subwavelength scale.

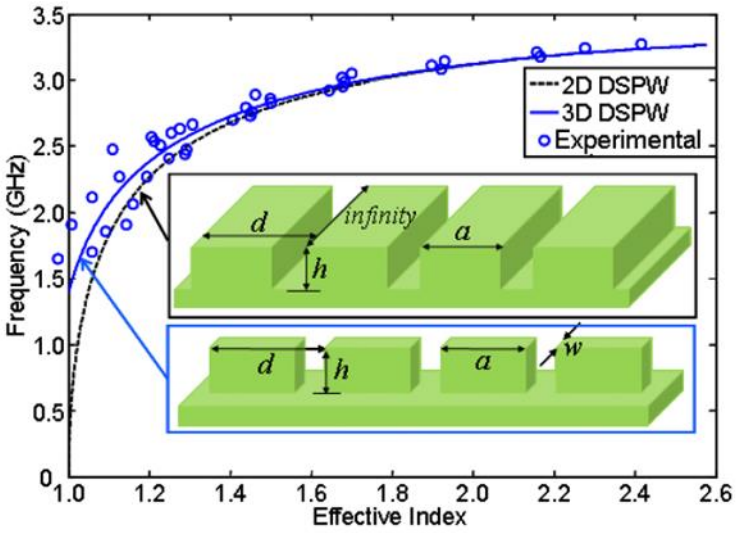

Figure 2.3 The dispersion diagram of DSP waveguides. The parameters of the waveguides are *d* = 12.7mm, *a* = 6.35mm, and *h* = 19.05mm. The width of the 2D DSP waveguide is assumed to be infinite; the width of the 3D DSP waveguide is *w* = 6.35mm. The circles indicate the measured dispersion relation for the 3D DSP waveguide. [85]

Theoretically, the propagation loss is very small because the 3D DSP waveguide supports a guided mode with small effective index (n_{eff} =1.2 at f=2.25GHz) and the small mode size supported by the waveguide is due to the interference of surface waves. The propagation attenuation mainly comes from the scattering due to fabrication imperfection. In our microwave device, the attenuation is very small and cannot be accurately measured within a short propagation distance.

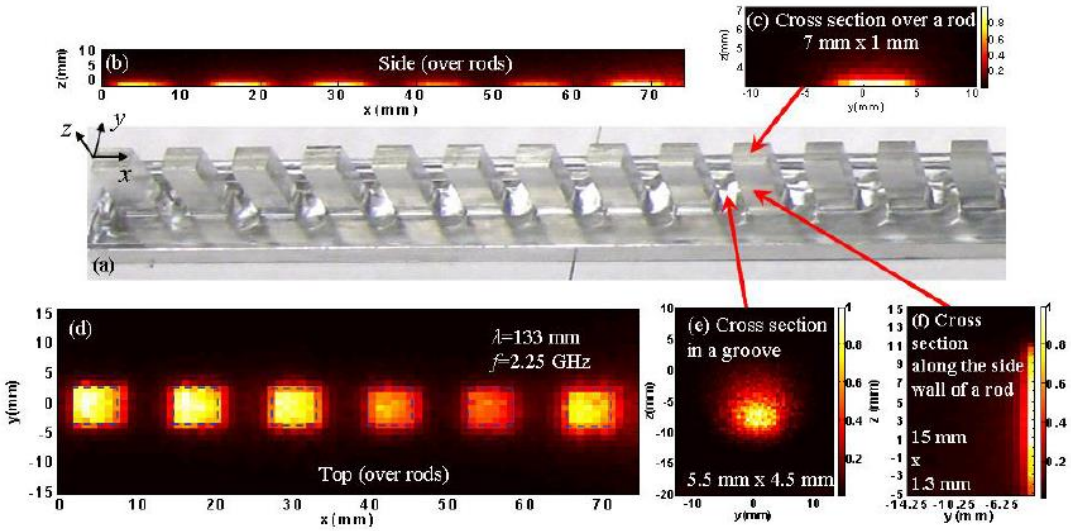

Figure 2.4 (a) The fabricated 3D DSP waveguide. The measured mode profiles (shown in normalized intensity) in different directions: (b) Side (over rods, in *x*-*z* plane), (c) Cross section over a rod (in *y*-*z* plane), (d) Top view (over rods, in *x*-*y* plane), the dashed blue squares indicate the positions of the metal rods, (e) Cross section in a groove (in *y*-*z* plane), (f) Cross section along the side wall of a rod (in *y*-*z* plane). [85]

2.3.2 3D directional coupler

To further demonstrate the function of the metal grating as a deep subwavelength DSP waveguide, we aligned two identical waveguides in parallel and formed a directional coupler as shown in Fig. 2.5(a). The EM source was then fed from one of the waveguides. Figure 2.5(b) shows that the EM wave switches between the waveguides at f = 3.25GHz. The distance between the two identical waveguides is 12.7mm (from center to center).

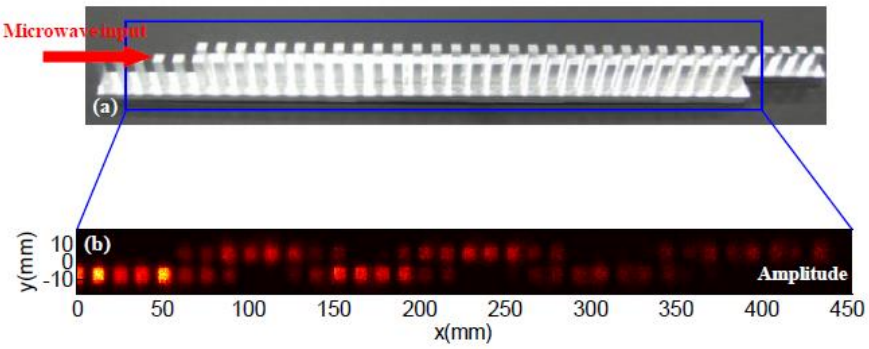

Figure 2.5 (a) Two DSP waveguides in parallel form a directional coupler. (b) The EM wave (shown in normalized amplitude) propagates in the directional coupler. [85]

2.3.3 Tapered 3D DSP waveguide

As shown in Fig. 2.3, the decrease of the waveguide width does not significantly affect the dispersion of the guided modes. This enables the mode-tapering in the transverse direction from a wide waveguide into deep subwavelength waveguide with high efficiency. The simulation of the taper in the terahertz regime was reported in recent work [63]. Our work in this aspect is focused on the experimental demonstration of this technique in the microwave regime. To this end, we fabricated a tapered DSP waveguide as the input of the uniform waveguide as shown Fig. 2.6(a). The waveguide is tapered from 203mm into 6.35mm within the distance of 216mm. In the experiment, we fed the taper with a monopole in the far end and partial EM waves are coupled to the taper. Figure 2.6(b) shows the measured intensity distribution on the device surface. As can be seen, when the EM waves propagate in the taper, the mode size becomes smaller and smaller with the intensity gradually increasing, and eventually EM waves are coupled into the deep subwavelength mode. This is an essentially squeezing or focusing process. Note that the tapered mode will be eventually end up as the guided mode of the 3D deep subwavelength DSP waveguide with dimensions 40mλ x 30mλ.

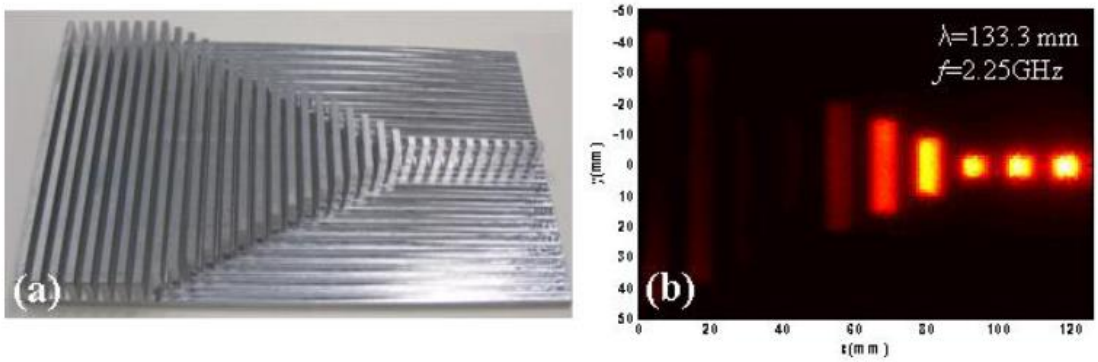

Figure 2.6 (a) The integration of the 3D subwavelength DSP waveguide with a tapered DSP waveguide as input. (b) Experimental result of normalized intensity distribution when EM waves are coupled from a 2D DSP waveguide and a 3D DSP waveguide. [85]

2.4 Conclusions

Compared to most *theoretical* work in designer surface plasmonic metamaterials [59-63,116], in this work, metal grating as a deep subwavelength DSP waveguide is *experimentally* investigated, where mode cross section down to 40mλ x 30mλ can be achieved in air. An efficient coupler for the deep subwavelength waveguide is also demonstrated, which provides a means to squeeze or focus EM waves into the deep subwavelength scale. It is worth noting that the modeling of the devices is based on perfect electric conductor (PEC) for metal and hence there is no difficulty to be scaled down into the THz regime, where metal can still be roughly treated as a PEC.

In addition, the working wavelength is scalable with the index of the surrounding medium as opposed to air. This is evident that when we immersed the device in low loss oil with refractive index $n_d \approx 2$, the working frequency shifted to approximate half of its original value. Thus, the mode size to wavelength ratio is inversely proportional to the refractive index. In particular, the mode size can be further shrunk into $0.01\lambda_0$-by-$0.02\lambda_0$ (λ_0 is the wavelength in free space), if silicon ($n_d \approx 3.5$) is coated on a 3D DSP waveguide in the THz regime. In Ref. [120], with silicon (at 0.6 THz) or germanium (at MIR region of 30 THz), numerical modeling via 3D FDTD has shown deep sub-wavelength mode confinement in transverse directions to smaller than $\lambda/50$ by $\lambda/50$, with an estimated propagation loss of less than 0.1 dB for each repetitive unit.

3 SUPER TALBOT EFFECT IN INDEFINITE ANISOTROPIC METAMATERIAL

In Chapter 2, an image size of 0.04λ-by-0.03λ can be achieved by metal gratings functioning as designer surface plasmonic (DSP) waveguide at *microwave* frequencies. In this chapter, we will re-visit a classical optical phenomenon named as Talbot effect and see that a comparable image size (~$0.087\lambda_0$) can be obtained at *visible* frequency via indefinite metamaterial. The Talbot effect (or the self-imaging effect) can be observed for a periodic object with a pitch larger than the diffraction limit of an imaging system, where the paraxial approximation is applied. The "super" Talbot effect can be achieved in an indefinite metamaterial even when the period is much smaller than the diffraction limit in both two-dimensional (2D) and three-dimensional (3D) numerical simulations, where the paraxial approximation is not applied. This is attributed to the evanescent waves, which carry the information about subwavelength features of the object, can be converted into propagating waves and then conveyed to far field by the metamaterial, where the permittivity in the propagation direction is negative while the transverse ones are positive. The indefinite metamaterial can be approximated by a system of thin, alternating multilayer metal and insulator (MMI) stack. As long as the loss of the metamaterial is small enough, deep subwavelength image size (~$0.087\lambda_0$) can be obtained in the super Talbot effect [121].

3.1 Introduction

3.1.1 TE and TM waves

In the electromagnetic waves, both the electric field and the magnetic field are oscillating in different directions. The polarization of the EM wave refers to the direction of the electric field. In *parallel* polarization, also known as *p*-polarization, or TM polarization, the electric fields lie on

the plane of incidence and the magnetic fields are perpendicular to that plane (along *y*-direction) and transverse to the *z*-direction, as shown in Fig. 3.1(a). In *perpendicular* polarization, which is also known as *s*-polarization, or TE polarization, the electric fields are perpendicular to the plane of incidence (along *y*-direction) and transverse to the *z*-direction, and the magnetic fields lie on that plane, shown in Fig. 3.1(b).

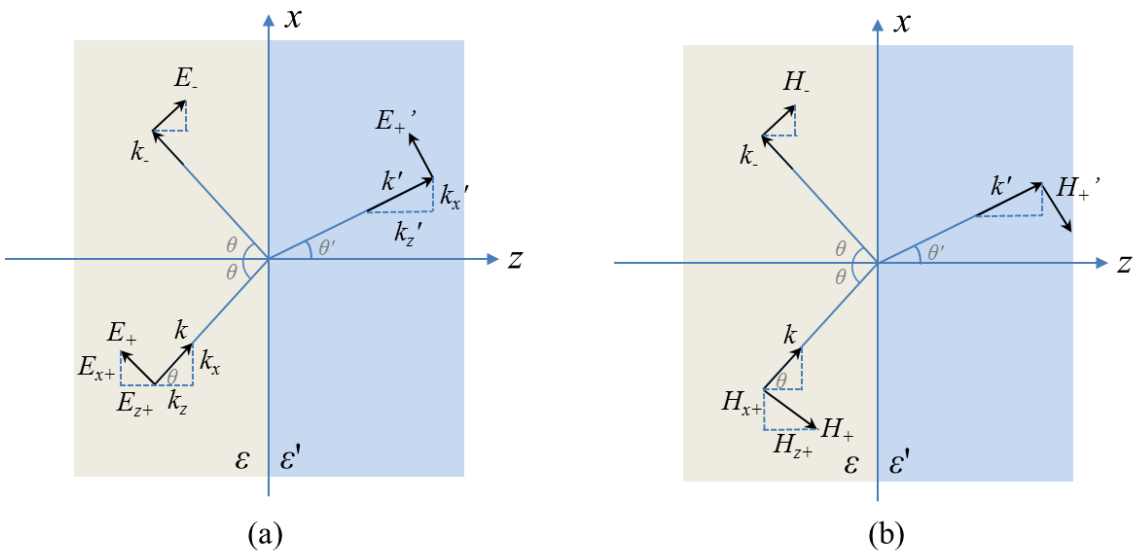

Figure 3.1 Illustration of oblique incidence for (a) TM- and (b) TE-polarized light.

Now we consider that the interface shown in Fig. 3.1(a) and (b) is between a dielectric and a metal, shown as Fig. 3.2(a). We will apply Maxwell's equations in Eq. (3.1a-d) to the flat interface and investigate the physical properties of surface plasmon polaritons (SPPs) [41,42], which is known as electromagnetic excitations propagating at the interface and evanescently confined perpendicular to the interface. These equations describe how the electric field *E* and magnetic field *H* are generated and altered by each other and by external charge density ρ and current density *J*.

$$\nabla \bullet \boldsymbol{D} = \rho \tag{3.1a}$$

$$\nabla \bullet \boldsymbol{B} = 0 \tag{3.1b}$$

$$\nabla \times \boldsymbol{E} = -\frac{\partial B}{\partial t} \tag{3.1c}$$

$$\nabla \times \boldsymbol{H} = \boldsymbol{J} + \frac{\partial D}{\partial t} \tag{3.1d}$$

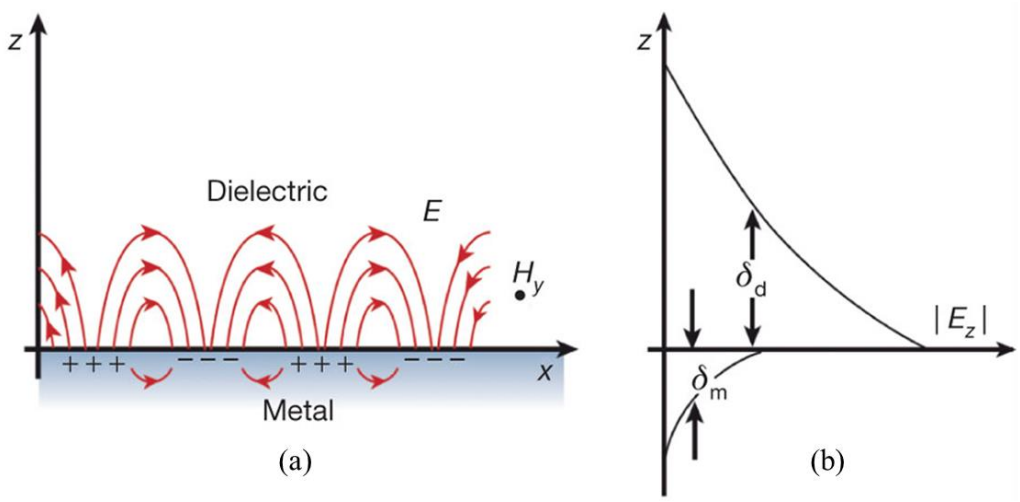

Figure 3.2 (a) Illustration of a SPPs as a collective excitation at a metal-dielectric interface. The electric field *E* and magnetic field *H* are enhanced at the interface. (b) The perpendicular field E_z decays exponentially with a characteristic length δ_d in the dielectric and δ_m in metal. [122]

Using the curl Eqs. (3.1c-d), for harmonic time dependence ($\frac{\partial}{\partial t} = -j\omega$), and propagation along the x-direction ($\frac{\partial}{\partial t} = j\beta$), we can have the following set equations,

$$\frac{\partial E_y}{\partial z} = -j\omega\mu_0 H_x \tag{3.2a}$$

$$\frac{\partial E_x}{\partial z} - j\beta E_z = j\omega\mu_0 H_y \tag{3.2b}$$

$$j\beta E_y = j\omega\mu_0 H_z \tag{3.2c}$$

$$\frac{\partial H_y}{\partial z} = j\omega\varepsilon_0\varepsilon E_x \tag{3.2d}$$

$$\frac{\partial H_x}{\partial z} - j\beta H_z = -j\omega\varepsilon_0\varepsilon E_y \tag{3.2e}$$

$$j\beta H_y = -j\omega\varepsilon_0\varepsilon E_z \tag{3.2f}$$

Equation set (3.2a-c) are the transverse magnetic (TM or *p*) mode, where only the field components E_x, E_z and H_y are nonzero, and the second set (3.2d-f) are the transverse electric (TE or *s*) mode, with only H_x, H_z and E_y are nonzero.

For TM modes, the equation set can be simplified to

$$E_x = -j\frac{1}{\omega\varepsilon_0\varepsilon}\frac{\partial H_y}{\partial z} \tag{3.3a}$$

$$E_z = -\frac{\beta}{\omega\varepsilon_0\varepsilon}H_y \tag{3.3b}$$

and the wave equation for the TM mode is

$$\frac{\partial^2 H_y}{\partial z^2} + \left(k_0^2\varepsilon - \beta^2\right)H_y = 0. \tag{3.3c}$$

For TE modes the equation set is

$$H_x = j\frac{1}{\omega\mu_0}\frac{\partial E_y}{\partial z} \tag{3.4a}$$

$$H_z = \frac{\beta}{\omega\mu_0}E_y \tag{3.4b}$$

and the TE wave equation is

$$\frac{\partial^2 E_y}{\partial z^2} + \left(k_0^2\varepsilon - \beta^2\right)E_y = 0. \tag{3.4c}$$

From Eqs. (3.4a-c), for TE mode, the expressions for the field components in half spaces shown in Fig. 3.2(a) are

$$E_y(z) = A_2 e^{j\beta x}e^{-k_2 z} \tag{3.5a}$$

$$H_x(z) = -jA_2\frac{1}{\omega\mu_0}k_2 e^{j\beta x}e^{-k_2 z} \tag{3.5b}$$

$$H_z(z) = A_2 \frac{\beta}{\omega\mu_0} e^{j\beta x} e^{-k_2 z} \tag{3.5c}$$

for $z > 0$ and

$$E_y(z) = A_1 e^{j\beta x} e^{k_1 z} \tag{3.5d}$$

$$H_x(z) = jA_1 \frac{1}{\omega\mu_0} k_1 e^{j\beta x} e^{k_1 z} \tag{3.5e}$$

$$H_z(z) = A_1 \frac{\beta}{\omega\mu_0} e^{j\beta x} e^{k_1 z} \tag{3.5f}$$

for $z < 0$. In these equation sets, $k_i \equiv k_{i,z}\,(i = 1, 2)$ is the wave component perpendicular to the interface. From boundary condition – the continuity of E_y and H_x at the interface leads to

$$A_1(k_1 + k_2) = 0. \tag{3.6}$$

To get the confinement at the interface, it requires that $Re(k_1) > 0$ and $Re(k_2) > 0$. In Eq. (3.6) this condition is only fulfilled when $A_1 = 0$, therefore $A_2 = A_1 = 0$. Hence, there is no surface mode exists with TE polarization.

On the other hand, for TM polarization, the field expressions are

$$H_y(z) = A_2 e^{j\beta x} e^{-k_2 z} \tag{3.7a}$$

$$E_x(z) = -jA_2 \frac{1}{\omega\mu_0} k_2 e^{j\beta x} e^{-k_2 z} \tag{3.7b}$$

$$E_z(z) = -A_1 \frac{\beta}{\omega\varepsilon_0\varepsilon_2} e^{j\beta x} e^{-k_2 z} \tag{3.7c}$$

for $z > 0$ and

$$H_y(z) = A_1 e^{j\beta x} e^{k_1 z} \tag{3.7d}$$

$$E_x(z) = -jA_1 \frac{1}{\omega\mu_0} k_1 e^{j\beta x} e^{k_1 z} \tag{3.7e}$$

$$E_z(z) = -A_1 \frac{\beta}{\omega\mu_0} e^{j\beta x} e^{k_1 z} \tag{3.7f}$$

for $z < 0$. According to boundary conditions, the continuity of H_y and $\varepsilon_i E_z$ at the interface leads to $A_1 = A_2$ and $\frac{k_2}{k_1} = -\frac{\varepsilon_2}{\varepsilon_1}$. Thus, surface plasmon polaritons only exist for TM polarization at the interface between materials with opposite signs of the real part of their dielectric permittivity, i.e. a conductor and an insulator. The perpendicular wave vectors' reciprocal values δ_d and δ_m define the evanescent decay lengths in dielectric and metal perpendicular to the interface, respectively, as shown in Fig. 3.2(b).

As we introduced in Chapter 1, most metamaterials are composed by artificially designed structures with metallic and dielectric materials. The novel properties of the metamaterials are enabled by the interaction of incident light with the metal-dielectric materials, where the light is transformed into electromagnetic waves of a different variety – surface plasmon polaritons.

3.1.2 Classical Talbot effect

The Talbot effect was originally discovered by H. F. Talbot in 1830s [123]. The self-imaging phenomenon is a direct result of Fresnel diffraction [124], which can be observed for a periodic object when illuminated by a monochromatic light. Over many years, different aspects of this phenomenon have been investigated and understood by researchers, and the theory of the Talbot effect based on diffraction theory [124-129] has been established. The field amplitude is observed to be periodic in both the transversal and light propagation directions behind the object, illustrated in Fig. 3.3. A monochromatic, coherent plane wave with a wavelength of λ is illuminating an infinitely long grating. In Fourier optics, such a periodic object can be represented as

$$A(x) = \sum_{n=-\infty}^{\infty} c_n e^{\frac{2\pi i n x}{d}}, \tag{3.8}$$

where d is the spatial period, and c_n is the amplitude of the nth harmonic.

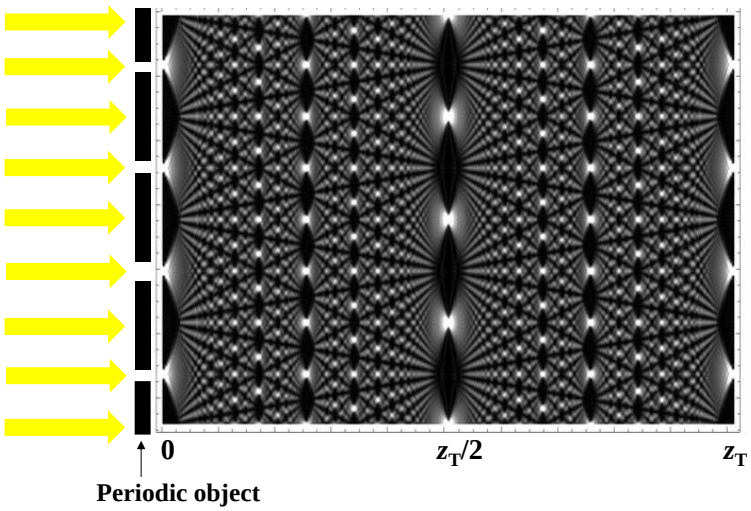

Figure 3.3 Illustration of the optical Talbot effect, shown as a Talbot carpet. [130]

The diffracted field amplitude $E(X)$ is defined in terms of the amplitude transmission of the object $A(x)$ and the coherent amplitude of the source $S(x_s)$, according to the Fresnel-Kirchhoff diffraction theory [131], where X, x, and x_s are Cartesian coordinates in the observation, object, and source planes, respectively. In the paraxial approximation, the diffraction amplitude $E(X)$ at a distance z from the object is proportional to

$$E(X) \propto \int_{-\infty}^{\infty} dx A(x) e^{i\frac{2\pi}{\lambda}\left(z+\frac{X^2}{2z}-\frac{xX}{z}+\frac{x^2}{2z}\right)}. \tag{3.9}$$

By substituting Eq. (3.8) into Eq. (3.9), we can get

$$E(X) \propto \sum_{n=-\infty}^{\infty} c_n e^{-i\frac{\pi\lambda n^2 z}{d^2}} e^{i\frac{2\pi nX}{d}}. \tag{3.10}$$

At a certain distance z, all diffraction orders are in phase by satisfying the condition

$$z = 2m\frac{d^2}{\lambda}, \tag{3.11}$$

where m is a positive integer and referred as the self-imaging number, and d is the period of the diffraction grating. From Eq. (3.11), the Talbot distance is defined as

$$Z_T = \frac{2d^2}{\lambda} \tag{3.12}$$

At $z = Z_T$, the primary Talbot image is observed in Fig. 3.3, and at $z = Z_T/2$ is the Talbot distance of the secondary Talbot image, where the image has a $d/2$ shift along the transversal direction. The fractional Talbot images are observed at all rational multiples of Z_T, which can be expressed as

$$z = \frac{p}{q} Z_T, \tag{3.13}$$

where p and q are prime integers.

Due to its simple arrangement, the Talbot effect attracts researchers' interests and the self-imaging phenomenon has a variety of applications in the optical dispersive fiber system [132,133], optical computing [134], phase locking of laser arrays [135], and in electron optics and microscopy [136]. The Talbot effect has also been demonstrated with atomic waves [137], and waveguide arrays [138,139].

3.1.3 Talbot effect in plasmons

Studying the analogues of the classical optical phenomena is an important aspect of the development of new branches of optics. Surface plasmon polaritons (SPPs) is well known for their advantages, for example, they can concentrate the electromagnetic field near the metal/dielectric interface, therefore enabling compact light waveguiding [140]. In 2007, Dennis and Zheludev, *et. al.*, first proposed the concept of the plasmon Talbot effect [141]. The analog of the Talbot effect in plasmons is illustrated in Fig. 3.4(a), where a plane wave is incident from the back of a metal film, with a periodic one-dimensional array of subwavelength hole structures, with period a. The complex carpet patterns shown in Fig. 3.4(c)-(d) are generated on the incident light exiting surface by the plasmons converted by part of the incident light. Each subwavelength hole can be modeled as a dipole, oscillating with a wavelength of λ_0, which is the incident wavelength. The converted

surface plasmons has a wavelength of $\lambda_{SP} = \frac{\lambda_0}{Real\left[\sqrt{\frac{\varepsilon}{1+\varepsilon}}\right]}$, where ε is the frequency-dependent dielectric constant of the metal. In this scenario, the Talbot length is derived to be

$$Z_T = \frac{2a^2}{\lambda_{SP}}, \tag{3.14}$$

The amplitude of the electric field E_z component of a plane with z=0.5μm above the metal surface is plotted in Fig. 3.4(b)-(e), where the incident wavelength λ_0=1.55μm and λ_{SP}=1.544μm. As seen in Fig. 3.4(b), with the period a=λ_{SP}, although a periodic pattern is developed, the Talbot effect is not observed. With a larger period a, the self-imaging phenomenon is clearly shown in Fig. 3.4(c)-(e).

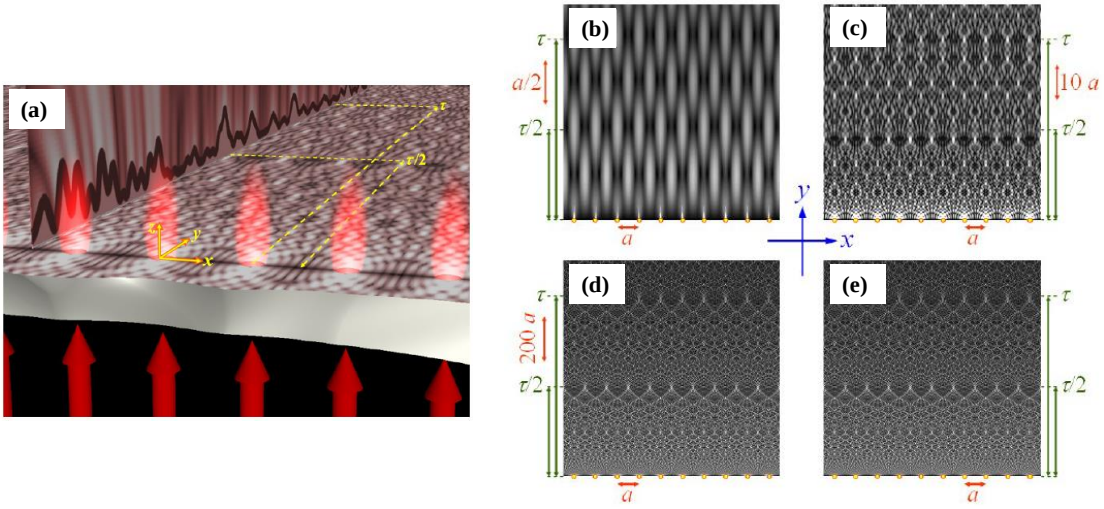

Figure 3.4 (a) Illustration of the plasmon Talbot effect above a metal surface. Numerically computed plasmon Talbot carpets for a metal film drilled by an array of nanoholes with different periods a: (b) $a=\lambda_{sp}$, (c) $a=5\lambda_{sp}$, (d) and (e) $a=20\lambda_{sp}$. [141]

As the plasmonic Talbot effect has wide potential applications, experimentally investigation of this effect is important as well. In 2009, the first plasmonic self-imaging experiment was performed [142] by using SPP launching gratings (SPPLGs), which consist of periodic grooves drilled on a gold film. The SPPLGs can be characterized by an opening ratio $\alpha=a/d$, as shown in Fig. 3.5(a). Two different SPPLGs are fabricated with the periods of $3\lambda_{SP}$ and

$6\lambda_{SP}$, respectively, and the opening ratio α = 0.5 for both SPPLGs. As a *y*-polarized laser beam is normally illuminating on the SPPLGs, the SPPs are excited at the grooves and propagate to form Talbot carpet. Figure 3.5(b) and (c) show the experimental results, where periodic patterns are clearly observed along both the transversal and longitudinal directions.

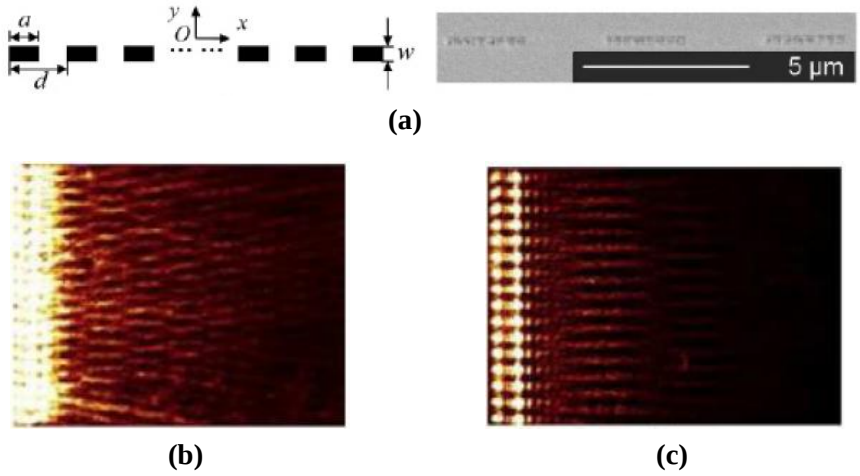

Figure 3.5 (a) Left: Illustration of the SPPLGs. Right: scanning electron micrograph of the SPPLG with $d=6\lambda_{sp}$ and $\alpha=1/2$. Experimental Talbot carpets for the SPPLGs with $d=3\lambda_{sp}$ (b) and $d=6\lambda_{sp}$ (c), respectively. [142]

3.2 Design and Modeling

3.2.1 Structure design

Figure 3.6(a) schematically illustrates a two-dimensional (2D) structure investigated in the numerical simulations. A one-dimensional periodic grating is put in front of a medium, which is either conventional material (for example, air) or indefinite metamaterial. The period of the grating is *D*, and the duty cycle is expressed as *d*/*D*. A TM-polarized plane wave (magnetic field is in the *y*-direction) with a wavelength of λ_0 propagates along *z*-axis and impinges the grating from the left side. A three-dimensional (3D) structure was also investigated, where the grating along both *x* and *y* axes was periodic.

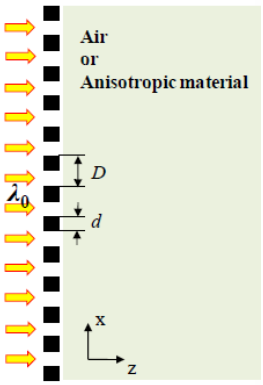

Figure 3.6 Schematic illustration of the investigated structure, the 1D grating is assumed to be infinite along *y*-axis. [121]

3.2.2 Talbot distance in indefinite metamaterial

Since the wavelength λ_0 is much larger than the period D, the paraxial approximation cannot be applied any more. In our case, light propagates in the indefinite metamaterial behind the input grating structure can be expressed in Fourier series form as

$$T(x,z) = \sum_m f_m e^{jmq_x x} e^{jk_z z}, \tag{3.15}$$

where $q_x=2\pi/D$, and k_z is expressed by Eq. (1.2), which is $k_z = \sqrt{\varepsilon_x \left(k_0^2 - \frac{k_x^2}{\varepsilon_z}\right)}$. Replacing k_x by mq_x in Eq. (1.2) and then plugging Eq. (1.2) into Eq. (3.15), we get

$$T(x,z) = \sum_m f_m e^{jmq_x x} e^{jzk_0 \sqrt{\varepsilon_x}\sqrt{1+\frac{m^2}{-\varepsilon_z}\left(\frac{q_x}{k_0}\right)^2}}, \tag{3.16}$$

Under long wavelength approximation, $\lambda_0 >> D$ and hence $q_x/k_0 >>1$, so Eq. (3.16) can be further simplified as

$$Z_T \approx \sqrt{\frac{-\varepsilon_z}{\varepsilon_x}} D, \tag{3.17}$$

which only depends on the permittivity components of the metamaterial and the input object period. Note the permittivity of a metamaterial is highly frequency-dependent. Using Eq. (3.17), the Talbot distance in the indefinite metamaterial (with ε_z = -1 and ε_x = 1) can be calculated approximately as

100nm, while the Talbot distance measured in the simulation is around 117nm. The difference may come from that the ratio of the wavelength λ_0 and the period D is only around 6.3 while Eq. (3.17) is based on the condition that $\lambda_0 >> D$.

3.3 Results and Discussion

3.3.1 Talbot effect without paraxial approximation

Classical Talbot effect can only be observed under paraxial approximation, where the incident wavelength should be much smaller than the period of the grating. Here, the focus is put on the opposite condition, where the wavelength is larger than the period. For the 2D structure shown in Fig. 3.7, the period of the grating D is 100nm, d is 50nm and the incident wavelength λ_0 is 630nm. In a conventional material, the evanescent waves which carry the information about the subwavelength features of the object will decay exponentially. Hence, if the period of the input object is much smaller than the incident wavelength, no Talbot effect can be seen in the regular material (as shown in Fig. 3.7(a), in the air). In contrast to the case in the air, self-imaging effect can be achieved in an indefinite metamaterial, which is due to the evanescent waves being converted into propagating waves and conveyed far away. This self-imaging effect observed in the indefinite metamaterial when the period of the object much smaller than the incident wavelength is defined as "super Talbot effect" in this paper. Figure 3.7(b) clearly shows the strong, periodic magnetic field distribution pattern in the indefinite metamaterial (with $\varepsilon_z = -1$ and $\varepsilon_x = 1$) behind the input grating. This effect is related to but also distinct from the plasmon Talbot effect reported in recent work [141,142], where *surface* plasmon Talbot effect is observed on the *surface* of metal and its resolution is still limited by the surface plasmon diffraction limit. In contrast, our super Talbot effect is based on *bulk* plasmons without diffraction limit.

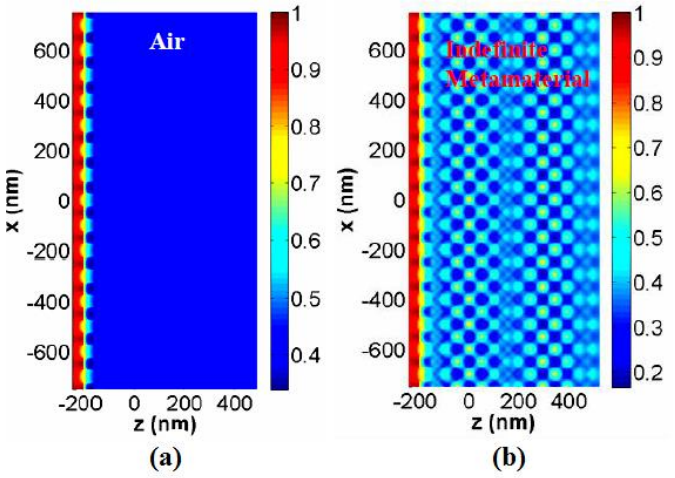

Figure 3.7 Without paraxial approximation: (a) No Talbot effect is seen in air. (b) Periodic Talbot carpet pattern can be observed in indefinite metamaterial (shown in normalized *H* field distribution). [121]

3.3.2 Classical Talbot effect in indefinite metamaterial

To better understand the super Talbot effect, the self-imaging of a large-pitch mask (D = 2 μm and d = 100nm) in a conventional medium and in an indefinite metamaterial was also modeled, respectively. As shown in Fig. 3.8(a), the Talbot effect can be observed in a conventional material (for example in the air) under paraxial approximation, where the incident wavelength is still 630nm. If the medium behind the grating is replaced by an indefinite metamaterial with ε_z = -1 and ε_x = 1, the Talbot carpet pattern still can be clearly observed (shown in Fig. 3.8(b)). The feature size of the squared hot spot in Fig. 3.8(b) along the transverse direction measured is approximately as 160nm, which is much smaller than that in the air, 240nm. The result is within our expectation since the high spatial-frequency waves can be conveyed to far field in the indefinite metamaterial, as mentioned previously.

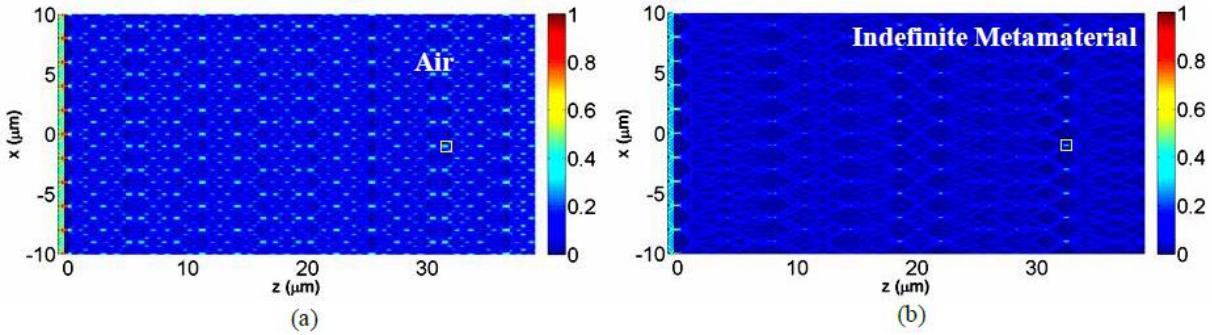

Figure 3.8 Talbot effect in (a) air, and (b) indefinite metamaterial. Both are shown in normalized power distribution. [121]

3.3.3 Super Talbot effect in indefinite metamaterial

As mentioned previously in Section 1.2.3, indefinite metamaterial can be approximated by a system of thin, alternating multilayer metal-insulator (MMI) stack. In this work, Ag and SiO_2 were selected as the metal and insulator, respectively. The structure we investigated is similar as shown in Fig. 3.4, where the material behind the grating was replaced by the MMI stack composed of Ag and SiO_2 thin layers and they were assumed to be infinite in *y*-axis. The alternating layers were stacked in the *x* direction and each layer has a thickness of 5nm. In the simulations, periodic boundary conditions were implemented for the boundaries parallel to the *z*-axis. The wavelength of the incident TM-polarized plane wave λ_0 = 630nm, the period of the grating D = 94nm and the duty cycle = 50%. At the wavelength of interest, the permittivity of Ag is ε_{Ag} = -15.69 + j1.06 and that of SiO_2 is ε_{SiO2} = 2.12. As η = 1, from Eq. (1.3) the effective permittivity of the MMI stack is calculated to be ε_z = -6.79 + j0.53 and ε_x = 4.9 + j0.05. Even the material loss is considered, the super Talbot effect is still obvious as shown in Fig. 3.9(a). Figure 3.9(b) plots the cross-sectional profile of the power in *z*-axis (where x = 52nm, the horizontal white solid line in the figure). Each of the peaks numbered from 1 to 7 of the curve represents the location of one Talbot imaging plane where the self-imaging phenomenon occurs. The intensity gradually decays due to the attenuation of the MMI stack. The distance between the two adjacent peaks is the Talbot distance Z_T, which is

approximately measured as 152nm. The Talbot distance calculated by Eq. (3.17) is around 110nm. Both the effective medium theory and the long wavelength approximation may contribute to the difference. If the attenuation of the MMI stack is negligible, deep subwavelength image size can be achieved in the super Talbot effect. At point 1, where z = 40nm (along the first dashed vertical line as shown in Fig. 3.9(a)), the full-width half-maximum (FWHM) of one image hot spot is measured as 35 nm (or $0.056\lambda_0$). At another Talbot imaging plane, where z = 642nm (point 5 in Fig. 3.9(b), along the second dashed vertical line in Fig. 3.9(a)), a subwavelength image size of 55nm (or $0.087\lambda_0$) still can be achieved. Comparing the cross-sectional power profiles of point 1 and point 5 (which are not shown in the paper), the contrast of the power at point 5 is not as sharp as that of point 1 and the quality of the image is worse, which are attributed to the loss of high-order diffraction light in the MMI stack.

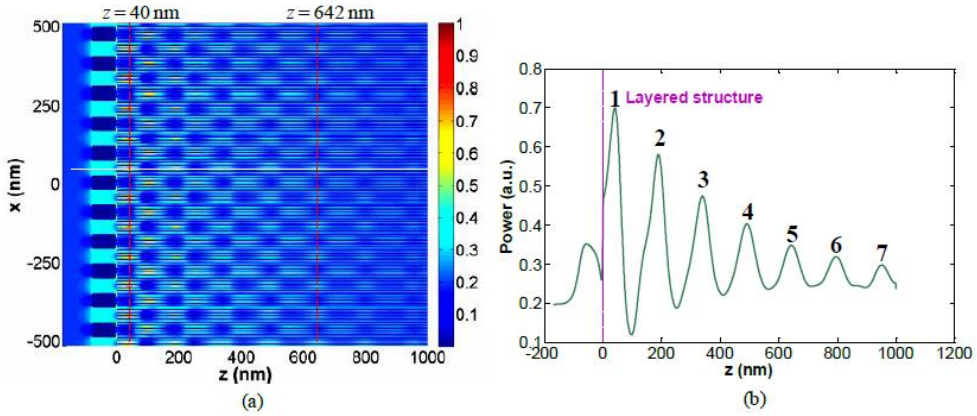

Figure 3.9 (a) Super Talbot effect in an Ag-SiO2 stack (shown in normalized power). (b) Cross-sectional power profile along the white solid line shown in (a), where x = 52nm. [121]

3.3.4 Super Talbot effect demonstrated in 3D simulations

When considering the realistic applications, for example in nanolithography, where usually the pattern on the mask in the *y*-axis is also periodic, the super Talbot effect in a 3D configuration needs to be explored. Here we mimic a simple scenario in nanolithography, where light is incident from a chrome (Cr) mask with periodic subwavelength holes, as shown in Fig. 3.10(a). The

incident plane wave is polarized in *x*-axis and has a wavelength of 630nm. The parameters of the hole-array are as below: hole diameter $2r$ = 80nm and the periods along the *x* and *y* axes are identical as D = 150nm. For simplicity, behind the Cr (ε_{Cr} = -6.3 + *j*31.2) mask is an indefinite metamaterial which is assumed to be lossless and the permittivity components are ε_z = -4, and ε_x = ε_y = 1. The origin of the whole system is defined at the center of the hole (marked with the red solid circle) with z = 0 at the interface between the Cr mask and the indefinite metamaterial.

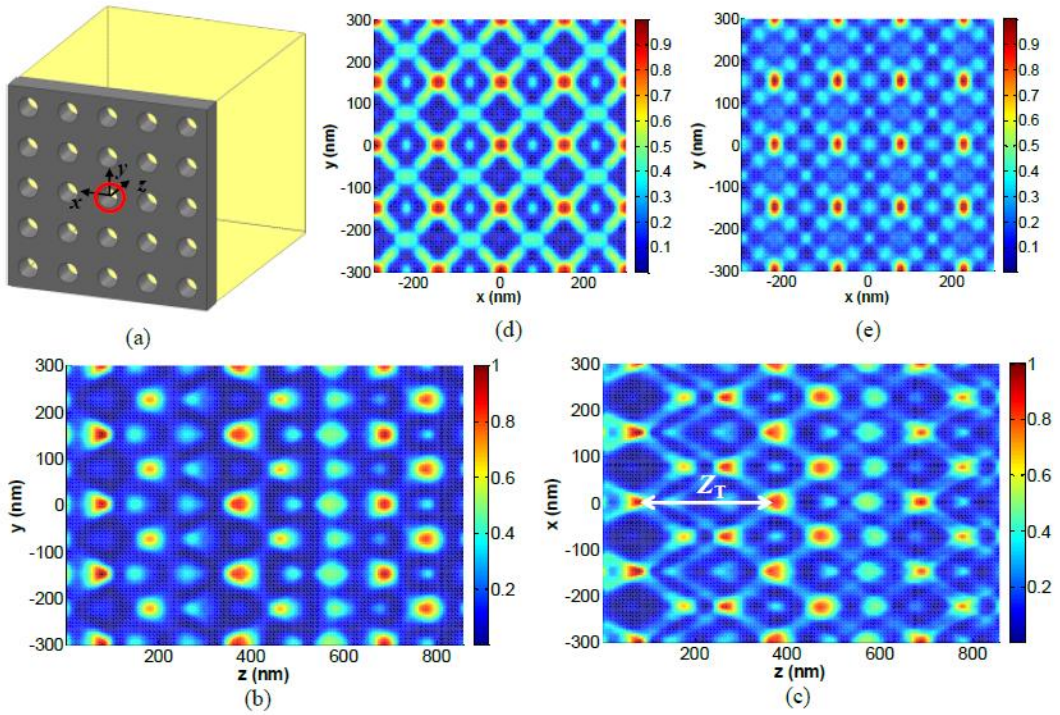

Figure 3.10 (a) Illustration of the structure. Hole diameter: $2r$ = 80nm, hole array periods: D = 150nm along *x* and *y* axes. Incident wavelength is λ_0 = 630nm. (b) The Talbot carpet pattern in the vertical *z*-*y* plane at x = 0. (c) Talbot carpet pattern in the horizontal *z*-*x* plane at y = 0. (d) One integer Talbot imaging plane. (e) One fractional Talbot imaging plane with z =2/3Z_T. (b-e) are shown in normalized $|E|^2$. [121]

In Fig. 3.10(b), the $|E|^2$ distribution of the vertical *z*-*y* plane at x = 0 is depicted, and similarly, Fig. 3.10(c) for the horizontal *z*-*x* plane at y = 0. Clearly, the super Talbot effect can be obtained in both the vertical and horizontal planes. The Talbot distance Z_T (as shown in Fig. 3.10(c)) measured is about (300 ± 15) nm, which agrees with the result from Eq. (3.17), calculated as

300nm. The asymmetric pattern distributions as shown in Fig. 3.10(b) and 3.10(c) may be attributed to the polarization dependent effect. Figure 3.10(d) shows the image in one of the Talbot imaging planes (*x*-*y* plane, z = 365nm). The positions of the hot spots coincide with those of the periodic holes on the Cr mask. The size of each hot spot (FWHM) is approximately 40nm-by-40nm (or $0.0635\lambda_0$-by-$0.0635\lambda_0$). Besides the integer self-imaging planes, we also observed some fractional Talbot imaging planes which locate between two adjacent integer Talbot planes [143], with $z = p/qZ_T$ (p and q are prime integers). One representative fractional Talbot imaging plane with $z \approx 2/3Z_T$ was shown in Fig. 3.10(e). Comparing with the integer Talbot imaging plane [Fig. 3.10(d)], the image on the fractional Talbot imaging plane as shown in Fig. 3.10(e) has the same spatial frequency but is shifted about 0.5 periods (75nm) along x-axis. The image size (FWHM) of those hot spots is measured as 30nm-by-40nm (or $0.0476\lambda_0$-by-$0.0635\lambda_0$).

Low loss 3D indefinite metamaterials may be constructed by an array of aligned metallic nanowires ($\varepsilon_m < 0$) embedded in a dielectric host ($\varepsilon_d > 0$). The fabrication of the nanowire-based metamaterial is based on a well-developed technique named "template synthetic method" [144-147] and with the pores filled by metals.

3.4 Conclusions

In conclusion, we have shown that super Talbot effect can be observed in an indefinite metamaterial without the paraxial approximation. A 2D indefinite metamaterial can be approximated by a multilayer metal-insulator stack for super Talbot applications. As long as the loss of the metamaterial is small enough, a deep subwavelength resolution (~$0.087\lambda_0$) can be achieved. Unlike the other plasmon Talbot effect discussed in Ref. [141,142], the super Talbot effect in this work is based upon bulk plasmon without diffraction limit. The super Talbot effect

may find a variety of applications in the fields as nanolithography and optical storage. In particular, 3D photonic crystals may be fabricated based the super 3D self-imaging phenomenon [148].

4 NANOPLASMONIC OPTICAL SWITCH BASED ON GA-SI_3N_4-GA WAVEGUIDE

In the previous two chapters, we introduced two different types of metamaterials -- designer surface plasmonic (DSP) waveguides [85] with periodic patterns on metal surface and an indefinite metamaterial consisting of alternative thin metal and dielectric layers [121], where in both cases the novel properties were achieved by man-made structures. In this chapter, we will see that a natural material – gallium (Ga), can also be treated as metamaterial, where the refractive index of gallium changes via the phase transitions of the material itself [149]. A numerical study of optical switch based on a metal-insulator-metal plasmonic waveguide with Si_3N_4 core sandwiched between two gallium (Ga) metal layers, is present [150]. Combining the unique structural phase transition property of gallium, within a total length of 400nm, an extinction ratio as high as 7.68 dB can be achieved in the proposed nanoplasmonic structure [150].

4.1 Introduction

Silicon is a prevalent, also a favorite choice in photonics, and silicon-based photonic components ranging from passive devices to active devices (like modulators, detectors, and light amplifiers) have been intensively investigated and developed [151-153]. On the other hand, silicon has the drawbacks of relatively low electro-optic coefficient and low light emission efficiency, which make silicon not a suitable for dense circuit component integration. A promising solution may be found in surface plasmon polaritons (SPPs), i.e. surface electromagnetic excitations coupled with collective electrons, which have intrigued considerable interest. Since SPPs exhibit extremely small guiding wavelengths and high field intensities along dielectric-metal interfaces, optical confinement can be scaled to deep subwavelength dimensions in plasmonic devices.

In recent years, considerable interest arises in the nonlinear effect enhancement by structural phase transitions in polyvalent metals, for example, Ga, which has already shown to enable all optical switching at mill watt power levels in thin films [154] and nanoparticles [155], as well as promises a new type of photodetector [156]. Gallium is a material known for its polymorphism [157]. The stable "ground-state" phase, α-gallium, is a highly anisotropic metal because molecular and metallic properties may coexist – some inter-atomic bonds are strong covalent bonds, forming well-defined Ga_2 molecules, and the rest are metallic bonds [149]. The structure is highly anisotropic, with much better thermal and electrical conductivity in the "metallic planes" than along the covalent bonds. The phase transitions between α-gallium and metallic gallium will occur when the temperature is close to the melting temperature of α-gallium, which is very low as 29.8 ℃. The switching may be achieved by external optical excitation or just simply changing the temperature of the metal with the switching time approximately in the picosecond-microsecond range [158]. The significant difference in the optical properties of α-phase and metallic phase makes gallium a very suitable material for plasmonic modulators and switches, when α-gallium is near its melting point. However, gallium also presents another means to achieve metallic phase, by a non-thermal transition [158,159]. With high intensity femtosecond optical excitation, the molecular character of the α-gallium structure results in highly localized excitation of the dimers, due to the very fast localization of the photo-generated electron-hole pairs on the dimers. Therefore, light absorption can excite a dimer from the bonding to the anti-bonding state. Consequently, the α-gallium structure transits to a new configuration, as shown in Fig. 4.1, without near the melting temperature [149]. This process is called light-induced surface-assisted metallization [149].

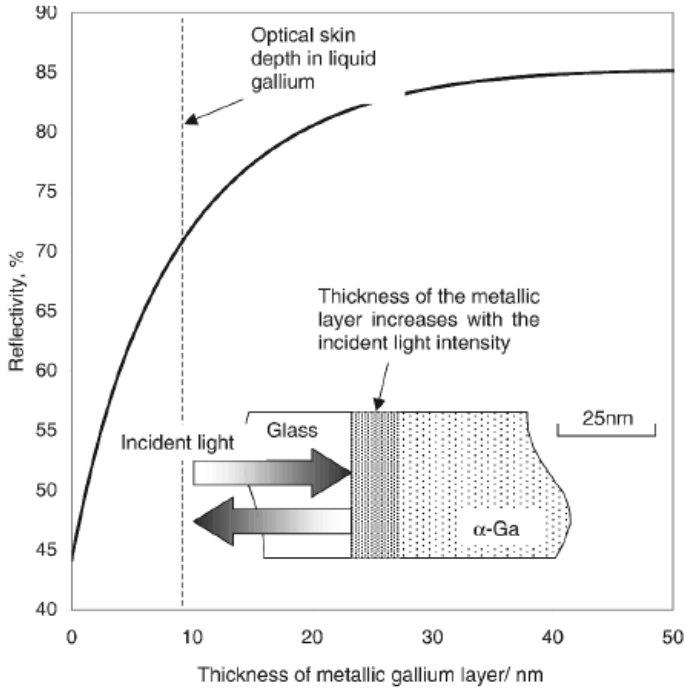

Figure 4.1 Surface light-induced metallization at a gallium-silica interface, at a wavelength of 1.55μm. [149]

In 2004, Krasavin and Zheludev proposed an active Au/Ga waveguide [154], which contains a 2.5μm long gallium switching layer, as illustrated in Fig. 4.2. The mechanism of the modulation is from the great different optical properties of the α-gallium and liquid gallium, in terms of the dielectric constants, $|\varepsilon_{liquid} - \varepsilon_{\alpha}| \sim 180$ at a wavelength of 1.55μm [154]. For a section of gallium waveguide 2.5μm-by-2.5μm the optical energy required for high-contrast switching will be on the order of 10 pJ. The intrinsic switch-on time was found to be 2-4 ps [160], which was measured on a gallium-quartz interface. The SPP switch-on time will be expected to be also on the scale of a few ps, while the switch-off to be in μs-ns time scale [158].

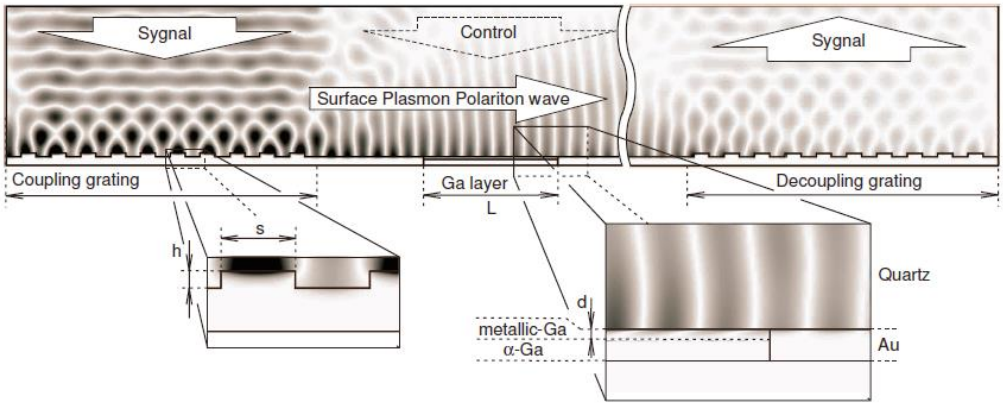

Figure 4.2 A SPP-based gold-on-quartz waveguide containing a gallium switching section, where gallium is at the bottom of the quartz substrate, shown in the magnitude of the magnetic field. [154]

4.2 Design and Modeling

Based on the previous work [154], in this work [150] the unique phase transition property of gallium is employed and the focus is put on the signal light transmission through a simple Ga-Si_3N_4-Ga waveguide. Finite-difference time-domain (FDTD) method [108,109] is used to investigate the switching properties of the plasmonic waveguide. In the FDTD simulations, the experimental data for the frequency-dependent dielectric constants of Ga is directly used [161,162], including both the real and imaginary parts for the three main crystalline axes (*a*-axis, *b*-axis, and *c*-axis) of α-gallium and the metallic gallium. At a wavelength of 1.55μm, the dielectric constants of different phase of gallium are: $\varepsilon_{\text{metallic}}$=-132.84+*j*134.77, $\varepsilon_{\alpha\_a\text{-}axis}$=-3.61+*j*23.79, $\varepsilon_{\alpha\_b\text{-}axis}$=-36.43+*j*21.79, and $\varepsilon_{\alpha\_c\text{-}axis}$ =2.83+*j*21.62. The simulated structure is created as a simple coupler by placing a Ga-Si_3N_4-Ga plasmonic waveguide embedded between two identical dielectric (silicon) waveguides, as shown in Fig. 4.3(a). The silicon waveguides and the Ga-Si_3N_4-Ga waveguide are aligned along the light propagation direction. The two silicon waveguides are used to couple optical signals into and out of the Ga-Si_3N_4-Ga waveguide, respectively. Recent work shows that high efficiency photonic-plasmonic-photonic coupling can be achieved through this configuration [163]. In order to calculate the power transmission of the Ga-Si_3N_4-Ga waveguide, a fundamental

TM mode in the input silicon waveguide is excited by a mode source. The power fluxes are measured in both the input and output silicon waveguides. Since the center of attention describes the switching characteristics of the plasmonic waveguide, the parameter optimization of the whole structure to achieve high extinction ratios, as well as waveguide transmission, will be discussed later in this chapter. The geometrical parameters of the silicon waveguides are temporarily put as: the width of the silicon waveguides, w_d = 400nm, the length of the Ga-Si_3N_4-Ga waveguide, l_p = 400nm, and the width of dielectric core, w_p = 60nm. Perfectly matched layers are used at all the boundaries of the simulation area to minimize the unnecessary reflection [164]. The spatial and temporal steps are set as $\Delta x = \Delta y$ = 2nm and $\Delta t = \Delta x/2c$ [165] respectively, to ensure accurate results in the FDTD simulations and c is the speed of light in free space.

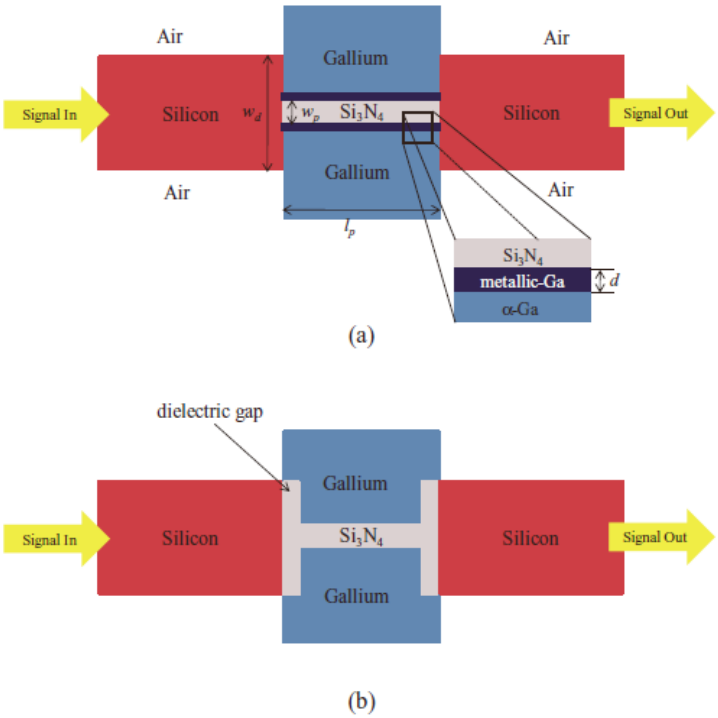

Figure 4.3 (a) A Ga-Si_3N_4-Ga plasmonic waveguide embedded between two silicon dielectric waveguides. (b) Dielectric gaps are introduced at both ends of the plasmonic waveguide. [150]

4.2.1 2D FDTD simulation results

We investigate the different conditions when external optical excitation is applied and hence, the phase of gallium parts may completely switch between the ground phase, α-gallium, and the metallic phase. The simulations include all main crystalline orientations of α-gallium. First, we consider the different transmissions of the waveguide at a wavelength of 1550nm. In the simulations, we assume that the gallium part is a homogeneous medium either in the α-phase or in the metallic phase. Figures 4.4(a) and 4.4(b) are the simulation results of the power distributions when the gallium is in the metallic phase and α-phase, CB (CB denotes the *c*-axis lying along the propagation direction and the *b*-axis lying along the transverse direction which is perpendicular to the Ga-Si_3N_4 interface, similar notations will be used in other figures), respectively. For a better comparison, the two figures are normalized to the maximum value of the result with metallic gallium. Simulation results with the α-gallium in other crystalline directions showed similar power distributions as shown in Fig. 4.4(b). The power transmission decreases from 24.8% (with metallic gallium) to less than 5.77%, depending upon a specific crystalline direction, 1.36% for AB, 2.72% for AC, 4.4% for BA, 5.77% for BC, 1.62 for CA, and 1.06% for CB. Here, we define at a given wavelength,

$$\text{Extinction ratio (in dB)} = 10\log\left(\frac{T_{\text{metallic}}}{T_{\alpha\text{-max}}}\right), \tag{4.1}$$

where $T_{\alpha\text{-max}}$ is the maximum transmission among those of the waveguide with α-gallium, and T_{metallic} is the transmission of the waveguide with metallic gallium at the same wavelength. Compared with the 2.5-μm long (the length of the gallium section, not including the lengths of the Au sections and the two 10 element coupling and decoupling gratings) structure in Ref. [154], an extinction ratio as high as 6.33 dB can be achieved in the simple Ga-Si_3N_4-Ga waveguide, with a

total length of only 400nm. This result is noticeable since the optical switch has been considered as a part of the integrated circuit, and the embedded structure is ready for fabrication. The detailed fabrication processes will be discussed in Section 4.3.

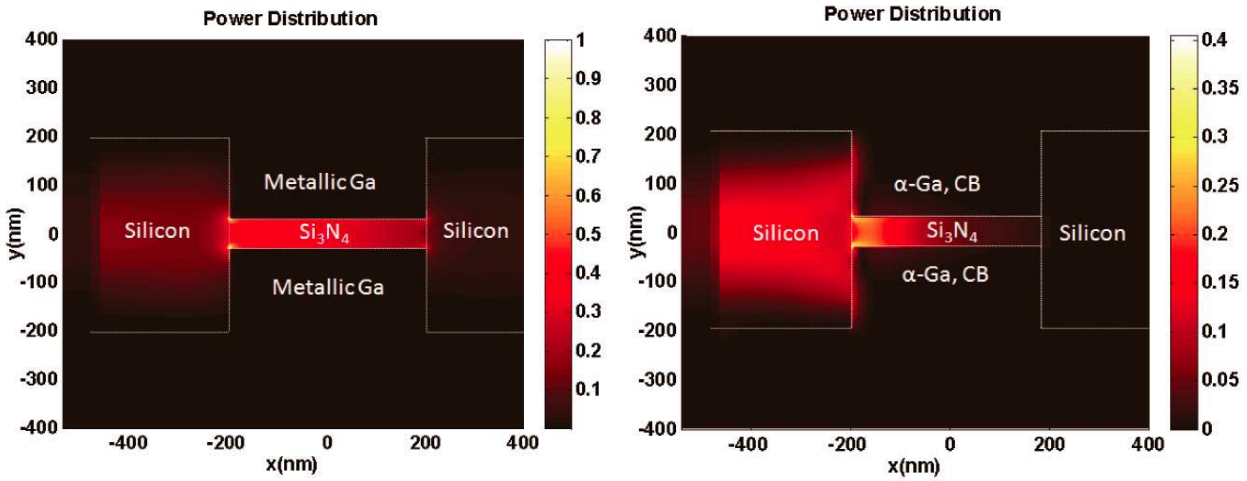

Figure 4.4 (a) Simulation result of field distribution with metallic gallium. (b) Simulation result of field distribution with *α*-gallium, CB [150]. Both plots are normalized with the result with metallic gallium.

To further investigate the performance of the modulator, we varied the working wavelengths of the optical switch from 1000 to 2000nm in the simulations. Figure 4.5 shows the transmissions at different wavelengths of incident light for the same structure. The most important information obtained from the simulation results is that the structural phase of the gallium is the main factor to determine the transmission of the Ga-Si_3N_4-Ga waveguide. From Fig. 4.5, we find that as the wavelength increases, the transmission levels for all the cases increase, except for the transmission of the waveguide with metallic gallium decreases at a very narrow wavelength range (1000 to 1070nm). We also note that an extinction ratio over 3 dB (not shown in Fig. 4.5) can be achieved at wavelengths approximately from 1160 to 2000nm. The reason can be attributed to the following: when the structural phase of gallium changes, the changed refractive index of gallium will cause the propagation loss as well as the impedance change. By carefully examining Fig. 4.5,

we found that at λ = 1360nm, the extinction ratio reaches its maximum, which is 7.68 dB.

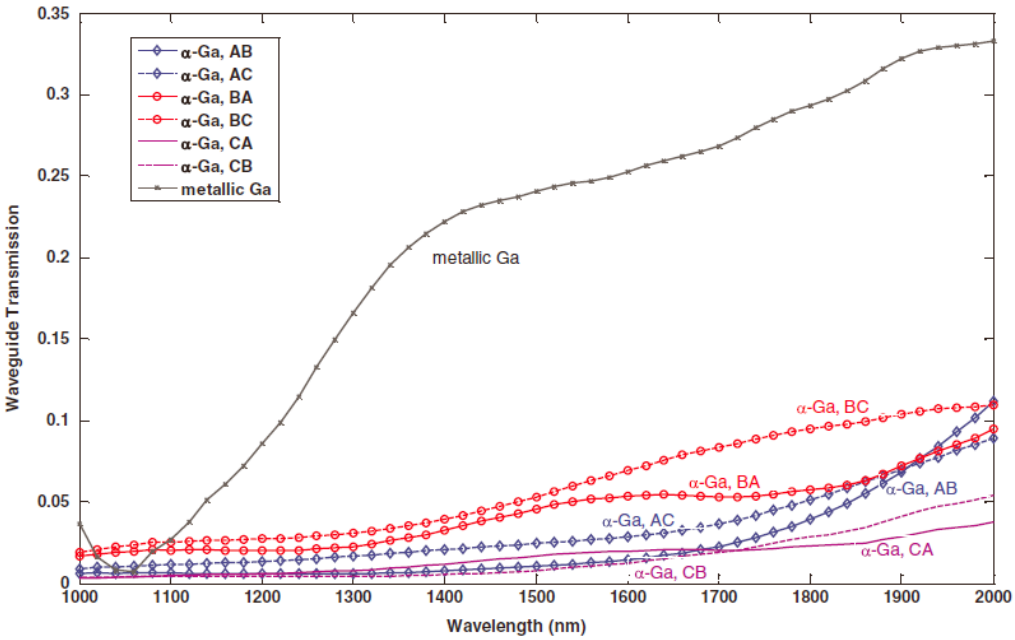

Figure 4.5 Power transmission of the Ga-Si_3N_4-Ga plasmonic waveguide as a function of wavelength for different phases and crystalline directions of gallium. [150]

Transitions between different structural phases in a bulk material are not reversible and therefore would not be suitable for controlling light with light. However, this will become a dynamic coexistence of structural forms if the material is placed in a restrictive geometry. The simplest form of confinement is the formation of an interface with another material [149]. The phase transition of gallium is a surface-mediated effect [154]. As shown in Fig. 4.3(a), a very thin layer of metallic gallium with thickness *d* is assumed to develop at Si_3N_4 and α-gallium interface. The thickness of metallic gallium layer *d* will steadily increase with either temperature just below the gallium bulk melting point or incident light intensity [149]. We simulate the conditions as the thickness *d* of metallic gallium continuously increases. The transmissions of the waveguide for a series of incident wavelengths and the corresponding extinction ratios are shown in Figs. 4.6(a) and 4.6(b), respectively. In the simulations, a thin layer metallic gallium is sandwiched between

Si_3N_4 and α-gallium, CB. The simulated structure and main geometric parameters are kept the same as the previous simulations. It is clearly seen that with the presence of tens of nanometers thick metallic gallium, the transmissions of the waveguide, as well as the extinction ratios, increase rapidly. This may be due to that only the metal in the vicinity of the metal-dielectric interface will be involved in the switching processes, since the field decays exponentially inside the metal at the interface. As shown in Fig. 4.6(b), at λ = 1550nm, with a 40-nm thick metallic gallium layer, the extinction ratio reaches around 9.98 dB and the transmission increases to 10 times of its original value [see Fig. 4.6(a)]. The plasmonic waveguide with metallic gallium represents an "on" state while with α-gallium represents an "off" state. The transmission of the waveguide with metallic gallium can be improved by choosing the optimal geometric parameters of the waveguide or simply introducing dielectric gaps to the structure, as shown in Fig. 4.3(b). Those gaps may function like "funnels" to gather more SPPs to the dielectric core of the waveguide [165]. With two 40-nm wide gaps placed at both ends of the plasmonic waveguide, at an incident wavelength of 1550nm, the transmission of the waveguide with metallic gallium is improved to 30.3%, while the extinction ratio is approximate 7.05 dB. Other parameters (e.g., the width of Si_3N_4 core, w_p), can also be optimized to increase the power transmission. From simulation results, with increased core thickness w_p, the transmission of the waveguide will increase as well. For example, when w_p = 90nm, transmission of the waveguide with metallic gallium increases to 39.7% at λ = 1550nm. The whole structure exhibits Fabry–Pérot effect as the length of the plasmonic waveguide changes [163], when the length of the Ga-Si_3N_4-Ga waveguide is 140nm, transmission with metallic gallium is around 40.7%, and the extinction ratio is approximately 4.25 dB.

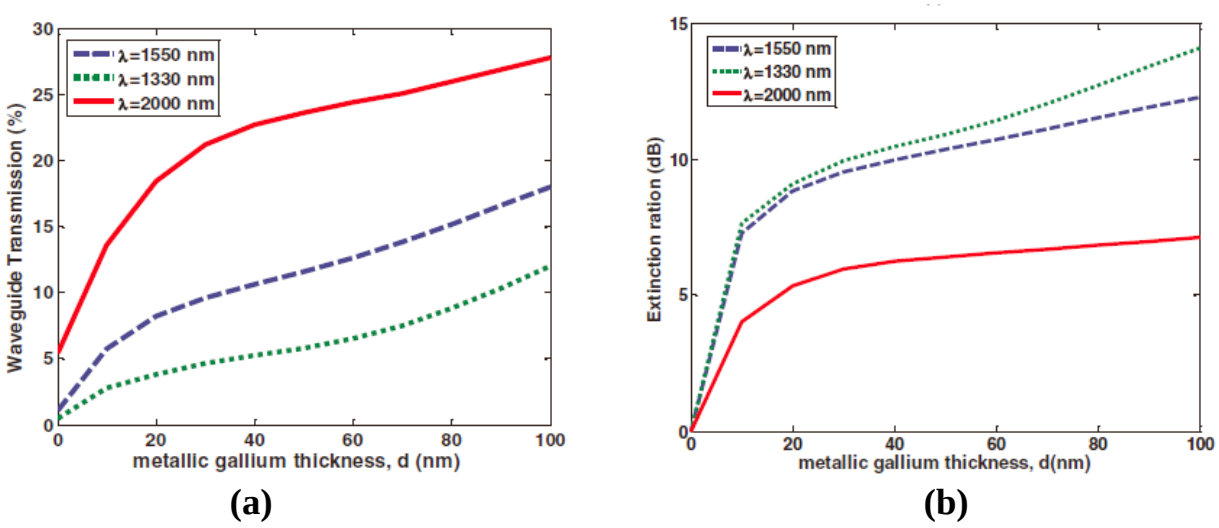

Figure 4.6 (a) Power transmission as a function of the depth *d* of metallic gallium thin film. (b) Extinction ratios of the Ga-Si_3N_4-Ga plasmonic waveguide as a function of *d*. [150]

4.2.2 3D FDTD simulation results

To characterize the optical switch in a 3D configuration and compare the extinction ratios with the 2D switch, the dimensions of the optical switch is similar to those in 2D simulations. The cross section of the Si waveguides in the *y*-*z* plane is assumed to be square, where the height of the Si waveguides h_d equals the width w_d to be 400nm. The height of the plasmonic waveguide h_p is identical as h_d. The length l_p and the width w_p are set as l_p = 400nm and w_p = 60nm, respectively. In the 3D numerical simulations, the gallium is either in the metallic phase or in the α-phase. The same notation of gallium in the α-phase is used, for example, CB represents *c*-axis lying in the light propagation direction, *x*-axis, *b*-axis lying in the *z*-axis, and *a*-axis lying in the *y*-axis. A mode with the main component of *E* in the *y* direction is excited in the input silicon waveguide. The power transmission measured at the output silicon waveguide is as follows: 31.1% for metallic gallium, 1.2% for AB, 2.95% for AC, 4.3% for BA, 7.0% for BC, 1.34% for CA, and 1.0% for CB. The extinction ratio using Eq. (4.1) is calculated as 6.48 dB, which is consistent with that of the 2D switch, 6.33 dB.

4.3 Proposed Fabrication Steps

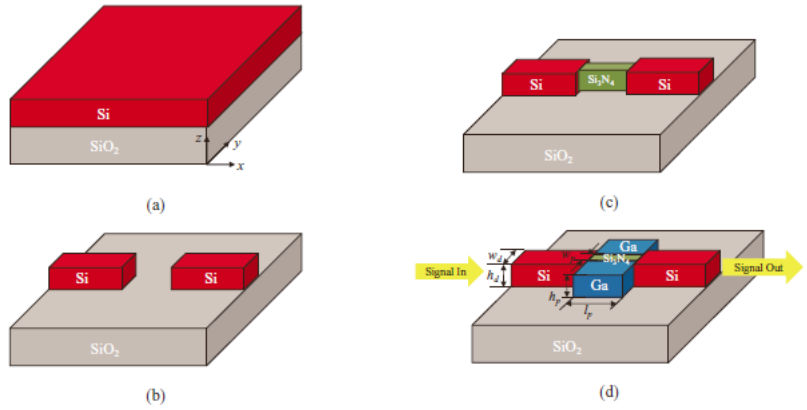

Figure 4.7 (a) Starting the fabrication process on an SOI wafer. (b) Defining the input and output silicon waveguide. (c) Deposition of Si_3N_4 film as the core of the plasmonic waveguide. (d) Deposition of gallium film. [150]

Here, a possible 3D implementation of the optical switch is proposed. Figures 4.7(a) –4.7(d) illustrates the main fabrication steps of the optical switch. First, the input and output silicon waveguides will be fabricated on a silicon-on-insulator (SOI) wafer. In the second step, the dielectric core of the plasmonic waveguide, silicon nitride, will be deposited between the two silicon waveguides by a method named hot-wires chemical vapor deposition [167]. With NH_3/SiH_4 ratios between 40 and 70, and at low substrate temperature of 100 ℃ or 250 ℃, dense films (2.56 to 2.74 g/cm^3) and refractive index between 1.93 and 2.08 can be obtained [167]. The following lithography and etch steps will pattern the dielectric core. Good alignment is required to make the dielectric core be in alignment with the input/output silicon waveguides in the *y*-axis. In the third step, a high quality gallium film will be deposited on the substrate from Ga targets using a *Q*-switched mode-locked Nd:YAG laser (λ=1.064 μm; τFWHM =60 ps) [168]. It has been reported that gallium nanoparticles with a relatively narrow size could be formed on the substrate if it was illuminated by very low intensity laser light [169,170]. The gallium film will re-solidify to α-phase after the melting process [168].

Recently, experimental demonstrations of plasmonic waveguide [171] and coupler [172] have been reported. Different from our proposed structure, the core material of the fabricated waveguides is air. One challenge of the fabrication process for our structure is the conformality of each deposited film. In order to show how the thicknesses of the silicon nitride or the gallium film will impact the extinction ratio, we performed a series of simulations with the conditions that either the silicon nitride or the gallium film was not at the target thickness, which is 400nm. Figure 4.8 shows the extinction ratio as a function of the thickness of silicon nitride or gallium. For simplicity, in each simulation, only one film (silicon nitride or gallium) thickness varies, while the other one has a thickness of 400nm. The range of thickness variation is 400 ± 40nm. From the results, it is seen that gallium film thickness is more critical, since ±10% thickness variation will cause a maximum 15% extinction ratio change, while with the same thickness variation, silicon nitride will only bring an 8.4% change in extinction ratio.

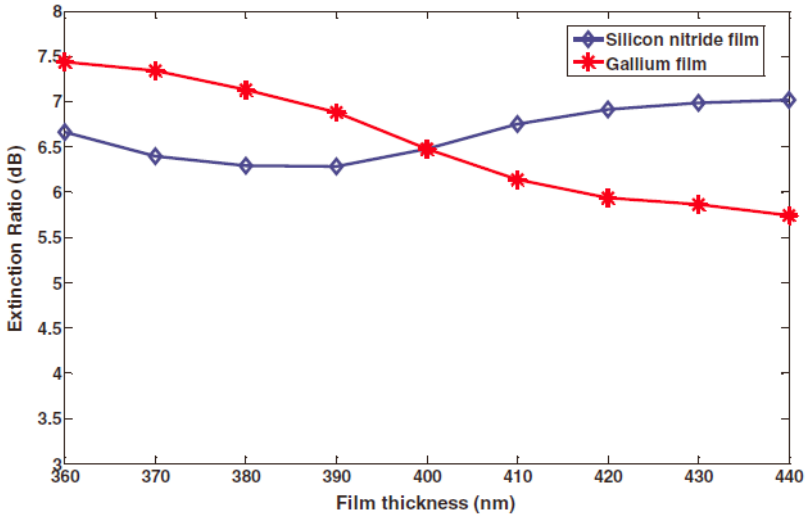

Figure 4.8 Extinction ratio as a function of thickness of silicon nitride or gallium film. [150]

4.4 Conclusions

Recently, all-optic switching has also been reported in metal-insulator-metal waveguides with Kerr nonlinear defects [173,174]. Compared with the plasmonic waveguides proposed in

those papers, the switching mechanism of our Ga-Si_3N_4-Ga waveguide mainly depends on the waveguide material (gallium) property, not by introducing an additional nonlinear medium. Hence, our proposed structure is much simpler and easier to fabricate.

To summarize, in this chapter the potential switching properties of a simple Ga-Si_3N_4-Ga plasmonic waveguide is investigated. With a length of only 400nm, an extinction ratio as 7.68 dB can be achieved in the proposed structure. Since the phase transition of gallium is a surface-mediated effect, we also show that with tens of nanometers thick metallic gallium sandwiched between Si_3N_4 and α-gallium, the power transmission level will increase greatly. Further study on the parameter optimization confirms that the transmission of the waveguide can be improved to 40.7%, while the extinction ratio is still kept over 4.25 dB.

5 ITO-BASED MULTILAYER ELECTRO-OPTICAL MODULATOR

Gallium is not the only naturally existing metamaterial. From Chapter 5 to Chapter 8, we will introduce another two natural metamaterials – ITO and graphene, and explore their applications in ultra-compact modulators.

In this chapter, we investigated an active plasmonic metamaterial – ITO and its application in electro-optical modulators, where the structures are planar multilayer structure. Here we also use a new material named electrolyte gel to enhance the modulation effect. When applying external voltages on these multilayer structures, electric double layers are formed at the interfaces of ITO and electrolyte gel, which can attract more electrons or holes in ITO. Two different structures: ITO/electrolyte gel/doped-Si and ITO/electrolyte gel/ITO, are investigated. Based on attenuated total reflection (ATR) measurement results, modulation depth up to 38.8% can be achieved. Preliminary result is present for the real time response of an ITO/electrolyte gel/doped-Si modulator.

5.1 Introduction

Conventional photonic elements have physical dimensions on the order of the wavelength of light, due to the diffraction limits of light in those devices. Hence, the difference in the physical sizes between the nanometer-scale electronic devices and the micrometer-scale photonic devices leads to the incompatibility between these two types of devices. Surface plasmon polaritons (SPPs) combines the high bandwidth offered by photonics and the nanometer-scale device size offered by nano-electronics by coupling a photon's energy with a free-electron gas, creating a subwavelength,

oscillating mode at the interface of dielectric and metal. Plasmonics and metamaterials are driving the development of novel devices with unprecedented functionalities, such as subwavelength waveguides [175-177], superlenses [4,5,178], optical invisibility cloaks [179-181], and planar magnifying hyperlens and light concentrators [182-184]. Since the plasmon phenomenon in optical and telecommunication frequencies typically originates from the collective oscillations of free charges in a material, plasmonic devices generally require metallic components. The abundant free electrons provide the negative real permittivity, which is an essential property of plasmonic material. One important challenge in these fields is the high loss caused by the metallic components in the devices, especially in the visible and ultra-violet (UV) spectrum regime. The high loss is a major obstacle in the design of efficient devices, seriously limiting the feasibility of many plasmonic applications. In order to compensate the high loss, optical gain materials are combined with metallic structures [185-187]. However, even the best gain materials available are barely enough to compensate the losses in metals. Therefore, alternative plasmonic materials with lower losses are desired to develop robust plasmonic devices and overcome the major bottleneck.

Conventionally, semiconductors are regarded as dielectric materials for frequencies above several hundred THz. However, semiconductors can exhibit a negative real permittivity in this spectrum regime under certain conditions [103,188,189]. Due to the flexibility in tuning the carrier concentration, semiconductors are potential alternative plasmonic materials. Indium-tin-oxide (ITO), a representative of TCOs, has been shown to be a potential plasmonic material in the near-infrared (NIR) region [190-192]. ITO is transparent degenerately doped semiconductor, containing 90%wt indium oxide (In_2O_3) and 10%wt tin oxide (SnO_2), which is widely used as transparent electrodes in solar cells and displays [103,193,194].The exploration of TCOs as the plasmonic metamaterial for near-infrared (NIR) applications can be traced back to decades ago [190,192,195].

Comparative studies can be found in Refs. [25,196]. The carrier concentration in ITO is in the range of 10^{19}~10^{21}/cm^3, which can be controlled by manipulating the concentration of oxygen vacancies and interstitial metal dopants. The high carrier concentration enables guiding surface mode at the interface of ITO and dielectric materials, for example air, which has a great potential in the applications of electro-optic (EO) modulators [24,107].

5.2 Transfer Matrix Method (TMM)

The transfer matrix method [197-199] in optics is a powerful numerical method used to analyze the propagation of the electromagnetic waves through a layered medium. According to Maxwell's equations, there are simple continuity conditions for the electric/magnetic field across boundaries from one medium to the next medium. If the field is known at the beginning of a layer, the field at the end of the layer can be derived from a simple matrix operation. Therefore, a stack consisted of multiple layers can be represented as a system of matrix, which is a product of the individual layer matrices. By converting the system matrix back into reflection and transmission coefficients is the final step of this method.

5.2.1 Single boundary

Considering a wave transmits through a planar boundary between two materials with indexes n_0 and n_1 as illustrated in Fig. 5. 1, we have $n_0 \sin\theta_0 = n_1 \sin\theta_1$ according to Snell's law. The transfer matrix M_{01} can be expressed as

$$M_{01} = \frac{1}{2a_{10}n_1}\begin{bmatrix} n_0 + n_1 & n_1 - n_0 \\ n_1 - n_0 & n_0 + n_1 \end{bmatrix}, \tag{5.1}$$

where $n_0 = n_0 \cos\theta_0$, $n_1 = n_1 \cos\theta_1$, $a_{10} = 1$ for TE mode, and $n_0 = n_0 \sec\theta_0$, $n_1 = n_1 \sec\theta_1$, $a_{10} = \cos\theta_1 / \cos\theta_0$ for TM mode.

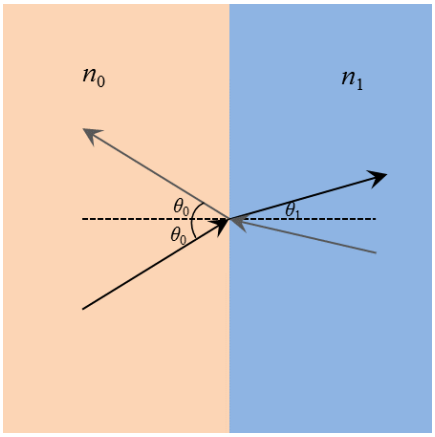

Figure 5.1 Oblique incidence.

5.2.2 Propagation in a multilayer stack

Figure 5.2 shows an incoming light beam transmitted through a planar multiple layer stack from medium 1 to medium (*i*-1), where media 0 and *i* are the input and output media, respectively.

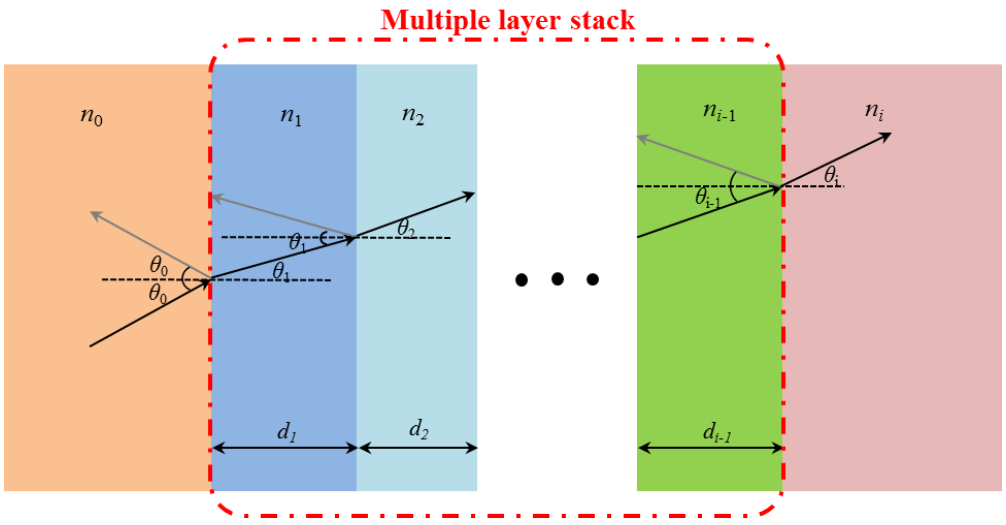

Figure 5.2 Illustration of a planar multilayer stack, incoming light comes from medium 0 and leaves the stack from medium (i-1).

As the light beam transmits from medium 0 to medium 1 with an oblique angle, at the boundary, the transmission matrix M_{01} can be expressed as Eq. (5.1). When the light transmits through medium 1 to medium 2 and propagates in medium 2, the transmission matrix will be added one propagation term $e^{-j\varphi}$ and expressed as

$$M_{12} = \frac{1}{2n_2 a_{21}} \begin{bmatrix} (n_2 + n_1)e^{-j\widetilde{\varphi}_1} & (n_2 - n_1)e^{j\widetilde{\varphi}_1} \\ (n_2 + n_1)e^{-j\widetilde{\varphi}_1} & (n_2 - n_1)e^{j\widetilde{\varphi}_1} \end{bmatrix}, \tag{5.2}$$

where $\widetilde{\varphi}_1 = n_1 k_0 d_1 \cos\theta_1$, k_0 denotes the vacuum wave vector [200]. If medium 1 is a lossless material, the propagation only induce phase change without amplitude change. If the medium has a complex index, for example metal, both amplitude and phase will change.

The transmission matrix through the whole stack is the product of all the individual matrices in sequence

$$M = M_{i\,i-1} * M_{i-1\,i-2} * \cdots M_{21} * M_{10} = \begin{bmatrix} A & B \\ C & D \end{bmatrix}. \tag{5.3}$$

The transmission matrix *M* can also be expressed in a concise way as an *ABCD* matrix, as shown in Eq. (5.3). The reflectance from the whole system can be calculated as

$$R = \left|\frac{C}{D}\right|^2. \tag{5.4}$$

In this chapter, we characterized the modulation properties of the ITO-based multilayer modulators by measuring the reflected power on an ATR setup. The experimental results will be modeled with transfer matrix method (TMM).

5.3 Drude model

The Drude model explaining the transport properties of free electrons in materials, was proposed in 1900 [201,202]. There are two main solid state systems that exhibit strong free electron effects: metals and doped semiconductor. Both can be treated as plasmas, which is a neutral gas of heavy ions and light electrons. Considering the oscillations of a free electron induced by the AC electric field *E*(t) of an electromagnetic wave, the equation of motion for the displacement *x* of the electron is

$$m_0 \frac{d^2x}{dt^2} + m_0\gamma \frac{dx}{dt} = -eE(t) = -eE_0 e^{-i\omega t} \tag{5.5}$$

where ω is the frequency of the light, and E_0 is its amplitude. The acceleration of the electron is represented by the first term, while the second is the frictional damping force of the material. The term on the right hand side is the driving force exerted by the light.

By substituting $x = x_0 e^{-i\omega t}$ into Eq. (5.5), we can obtain $x(t) = \frac{eE(t)}{m_0(\omega^2 + i\gamma\omega)}$. The polarization P of the gas is equal to $-Nex$, where N is the number of electron per unit volume. Recalling the electric displacement field D, which is defined as $D = \varepsilon_r \varepsilon_0 E = \varepsilon_0 E + P$. Therefore, D can be written as

$$D = \varepsilon_0 E - \frac{Ne^2 E}{m_0(\omega^2 + i\gamma\omega)}. \tag{5.6}$$

Hence, we can get

$$\varepsilon_r(\omega) = 1 - \frac{Ne^2}{\varepsilon_0 m_0} \frac{1}{(\omega^2 + i\gamma\omega)}. \tag{5.7}$$

This equation can be written in a more concise form as

$$\varepsilon_r(\omega) = 1 - \frac{\omega_p^2}{(\omega^2 + i\gamma\omega)}. \tag{5.8}$$

where

$$\omega_p = \left(\frac{Ne^2}{\varepsilon_0 m_0}\right)^{\frac{1}{2}} \tag{5.9}$$

is known as the plasma frequency, while e is the unit electric charge, ε_0 the free space permittivity, and m_0 the electron mass. The plasma frequency ω_p corresponds to the natural resonant frequency of the free carrier gas.

The free electron model presented above can be applied to doped semiconductors if two appropriate modifications [203]. Firstly, the fact that the electrons and holes are moving in the conduction or valence band of a semiconductor needs to be considered. In this scenario, we can assume that those carriers behave as particles with an effective mass m^* rather than the free electron mass m_0. Secondly, there are other mechanisms that may contribute to the dielectric constant as well as the free carrier effects. The main extra part is the contribution to the polarization due to the optical response of the bound electrons. Therefore, Eq. (5.6) can be rewritten in the following form when the two modifications are considered

$$D = \varepsilon_\infty \varepsilon_0 E - \frac{Ne^2 E}{m^*(\omega^2 + i\gamma\omega)} \tag{5.10}$$

The effective mass m^* accounts for the band structure of the semiconductor, ε_∞ is the high frequency dielectric constant, and carrier density N in this equation is the density of free electrons or holes generated by the doping process. From Eq. (5.10) we can write the frequency dependence of the dielectric constant as

$$\varepsilon_r(\omega) = \varepsilon_\infty - \frac{\omega_p^2}{(\omega^2 + i\gamma\omega)} \tag{5.11}$$

where $\omega_p^2 = \frac{Ne^2}{m^*\varepsilon_0}$ is the plasma frequency. Since the carrier density is much smaller than that in metals, the plasma frequency may occur in the infrared spectral range.

In this chapter, we will use Eq. (5.11) to model the optical properties of ITO, where the ITO is treated as doped-semiconductor.

5.4 Optical property of ITO

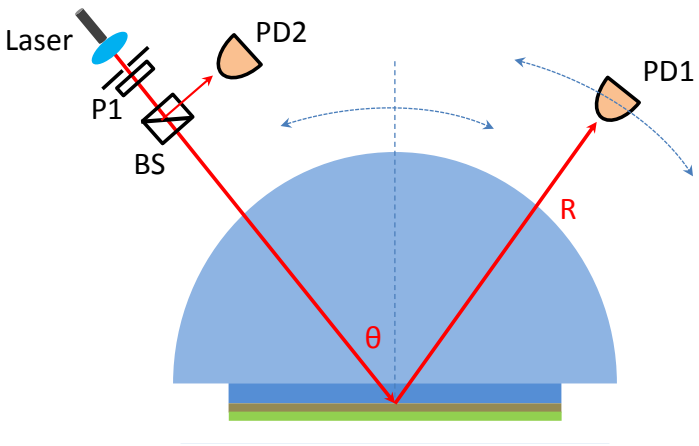

Figure 5.3 ATR setup in Kretschmann configuration.

An attenuated total reflection (ATR) setup was built in the Kretschmann configuration [204], as illustrated in Fig. 5.3. A collimated laser beam propagates through a broadband polarizer (P1), and the output is either *s*- or *p*- polarized light, and is then split into two by a beam splitter (BS). One beam is used for collecting source power fluctuation and fed into a Ge photodiode (PD2); another is incident at the angle θ into a BK7 glass hemi-cylindrical (Ø100mm obtained from Rocoptonics) lens, which functions as a coupling prism in this setup. The reflected light is then collected by another Ge photodiode (PD1). The reflectance, *R*, is well measured by the power ratio between PD1 and PD2, even there is power fluctuation in the laser source. The rotation of the prism (together with the multilayer ITO modulator) and PD1 is in a θ-2θ configuration, which is precisely controlled by two motorized rotation stages. The increment of θ is set as 0.25^{o}. The measurement result is recorded by a LabView program, thus, the reflectance *R* as a function of θ can be plotted.

The measured reflectance of the ITO on corning glass slide is numerically fitted by calculating the reflectance through the multilayer structure based on the transfer matrix method (TMM) [197-199]. In order to avoid the thin air gap between the sample and the BK7 prism, a

BK7 index matching liquid was used. The film stack in this experiment can be treated as BK7/ITO/air. In the fitting, the thickness of the ITO film and its permittivity (both real and imaginary parts) were used as the variables to model the measured reflectance data. After the 4 hours-annealing process, the sheet resistance of the ITO film is 63.16Ω/□. The fitted results are shown in Fig. 5.4(a), where the magnitude of the permittivity is also plotted. Here a cross-over wavelength is defined as, at this specific wavelength, the magnitude of the permittivity $|\varepsilon|$ is very small and even close to zero. In Fig. 5.4(a), a cross-over wavelength of 980nm is observed, where the permittivity of ITO is $\varepsilon = 0.46 + j0.13$ and $|\varepsilon|$=0.478. Two measured reflectance curves as a function of angle are shown in Fig. 5.4(b), the blue curve is at λ=980nm where ε is close-to-zero and the red one is at λ=1260nm where ε is far-from-zero. As mentioned previously in Section 1.3.3, deposition/annealing conditions play a crucial role in achieving the desired optical property of ITO. For example, Ref. [196] demonstrates that ITO could have a cross-over wavelength in the near infrared (NIR) regime.

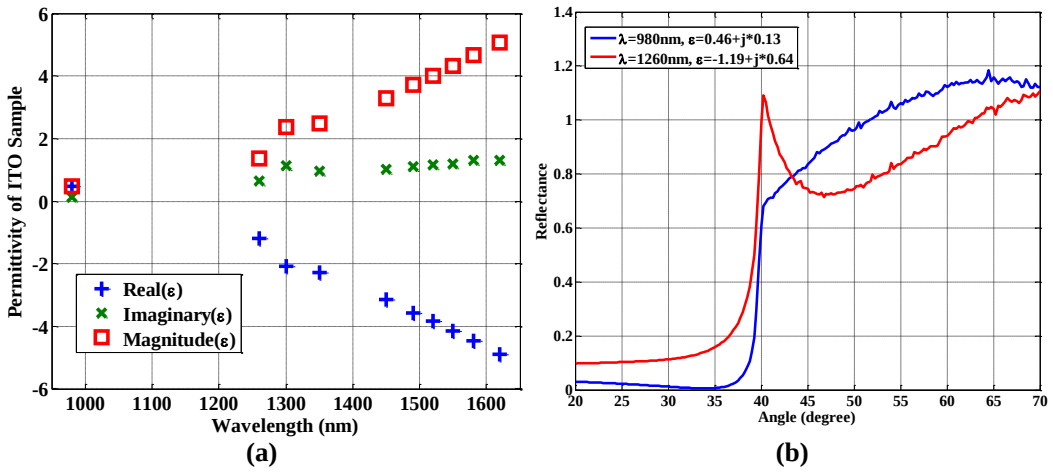

Figure 5.4 (a) Fitted permittivity of an ITO on glass sample. (b) Measured reflectance curves.

The permittivity of ITO can be described by Drude model [201,202], which is described in Eq. (5.11) $\varepsilon(\omega) = \varepsilon_\infty - \frac{\omega_p^2}{\omega(\omega + j\gamma)}$, where ε_∞ is the high frequency dielectric constant, ω_p is the plasma

frequency, and γ is the electron damping factor. Hence, the carrier concentration in ITO can be determined by

$$N = \frac{\omega_p^2 \varepsilon_0 m^*}{e^2}, \tag{5.12}$$

where ω_p is the plasma frequency, and m^* is the effective mass of electron. Assuming $\varepsilon_\infty = 4$ [196], the carrier concentration is estimated as N=4.12E+21/cm^3 at wavelength of 980nm.

5.5 ITO-based multilayer modulators

5.5.1 Fabrication of multilayer structure

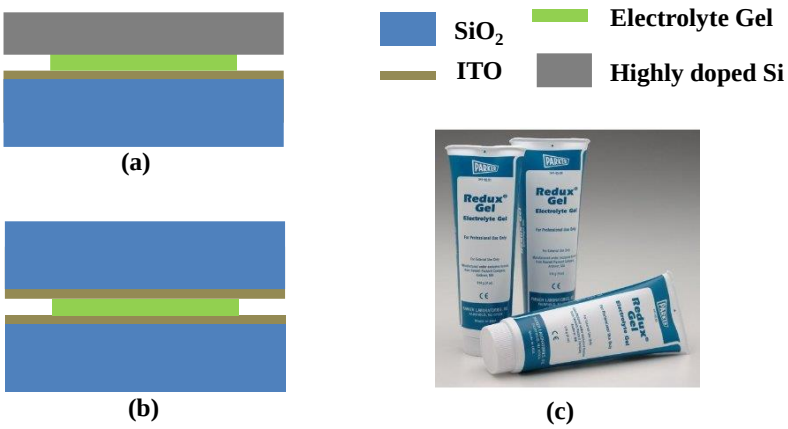

Figure 5.5 Illustration of ITO-based multilayer modulator: (a) ITO/gel/doped-Si, and (b) ITO/gel/ITO. (c) Commercial Electrolyte gel.

Figure 5.5(a) and (b) illustrate two different types of ITO-based multilayer modulators, which are similar as that of metal-oxide-semiconductor (MOS). Here, an electrolyte gel is used to replace the sandwiched oxide material and form simple planar multilayer structure. Electrolyte has been used as gate insulators in organic field-effect transistors in 2005 by Nilsson *et. al.* [206]. The interface between a metal (or heavily-doped semiconductor) and electrolyte is of interest in most electrolyte applications, where two parallel layers of positive and negative charges called an electric double layer (EDL) are formed. Another advantage of using electrolyte as the gating

material is, the device behavior can be conveniently controlled by varying the concentration of chemical compounds in the electrolyte [207,208]. In our experiments, a commercially available electrolyte Redux® Gel is used to fabricate the ITO-based multilayer modulators. Sodium chloride (NaCl) is the main chemical compound in the electrolyte gel that makes it highly conductive. The fabrication of the modulators starts from ITO film deposition on a transparent glass slide, as described in Section 5.4. After applying a thin layer of electrolyte gel on the surface of ITO film, either a heavily doped (resistivity as low as 0.001-0.002Ω·cm) silicon chip or another identical ITO sample with the ITO side facing the electrolyte gel is tightly pushed toward the substrate ITO to form the multilayer modulator, as shown in Fig. 5.5(a) and (b), respectively. With this fabrication method, the thickness of the sandwiched electrolyte gel is usually 4-6μm, which is determined by the numerical fitting.

5.5.2 Experimental demonstration of modulation effect

An ATR setup as illustrated in Fig. 5.3 was used to test the modulation performance of the two types of ITO-based modulators. During the experiment, the ITO-based modulators were mounted on the back of the hemi-cylindrical BK7 prism. To avoid a thin air gap between the prism and the modulator, a BK7 index matching liquid is applied between them. In all the experiments, the reflectance of the modulators was measured in a sequence of: (1) without externally applied voltage, (2) with an externally applied voltage V_P, and (3) with an externally applied voltage which has reversed polarity but the same magnitude. We firstly focused on a simple structure, as shown in Fig. 5.6(a), which includes only one active ITO layer. The measured reflectance of the modulator with different applied voltages, as a function of θ with a *p*-polarized incident light beam at λ = 1520nm is shown in Fig. 5.6. With an applied voltage, an EDL is formed at the interface of the electrolyte gel and the ITO. Here we assumed there is a 5nm-thick [24] depletion layer (with

positive voltage V_P = 10 V, illustrated in Fig. 5.6), or a 5nm-thick accumulation layer (with negative voltage -V_P=-10V) formed in ITO at the interface. The modulation depth, $M(\theta)$, as a function of angle θ at a given wavelength can be defined as:

$$M(\theta) = \frac{|R_{V_P} - R_{-V_P}|}{R_0}, \tag{5.13}$$

where R_0 is the experimentally measured reflectance without applied voltage, $|R_{V_P}$-$R_{-V_P}|$ is the magnitude of the difference of the two reflectance with applied voltages. From Fig. 5.5, the modulation depth at a specific angle of θ=70 °can be calculated as M(70 °)=20.7%. We attribute the modulation to the change of the free carrier concentration in either the 5nm-thick depletion layer or the accumulation layer in ITO at the interface, which is assisted by the redistribution of the ions in electrolyte gel induced by the applied voltage. The charge distribution at the interface and electric potential (V) at a stable status with the applied voltage is schematic illustrated in Fig. 5.6.

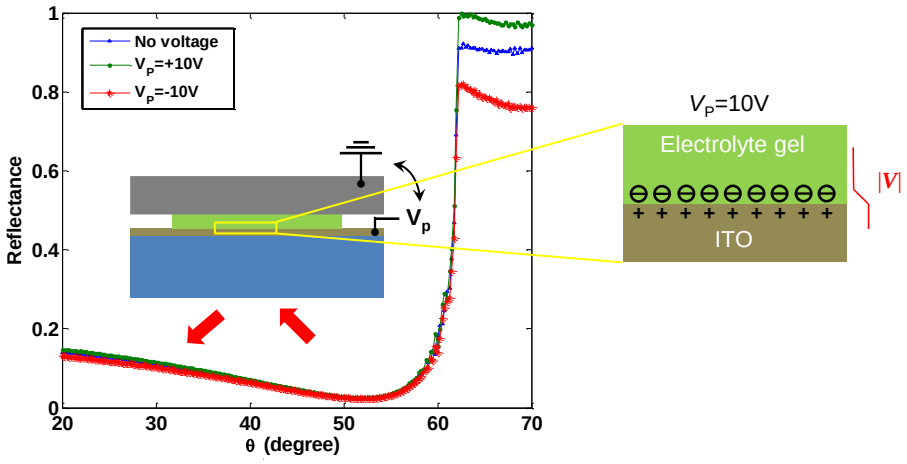

Figure 5.6 Normalized reflectance as a function of angle for the ITO/electrolyte gel/heavily-doped Si modulator with different applied voltages. Inset: illustration of the modulator with applied voltage.

The measured reflectance of the ITO modulator is numerically fitted by calculating the reflectance through the multilayer structure based on the transfer matrix method (TMM) [197-199]. In this experiment, the film stack can be treated as BK7/ITO/electrolyte gel/heavily-doped Si. In order to simplify the fitting, we used the permittivity of the 5nm depletion layer or accumulation layer in ITO (both real and imaginary parts), and the thickness of the electrolyte gel as the variables to model the measured reflectance data. The permittivity of the electrolyte gel is determined by a separate ATR measurement, which is $\varepsilon_{gel} \approx 1.80$ at λ = 1520nm. In the numerical fitting, the BK7 medium has a refractive index of n = 1.50 at λ = 1520nm. The result turns out that the dielectric constant of ITO film $\varepsilon_{ITO} = 3.7+j1.0$ at λ = 1520nm without applied voltage, and the thickness of the electrolyte gel $t_{gel} \approx 5.22\mu$m. Note the fitted dielectric constant of ITO at the wavelength of 1520nm is significantly different with the one shown in Fig. 5.4(a), due to the ITO film was not annealed after deposition.

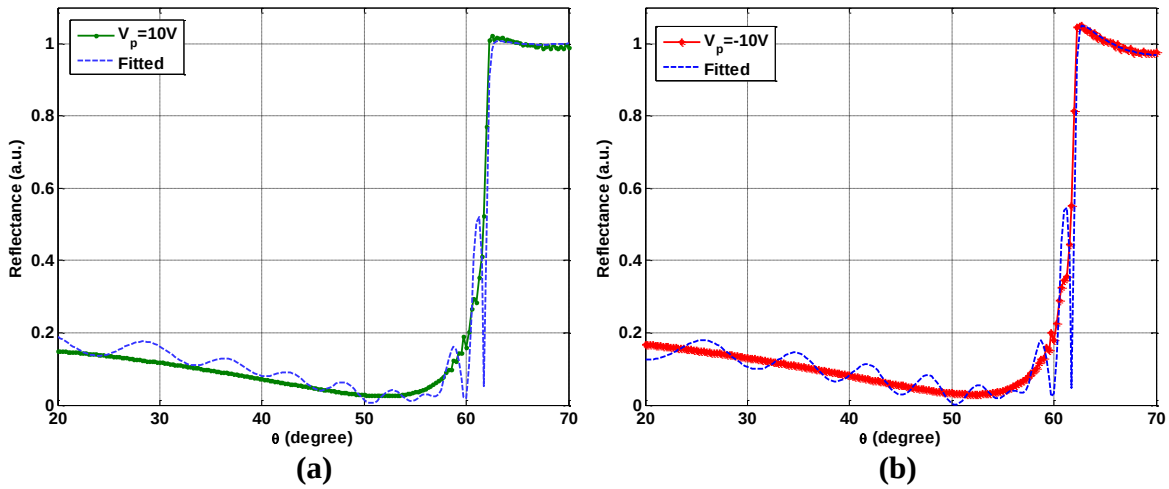

Figure 5.7 ATR measurement results and fitted curves for (a): with V_P= +10V, (b): V_P= -10V.

With an applied voltage of V_P = 10 V, the permittivity of the 5nm depletion layer of ITO is fitted as $\varepsilon_{ITO\text{-}dep} = 3.69+j0.6$. When the polarity is reversed, the permittivity of the 5nm

accumulation layer of ITO is $\varepsilon_{ITO\text{-}acc}$ = -1.59+*j*8.1. Combining Eq. (5.11) and (5.12), the carrier concentration in ITO can be estimated as: $N(0V)=9.82\times10^{20}/cm^3$, $N(10V)=6.18\times10^{20}/cm^3$ for the 5nm depletion layer, and $N(-10V)=8.13\times10^{21}/cm^3$ for the 5nm accumulation layer, assuming ε_∞=4.55 for all the conditions [24]. The fitted curves are shown in Fig. 5.6 as the blue dashed lines for the applied voltage measurements.

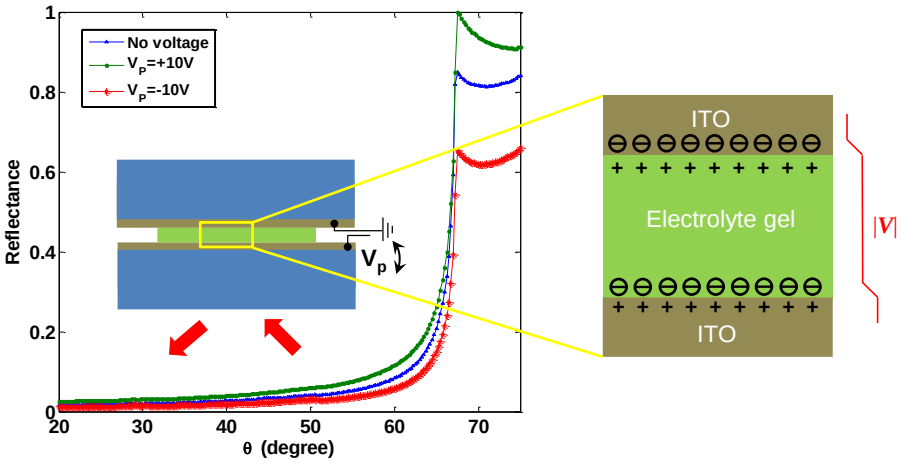

Figure 5.8 Normalized reflectance as a function of angle for the ITO/electrolyte gel/ITO modulator with different applied voltages. Inset: illustration of the modulator with applied voltage.

The modulation depth can be further enhanced when the electrolyte gel sandwiched between two identical ITO samples. To make the measurement result accurate, we used a glass deflector on the other side of the modulator [205], to avoid any light reflected back and collected by the detector PD1. When applying a voltage to the double-ITO modulator, there will be an EDL formed at each electrolyte gel/ITO interface, as shown in Fig. 5.8. The double EDLs result a higher modulation depth, which is $M(70°)$=38.8%, at a specific angle of θ = 70 °with *s*-polarized light at λ = 1520nm. This result also reveals that the ITO-based multilayer modulator is not sensitive to the polarization of the incident light beam.

5.5.3 Preliminary result for real-time response

The switching speed of the modulator is directly influenced by the relaxation of the ions in the electrolyte gel. For the modulator structure shown in Fig. 5.5(a), another experiment is carried out to test this relaxation effect, where two rectangular voltage pulses are excited by a DC power supply. The first pulse is 30s wide with a height of +20V applied on ITO, after 120s the second pulse is excited with the same width but an opposite polarity, as illustrated by the blue curve in Fig. 5.9. The incident light beam is at λ = 1310nm with *p*-polarization. The response of the ITO-based modulator to the applied voltage pulses as a function of time is measured at a specific angle θ = 65 ^{o}and the reflectance is shown in Fig. 5.9. When there is no applied voltage, the reflectance *R* is at its baseline level. When the voltage pulses are applied on the ITO (at time t_1 and t_2), EDLs are immediately formed at the interface of the electrolyte gel/ITO. The induced change of the reflectance is similar as we observed in the first experiment shown in Fig. 5.6, and the modulation depth is around 12.4%. When both the rectangular pulses vanished, the reflectance of the modulator either decreases or increases toward its baseline level, respectively. However, it is clearly seen that for both the situations, the modulator needs a long time to recover to its baseline level. With the positive voltage pulse, the recovery time is even longer. The phenomenon could be caused by the different mobility of the major carriers in the 5nm region in ITO at the interface. The response of the ITO modulator under high-frequency AC signals needs further investigation. Both the ions in electrolyte gel and the free carriers in ITO needed to form the electric double layer will probably limit its applications at high frequency.

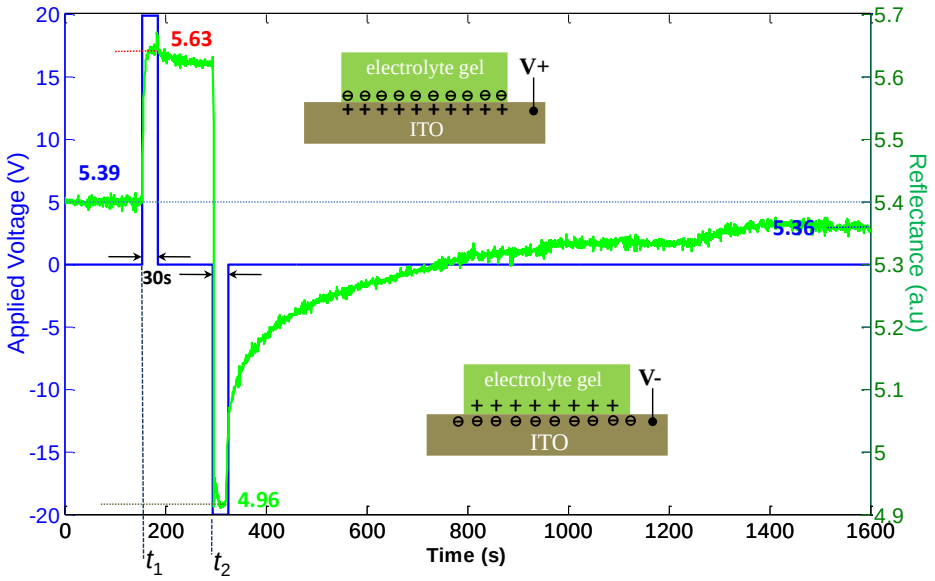

Figure 5.9 Ionic relaxation effect of the electrolyte gel, at an angle of θ = 65 °.

5.6 Conclusions

To summarize, we have experimentally demonstrated modulation effect with multilayer modulators based on ITO. The fabrication of the modulators are much simpler compared to other work [24], which contains only one fabrication process (ITO deposition). The modulation depth is around 21.7% with one ITO active layer, and this result can be further enhanced to 38.8%, where there are two ITO active layers. The real time response of the ITO-based modulators needs further investigation, where the response is determined by the relaxation of the ions in electrolyte gel as well as the free carriers in ITO.

6 ULTRACOMPACT ELECTRO-OPTIC MODULATORS BASED ON ENZ-SLOT WAVEGUIDE

In this chapter, we will continue the work in Chapter 5 and propose a novel waveguide, namely "TCO-slot waveguide", which combines both the tunable property of a TCO and field enhancement of a slot waveguide. Recent experiments showed that unity-order index change [24] in a TCO can be achieved in a metal-oxide-semiconductor (MOS) structure by accumulation charge. However, the ultrathin (~5nm) accumulation layer and inherent absorption of TCOs impede the practical applications of this effect. We found that light absorption can be sharply enhanced when the slot dielectric constant is tuned close to zero. Based on TCO-slot waveguides, efficient electro-absorption modulation can be achieved within 200nm with small insertion loss.

6.1 Introduction

Ultracompact high-speed electro-optic (EO) modulators have become one of the critical technical bottlenecks impeding the wide applications of on-chip optical interconnects. This is due to the very poor EO properties of conventional materials. Phase modulators are on the order of millimeters [209-211] and can reduce to about tens of micrometers by introducing novel structures to enhance the EO effect [212]. Absorption modulators can be quite compact, but in most cases they require advanced materials [82,213]. Even though, their dimensions are still 10μm~100μm. On-chip optical interconnects require EO modulation at the nanoscale. The key to achieve nanoscale EO modulation is to (1) identify an efficient and low cost active material and (2) greatly enhance light-active medium interaction based on a novel waveguide or platform.

The development of metamaterials has opened new horizons in photonics [11,214]. Recent research shows that the dielectric constant of materials can be engineered to be almost arbitrary value (positive, zero, or negative). One example is epsilon-near-zero (ENZ) materials [215-217], which received significant attention and found applications in squeezing electromagnetic energy through very narrow channels [218,219], design of matched zero-index materials [217,220], as well as shaping the radiation pattern of a source [214,221]. In our recent research [222], we found that light absorption can be greatly enhanced in ENZ-slot waveguides hence ENZ material is very promising to improve the performance of EO modulators. An ENZ material is found to have many advantages as an EO material: (1) sharply enhanced absorption can be achieved in an ultrathin slot; (2) the ultrathin slot does not introduce a large insertion loss; (3) an ENZ material often has tunable optical properties because a small change in carrier density may result in a significant change in dielectric constant.

As introduced in Chapter 5, the effect of free carriers on an optical material can be approximated by the Drude model [201,202], $\varepsilon = \varepsilon_\infty - \frac{\omega_p^2}{\omega(\omega+j\gamma)}$. Here, ε_∞ is the high frequency dielectric constant, γ is the electron damping factor, ω is the angular frequency of the light, and ω_p is the plasma frequency given by $\omega_p^2 = \frac{Ne^2}{\varepsilon_0 m^*}$, which depends on carrier concentration N, and the effective electron mass m^*. The ENZ effect can be found in many materials at $\omega \approx \frac{\omega_p}{\sqrt{\varepsilon_\infty}}$, for example, tungsten at λ_0=48.4nm with a minimum $|\varepsilon(W)|$=0.483, and aluminum at λ_0=83nm with a minimum $|\varepsilon(Al)|$=0.035 [39]. However, the plasma frequencies of most metals are located in the UV regime due to their ultrahigh electron density. To make ENZ located in the near infrared (NIR) regime, the electron density should reduce to 10^{20}~10^{21}/cm^3, which coincides that of TCOs. Recently, considerable effort has been focused on TCOs as the plasmonic and ENZ metamaterial

for NIR applications [107,190,192,195,223]. Feigenbaum *et al*. [24] have studied the refractive index changes in the accumulation layer of a metal-oxide-ITO heterostructure, and experimentally showed that carrier concentration at the oxide/ITO interface can increase from 1E+21/cm^3 to 1E+22/cm^3 under a few volts across a 100nm thick oxide. In particular, the crossover wavelength, where the real permittivity crosses zero, of ITO shifts from 1918nm to 1136nm with only 1.0 V.

6.2 Tunable ENZ-slot waveguides

6.2.1 Epsilon-near-zero (ENZ) state

Based on Feigenbaum et al. work [24], we paid special attention to the two conditions of ITO listed in the bale below:

V_a(V)	ε_∞	ω_p(rad/s)	γ(rad/s)	N(cm^{-3})
0	4.55	2.0968E+15	7.25E+14	1.00E+21
1	4.37	3.4687E+15	5.29E+13	1.65E+22

Table 6.1 Free carrier concentrations in ITO.

The two conditions in Table 6.1 are referred by their corresponding carrier concentrations N=N_1=1.0E+21/cm^3 and N=N_2=1.65E+22/cm^3, which are directly related to the dielectric constant of ITO. Based on the Drude model and the measured parameters, Fig. 6.1(a) plots the dielectric constant of ITO accumulation layer (real part and imaginary part) as a function of wavelength under N=N_1 and N=N_2, respectively. In particular, at λ_0=1136nm,

N=N_1	ε_1=3.2074+j0.5867	ε-far-from-zero state
N=N_2	ε_2=-0.0014+j0.1395	ε-near-zero state

Note that the magnitude of the dielectric constant has changed $|\varepsilon_1|/|\varepsilon_2|$=23.4 times by only 1.0 V gate voltage across the 100nm oxide. In this sense, ITO and other TCOs may be excellent EO materials. Indeed, TCOs have been proposed as the active media in several plasmonic

modulators [224,225]. However, there seems always a tradeoff between the dimensions and insertion loss of the modulators. In this work, we show that modulators with ultracompact dimensions and small insertion loss can be achieved even on a plasmonic platform based on our recent work on ENZ-slot dielectric waveguides [222].

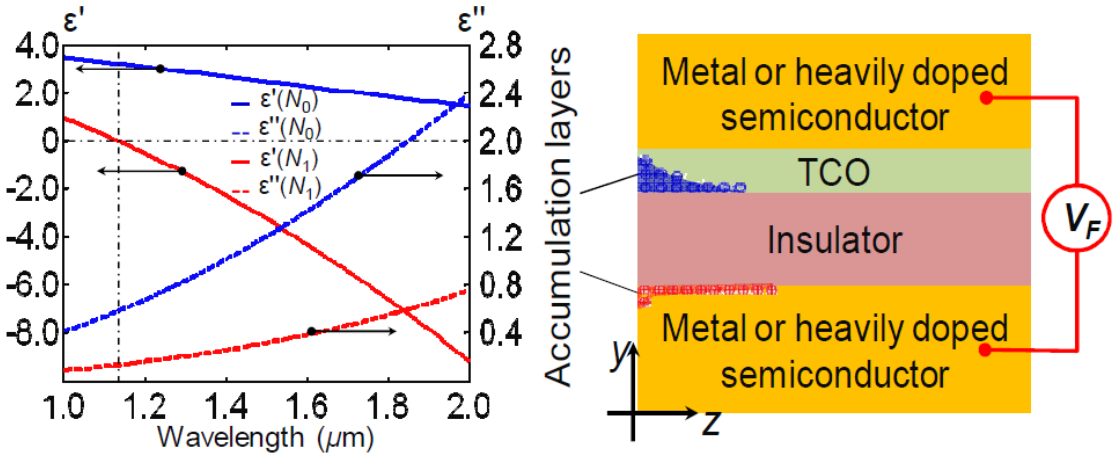

(a) **(b)**

Figure 6.1 (a) Real part and imaginary part of the dielectric constant of ITO as a function of wavelength at two different carrier concentration based on Drude model. (b) The illustration of ENZ-slot waveguides.

A low carrier concentration (or a voltage between 0 and 1.0 V in Ref. [24]) should result in ENZ accumulation layer at the telecom wavelengths. However, due to the lack of the experimental data, we only consider devices working at 1136nm. To circumvent the band edge absorption of Si at 1136nm in the theoretical and numerical study, the waveguide semiconductor is assumed to be a material with a similar refractive index of Si at telecom wavelengths, e.g. GaAs. The applications of the devices described below can be easily extended into telecom Si photonics.

6.2.2 Significantly enhanced absorption by ENZ state

Figure 6.1(b) illustrates the structure to be discussed in this chapter. We will use ITO as one example of various TCOs. Assume 10nm thick ITO film is sandwiched between two Au slabs with 30nm thick SiO_2 buffer layer. The structure is simply the MOS structure as reported in Ref.

[24] with a thinner oxide layer. Optically, it is also known as a metal-insulator-metal (MIM) plasmonic waveguide, where a well confined transverse magnetic (TM) plasmonic mode can be excited between the two Au slabs. The magnetic field is parallel to the slabs, i.e. $H=H_x$ in Fig. 6.1(b). At the SiO_2-ITO interface, the continuity of normal electric flux density,

$$\varepsilon_{ITO}(E_{ITO})_y = \varepsilon_{SiO_2}\left(E_{SiO_2}\right)_y \tag{6.1}$$

is applicable, where the free charge effect is included in the complex dielectric constant. Thus, very high electric field can be excited when $|\varepsilon_{ITO}| \rightarrow 0$. In other words, an ENZ-slot can sharply enhance the electric field in the slot. Without loss of generality, we assume the dielectric constant of the ENZ-slot to be:

$$\varepsilon = \varepsilon' + j\varepsilon'' = \varepsilon' + \frac{j\sigma}{\omega\varepsilon_0}. \tag{6.2}$$

The dissipation power density:

$$p_d = \frac{1}{2}\sigma E^2 \propto \frac{1}{2}\varepsilon'' E^2 \propto \frac{1}{2}\varepsilon''/|\varepsilon|^2 \tag{6.3}$$

can be greatly enhanced at ENZ because: (1) $|E_y|$ reaches its maximum and (2) $\varepsilon''/|\varepsilon|$ nearly grows to its maximum at the same time. To maximize the absorption, the magnitude of dielectric constant of the slot should decrease to zero as close as possible. Equation (6.3) is valid for infinitesimal slot thickness. Otherwise, the guided power will redistribute, and the operation of the slot waveguide fails if the slot thickness is too large. The absorption of the ENZ-slot may even be much stronger than that of Au in the waveguide as can be seen in the following context.

Based on the transfer matrix method, we solved the TM mode supported by the Au-ITO-SiO_2-Au stack, i.e. a 2D ITO-slot MIM plasmonic waveguide. The dielectric constant of Au is ε=

-63.85+j5.07 at λ_0 = 1136nm. We considered two cases: (1) without a gate voltage, $N = N_1$ and the 10nm ITO layer has dielectric constant ε_1 = 3.2074+j0.5867; (2) with a suitable gate voltage, $N = N_2$ and the 10nm ITO layer is split into two, namely 5nm unaffected layer with ε_1 = 3.2074+j0.5867 and 5nm accumulation layer with ε_2 = -0.0014+j0.1395. As shown in Fig. 6.2(b), the electric field can be greatly enhanced in the accumulation layer at λ_0=1136nm when carrier concentration increases from N_1 to N_2. In particular, the magnitude of E_y increases about 9.2 times. In addition, similar level of enhancement can be achieved when the ENZ-slot is sandwiched in a dielectric waveguide. Figure 6.2(b) shows the mode profiles of an ENZ-slot dielectric waveguide at N_1 and N_2. The top and bottom dielectric layers, each 125nm thick, are assumed to be heavily doped semiconductor with refractive index 3.45.

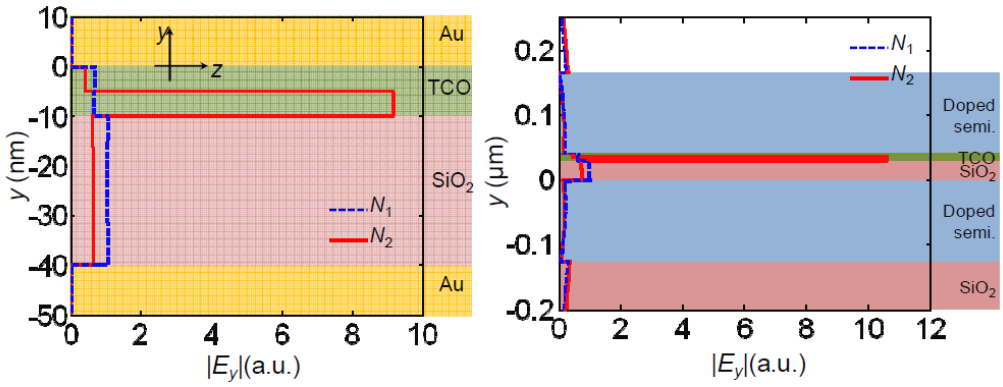

(a) **(b)**

Figure 6.2 (a) The plots of the transverse electric field magnitude across the ENZ-slot MIM plasmonic waveguide at N=N_1 and N=N_2, respectively. (b) The plots of the transverse electric field magnitude across the ENZ-slot dielectric waveguide at N=N_1 and N=N_2, respectively.

6.3 Nanoscale EO modulators

6.3.1 Mode profiles

These 2D film stacks can be easily rendered into 3D rib waveguide as shown in Fig. 6.3. We used a 3D mode solver to study their modes based on the finite-difference time domain (FDTD)

method. Figure 6.3(a) shows the mode profiles of the ITO-slot plasmonic waveguide at different carrier concentrations. Note the top Au strip is only 200nm wide. As can be seen, there is a considerable shift in the effective index: 1.99 at $N=N_1$, and 1.09 at $N=N_2$. Thus, quite compact phase modulators may be realized. More importantly, there is a huge change in the waveguide attenuation. At $N=N_1$, the $|E_y|$ in the ITO is even lower than in the SiO_2 buffer layers, and the waveguide works at the low loss state with $\alpha_1 = 2.92$ dB/μm; at $N=N_2$, the $|E_y|$ in the accumulation layer is many times higher than in the SiO_2 buffer layers, and the waveguide works at the high absorption state with α_2=23.56 dB/μm. As a result, modulation depth 20.64 dB/μm can be achieved, and 3 dB modulation depth only requires 146nm propagation distance. Based on the film stack shown in Fig. 6.2(b), a dielectric modulator can be designed. Figure 6.3(b) shows the mode profiles of the ITO-slot dielectric modulator at different carrier concentrations. A similar modulation effect can be achieved. The dielectric modulator may find more practical applications.

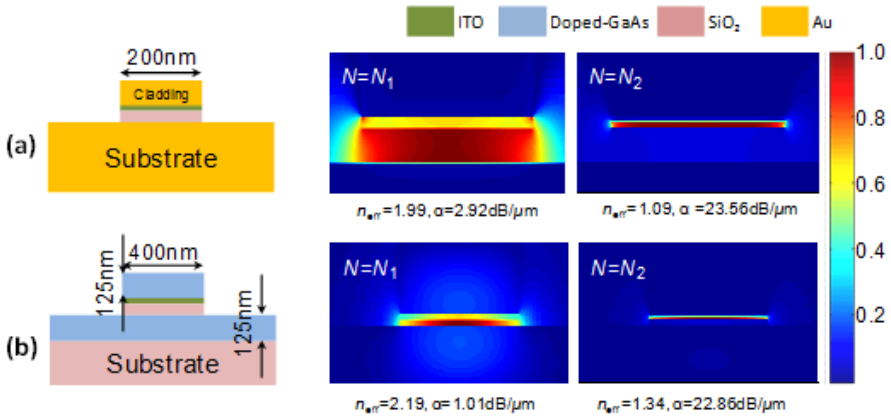

Figure 6.3 The electric field profiles, effective indices, and propagation loss for different ITO-slot waveguides at $N=N_1$ and $N=N_2$, respectively: (a) in a plasmonic waveguide; (b) in dielectric rib waveguide. The refractive indices of the semiconductor and SiO_2 are assumed to be 3.45 and 1.45, respectively. All mode profiles are shown in normalized electric fields.

6.3.2 Performance Analysis

To evaluate the insertion loss of the EO modulators, we performed 3D FDTD simulations

with the smallest mesh size down to 0.5nm. We first simulated the modulator based on the plasmonic waveguide platform as shown in Fig. 6.4(a). We assume the modulator is embedded in a waveguide with same configuration as itself except without the ITO layer. The length of the EO modulator is 150nm. Figures 6.4(b) and (c) show the power distribution in the waveguide at $N=N_1$ and $N=N_2$, respectively. Simulation results demonstrate that the overall throughput is 89.6% at $N=N_1$, and 40.8% at $N=N_2$. Note that the insertion loss is only 0.48 dB (89.6%). The achievable modulation depth, 3.42 dB, is very close to the one predicted by the 3D mode solver. We also simulated the modulator based on the dielectric waveguide platform as shown in Fig. 6.4(d). The length of the EO modulator is 200nm. In this case, we assume the modulator is embedded in a dielectric waveguide with same overall dimensions as itself except without the ITO and buffer layers. Figures 6.4(e) and (f) show the power distribution in the waveguide at $N=N_1$ and $N=N_2$, respectively. Simulation results demonstrate that the overall throughput is 88.2% at $N=N_1$, and 39.1% at $N=N_2$. The achievable modulation depth, 3.53 dB, is smaller than the one predicted by the 3D mode solver. This is due to the mode mismatch between the slot waveguide of the modulator and its input/output rib waveguide. We expect that its performance (modulation depth and insertion loss) can be significantly improved by replacing the input/output rib waveguide with a dielectric slot waveguide.

The design of the EO modulator is ultracompact and has much lower insertion loss compared with previous works, in which a modulation depth around 3 dB need the modulator lengths of 4μm [226] and 50μm [82], respectively. In most works, the insertion loss is either not reported or quite large. For example, the insertion loss is over 3.7 dB in Ref. [82].

In addition, the optical bandwidth of the modulators can be over several THz due to the slow Drude dispersion [227]. The EO modulators can potentially work at an ultra-high speed,

being mainly limited by the RC delay imposed by electric circuits.

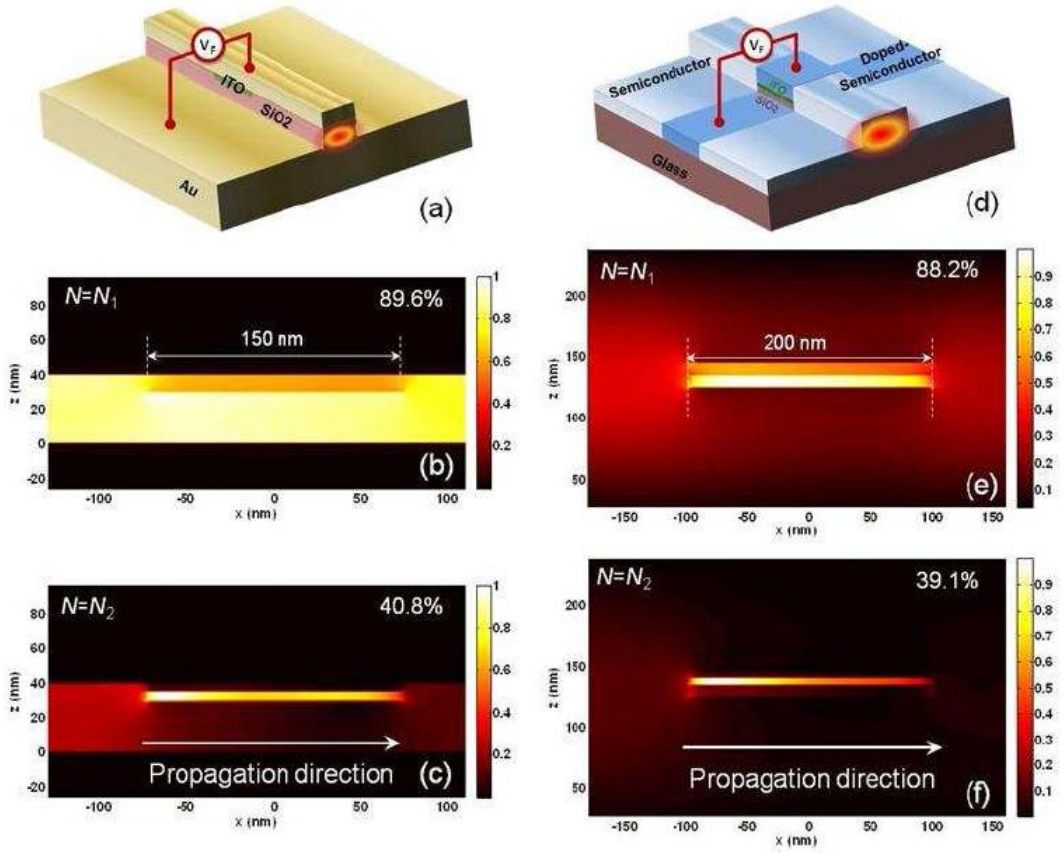

Figure 6.4 (a) The illustration of an EO modulator embedded in a plasmonic rib waveguide. (b,c) The 3D simulation of light propagation between a plasmonic rib waveguide and the EO modulator at $N=N_1$ and $N=N_2$, respectively. (d) The illustration of an EO modulator embedded in a dielectric rib waveguide. (e, f) The 3D simulation of light propagation between a dielectric rig waveguide and the EO modulator at $N=N_1$ and $N=N_2$, respectively. (b), (c), (e) and (f) are shown in normalized power distribution.

6.4 Conclusions

Recent research shows that transparent conductive oxides (TCOs) are promising tunable ENZ metamaterials. When sandwiched in a plasmonic or dielectric waveguide, a very thin ENZ film can greatly enhance light absorption. The tunable ENZ-slot waveguides may enable EO modulation at nanoscale and an optical modulator can be made at the scale of a transistor. In addition, the nanoscale modulators potentially have the advantages of small insertion los,

ultrahigh-speed, and easy fabrication. A similar work can be found in Ref. [227], where aluminum-doped zinc oxide (AZO) is the active material. The successfully development of this technique may lead to a significant breakthrough in on-chip optical interconnects.

7 GREATLY ENHANCED ABSORPTION OF MONOLAYER GRAPHENE IN AN ULTRABROAD BAND

In Chapter 5 and Chapter 6, we explored the electro-optic (EO) property of ITO and its potential applications in light modulation. From Chapter 7 to Chapter 8, we will focus on another natural metamaterial – graphene and investigate its properties which can be employed in modulators. In this chapter, greatly enhanced light absorption by monolayer graphene over a broad spectral range, from visible to near infrared, is experimentally demonstrated based on the attenuated total reflection. In the experiment, graphene is sandwiched between two dielectric media referred as superstrate and substrate. Based on numerical calculation and experimental results, the closer the refractive indices of the superstrate and the substrate, the higher the absorption of graphene will be. The light absorption of monolayer graphene up to 42.7% is experimentally achieved [205]. Compared to other reported works [248,265-269], our work doesn't need any complicated, time-consuming fabrication process and the greatly enhanced absorption is shown to be broadband.

7.1 Introduction

Graphene [229,230] is the first two-dimensional (2D) atomic crystal available to researchers, which is a basic building block for graphitic materials of all other dimensionalities [231], as shown in Fig. 7.1. Since it was isolated by mechanical exfoliation in 2004 [229], many extraordinary properties of graphene have been demonstrated. For example, graphene can support remarkably high density of electric currents [232], and has high thermal conductivity [233] and elasticity [234]. At room temperature, the electron mobility of graphene is extremely high, up to

2.5×10^5 cm^2 V^{-1} s^{-1} [232,235]. This property enables graphene a desirable material in the advancement of nanoelectronics [236], for example, metal-oxide-semiconductor field effect transistor (MOSFET) channels [237], graphene nanoribbons [97,238,239], bilayer graphene transistor [240] and perforated graphene transistors [241-243]. The optical properties of graphene have intrigued considerable interest as well. Recent research revealed gate-variable optical conductivity [244] and high-speed operation [245] of graphene. These extraordinary properties combining with its high electron mobility make graphene a promising candidate satisfying the need of broadband optical modulators [78,222,246,247] and photodetectors [245,248].

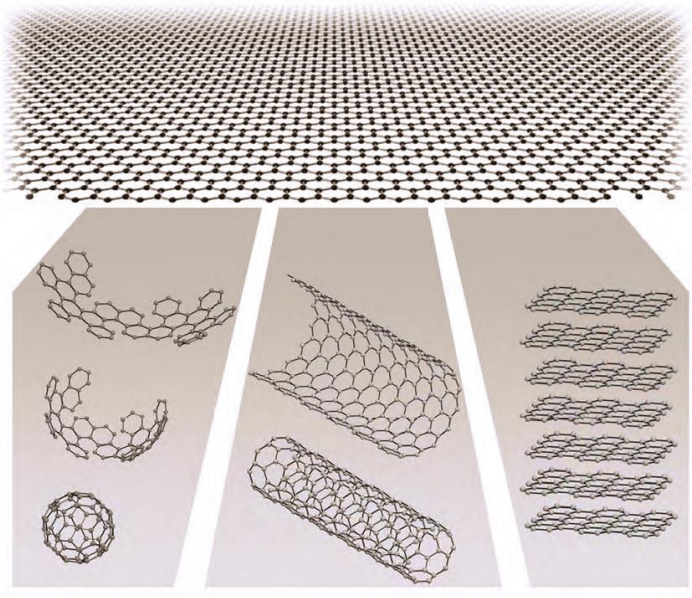

Figure 7.1 Illustration of the graphene (upper), 0D bucky balls (lower left), 1D nanotubes (lower middle), and 3D graphite (lower right). [231]

7.2 Optical Absorption of Graphene and Its Applications

The optical property of graphene is attracting researchers' interests. The light transmission (T) of a free standing monolayer graphene could be derived with Fresnel's equation for a thin film with a fixed universal optical constant [232,247] of $G = \frac{e^2}{4}$, to be:

$$T = \left(1 + \frac{\pi\alpha}{2}\right)^2 \approx 1 - \pi\alpha \approx 0.977, \tag{7.1}$$

where $\alpha = \frac{e^2}{4\pi\varepsilon_0 c} = \frac{G_0}{\pi\varepsilon_0 c} \approx \frac{1}{137}$ is the fine structure constant [249]. The reflectivity of graphene is very low (< 0.1%), therefore nearly 2.3% of the incident light will be absorbed by the graphene thin film, which is independent of the wavelength [244,249-251]. The absorption spectrum of a single layer graphene is quite flat for a wide wavelength range, from 300 to 2,500nm [252]. The large transmission combines the high conductivity, makes graphene a promising candidate in a variety applications, including solar cells, touch screens and organic light-emitting diodes (OLEDs). Indium tin oxide (ITO) is widely used in the above mentioned devices. Despite that ITO has an optical transparency of nearly 90% and a low sheet resistance (less than 100 Ω/□, which depends on process condition), it is brittle and expensive. With stable doping to increase conductivity and a controlled layer number, graphene could replace ITO as the transparent electrode in solar cells [253,254]. Graphene may also work as photoactive material [255] and the channel [256] in photovoltaic devices.

Graphene can be used with metals in the form of graphene/metal contacts in photo detectors [245], since it has a very wide spectrum of absorption and fast carrier transport. A Schottky-like barrier at a graphene/metal contact will be set up and generate a built-in electric field. Electron-hole pairs generated near the contact will be separated by the electric field and a net photocurrent can be observed [257-260]. Recently, interdigitated metal electrodes made of two different metals are employed in a graphene photo detector [261]. The design allows photo detection over the entire area of the device. Reliable detection of optical data streams of 1.55μm light pulses at a rate of 10 GBits/s can be obtained in this device [261].

7.3 Enhanced Optical Absorption by Graphene

7.3.1 Background

Considered its single atom thickness, the interaction between light and graphene is quite strong: light absorption can go up to $\pi\alpha$ = 2.293% (α is the fine-structure constant) [232,262-264] when light is normal incident through graphene. However, the absolute value (~2.3%) of absorption is still weak for most practical applications. For active optoelectronic devices [245,261,265], a strong light-matter interaction is usually desired. Therefore, many approaches have been explored to increase the interaction of light with graphene or to enhance the optical absorption. One possible way is to utilize plasmonic nanostructures [265] or nanoparticles [266] in graphene-based photodetectors, where the responsivity can be significantly enhanced due to the localized surface plasmons. It was also shown that the enhanced absorption of graphene can be achieved by patterning doped-graphene into a periodic nanodisk [267] or alternating with insulator layers to form superlattice structure [268]. More recent research work demonstrated that over 60% absorption can be reached by integrating graphene with a microcavity structure [248]. However, all these methods mentioned above either need complicated, time-consuming fabrication processes [248,269] or the devices exhibit very narrow bandwidth [248,266,269] due to the involvement of microcavities or resonators. An easily fabricated graphene-based device with a broad bandwidth is then desired for fundamental research and practical applications.

In a recent research [270], up to 10% light absorption by a monolayer graphene was demonstrated through an F2 prism coupling into a graphene-sandwiched silica waveguiding structure. The experimental setup used in Ref. [270] is based on an attenuated total reflection (ATR) configuration. This configuration has been used to measure the graphene absorption spectra [270], analyze terahertz surface plasmons on graphene [272], and estimate number of carbon layers in an unknown graphene sample [273].

7.3.2 Numerical Analysis

Here we consider a graphene-sandwiched three-layer structure as shown in the inset of Fig. 7.4(a). The top layer (superstrate), graphene, and bottom layer (substrate) have refractive indices, n_1, n_2, and n_3, respectively. Assume that a plane wave is incident into the three-layer structure and the corresponding propagation angles to the normal are θ_1, θ_2, and θ_3, respectively. Snell's law is held between layers, $n_q \sin\theta_q = n_1 \sin\theta_1 \equiv N$ (q=1, 2, 3). Based on the transfer matrix method (TMM) [197-199], the amplitude reflectance can be calculated by:

$$r = \frac{(n_3-n_2)(n_2+n_1)e^{+j\tilde{\varphi}_2}+(n_3+n_2)(n_2-n_1)e^{-j\tilde{\varphi}_2}}{(n_3-n_2)(n_2-n_1)e^{+j\tilde{\varphi}_2}+(n_3+n_2)(n_2+n_1)e^{-j\tilde{\varphi}_2}} \tag{7.2}$$

where $\tilde{\varphi}_2 = n_2 k_0 d \cos\theta_2$, k_0 is the wavenumber of the light wave in free space; $d \approx 0.335$ nm is the thickness of graphene). Also, $n_q = n_q \cos\theta_q$ (q=1, 2, 3) for s-polarized light, and $n_q = n_q/\cos\theta_q$ (q=1, 2, 3) for p-polarized light.

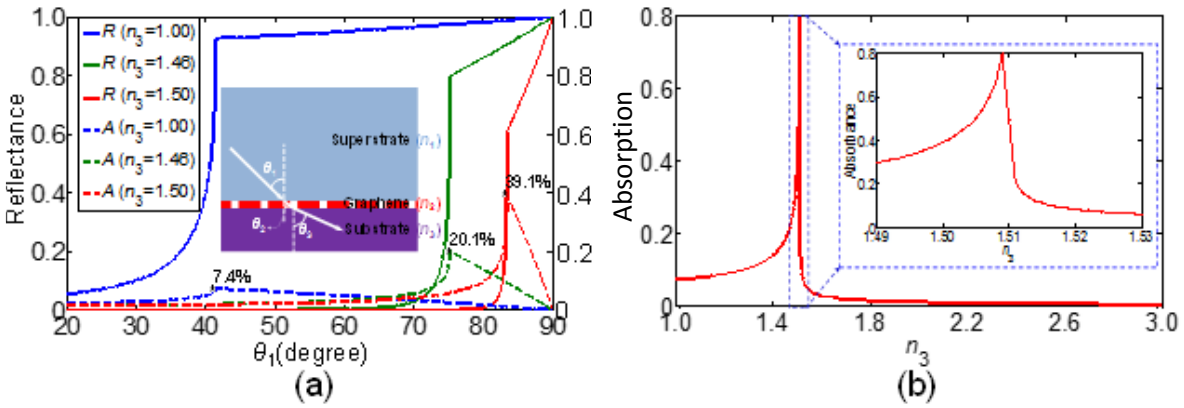

Figure 7.2 (a) Numerical calculation of the reflectance and absorption as functions of incident angle, θ_1, and substrate refractive index n_3. (b) Calculation of maximum achievable absorption as a function of substrate refractive index n_3. Results in (a) and (b) are obtained at λ=650nm for s-polarized light, and n_1=1.51. [205]

For pristine graphene, its surface conductivity σ_g can be universally expressed as $\sigma_g = \frac{\pi e^2}{2h} = 6.084 \times 10^{-5} S$, where h is the plank constant and e represents the elementary charge. Thus,

the refractive index of graphene is a complex number and can be calculated by $n_2 = \sqrt{1 + j\frac{\sigma_0}{\varepsilon_0 \omega d}}$, where ε_0 is the permittivity of the free space, and ω is the angular frequency of the incident light wave.

We assume the refractive index of the superstrate is n_1 = 1.51 at λ = 650nm, and first consider the *s*-polarized light case. The solid lines in Fig. 7.2(a) plot the power reflectance $R = |r|^2$as a function of incident angle θ_1 and substrate refractive index. Based on the transfer matrix method [197-199], we can similarly calculate the power transmittance *T*. The absorption *A*=1-*R*-*T*. The dashed lines in Fig. 7.2(a) plot the *A*-θ_1 relations for different substrates. Almost identical curves can be obtained at λ = 1520nm or even longer wavelengths if n_1 and n_3 remain the same as their corresponding values.

From the graph, we can see that the maximum absorption occurs at the critical angle $\theta_c = \sin^{-1}\left(\frac{n_3}{n_1}\right)$ for each case. This can be explained as follows. Due to the ultrathin thickness of graphene, the three-layer structure can also be approximately treated as a two-layer ($n_1|n_3$) structure, with the boundary replaced by graphene as a perturbation, if the graphene absorption is not significant. According to the continuity relation of electric field in different layers, the electric field in graphene, E_2, is proportional to the amplitude transmittance between the superstrate and substrate:

$$E_2 = t_s E_i = \frac{2n_1 \cos\theta_1 E_i}{n_1 \cos\theta_1 + n_3 \cos\theta_3}, \tag{7.3}$$

where E_i is the electric field of the incident light wave. The power dissipation in graphene in a unit area can be calculated by $p_d = \frac{1}{2}\sigma_g |E_2|^2$, and maximum $|E_2|$ gives rise to maximum p_d. In Eq. (7.3), $|E_2|$ reaches its maximum, $2|E_i|$, when $\cos\theta_3 = 0$ or equivalently $\theta_1 = \theta_c = \sin^{-1}\left(\frac{n_3}{n_1}\right)$.

Furthermore, the closer n_3 and n_1 are, the larger the critical angle, and the larger the absorption. The reason is because a larger critical angle decreases the incident power density on graphene, $S_i = \frac{1}{2\eta_1}|E_i|^2 \cos\theta_1$, which will increase the ratio between dissipated power and incident power, i.e.

$$A \approx \frac{p_d}{S_i} = \frac{\sigma_g \eta_1}{\cos\theta_1}\left|\frac{2n_1\cos\theta_1}{n_1\cos\theta_1+n_3\cos\theta_3}\right|, \tag{7.4}$$

where $\eta_1 = \eta_0/n_1$ is the impedance of the superstrate and $\eta_0 = 120\ \pi(\Omega)$ (the impedance of the free space). For normal light incidence into graphene suspended in air, $A \approx \sigma_g \eta_0 = 2.29\%$ in Eq. (7.4). When the absorption becomes significantly large, the amplitude transmittance cannot be estimated based on the above equation. Instead, the three-layer model needs to be applied.

Based on the three-layer model, the absorption grows with the increase of n_3, as shown in Fig. 7.2(b). The closer n_3 to $n_1^{(-)}$, the larger the absorption is. For example, the absorption can reach 79.6% when n_3=1.509. However, when n_3>n_1, the maximum absorption will sharply drop. In our work, we only consider the cases where n_1>n_3. The power transmittance T=0 when $\theta_1 \geq \theta_c$; thus, the incident power will be either reflected back or absorbed by graphene, i.e. A=1-R. The scattering by graphene is negligible as can be seen in the experimental result for *p*-polarized light. In other words, when $\theta_1 \geq \theta_c$, the absorption can be easily measured by testing the reflectance.

Furthermore, there is no cavity or resonant component involved in the structure. As a result, the absorption expression given in Eq. (7.4) is not an explicit function of frequency, which implies that the same level of enhanced light absorption can be achieved in a broad band. This is verified by the more accurate calculation based on the three-layer model: the absorption would slightly increase from 39.1% at 650nm to 39.2% at 1620nm if there were no material dispersion (n_1 and n_2 are actually slowly varying functions of frequency due to material dispersion). Consequently,

greatly enhanced ultrabroad band light absorption can be achieved simply based on the graphene-sandwiched three-layer structure.

7.3.3 Experimental Results and Discussion

To experimentally demonstrate the greatly enhanced light absorption by graphene, we have built an ATR setup in the Kretschmann configuration [197], as illustrated in Fig. 7.3. A collimated laser beam propagates through a broadband polarizer (P1) to choose either *s*- or *p*- polarized light, and is then split into two by a beam splitter (BS). One beam is used for recording source power fluctuation and fed into a germanium photodiode (PD2); another is incident at the angle θ_1 into a BK7 glass hemicylindrical (Ø100mm obtained from Rocoptonics) lens, which functions as a coupling prism in this setup. The reflected light is then collected by another germanium photodiode (PD1). The power ratio between PD1 and PD2 can well measure the reflectance, *R*, even if there is power fluctuation in the laser source. The rotation of the prism (together with the graphene sample) and PD1 is in a θ_1-$2\theta_1$ configuration, which is precisely controlled by two motorized rotation stages. In our experiment, we made one measurement for every 0.25 °increment of θ_1. As a result, the reflectance, *R*, as a function of θ_1 can be plotted.

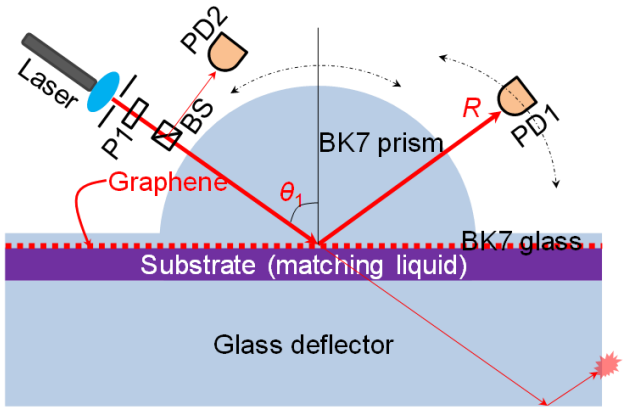

Figure 7.3 Illustration of the experimental setup for ATR measurement. The red dashed line represents the monolayer graphene film. P1 and BS represent the polarizer and beam splitter, respectively. [205]

Our sample is commercially available monolayer graphene [274] synthesized by the chemical vapor deposition (CVD) process then transferred to our bare BK7 glass slide. Its Raman spectroscopy result shown in Fig. 7.4 indicates that the sample is monolayer graphene with an obviously higher 2D peak than the G peak [275]. The graphene sample is mounted at the back of the hemicylindrical prism. To avoid a thin air gap between the prism and the graphene sample, a BK7 index matching liquid is applied between them. In this case, the superstrate can be simplified and treated as a BK7 medium, consisting of the BK7 prism and the BK7 glass slide. The medium on the other side of the graphene is referred as the substrate, which is another matching liquid from Cargille™ in our case to better control the refractive index. A thick (>10 mm) glass plate is used to hold the matching liquid and meanwhile to deflect light away from PD1.

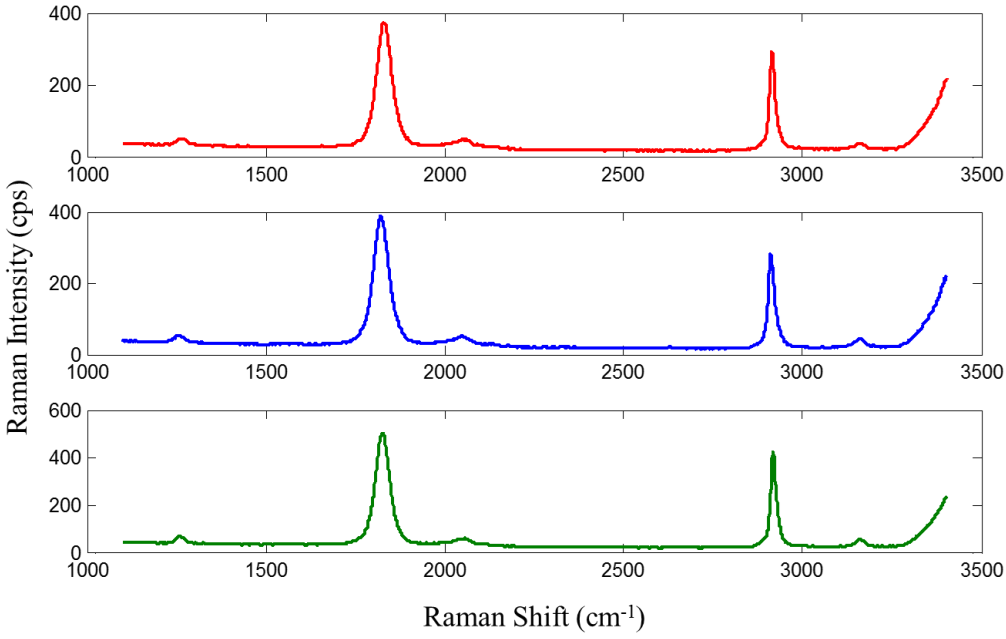

Figure 7.4 Raman spectroscopy result for the graphene sample. The three curves represent three different points on the same sample. [274]

In our work, we focused on *s*-polarization and carried out the experiment in a step-by-step fashion. First, we tested the graphene on BK7 glass sample without any substrate (or air as the

substrate), as shown in Fig. 7.3 but without the deflector. The experimentally measured reflectance at λ = 650nm and 1520nm as a function of θ_1 is shown in Fig. 7.5(a) and (b), respectively. In order to calculate the absorption of the monolayer graphene, the reflectance (blue triangles) of a bare BK7 glass slide is measured as a control experiment. The critical angle is measured to be 41.00 ° (at λ=650nm) and 41.25 ° (at λ=1520nm), which is in agreement with the theoretical calculation value 41.3 °(at λ=650nm) and 41.8 °(at λ=1520nm). The discrepancy is attributed to the angle error in θ_1, and corrected in our following calculation.

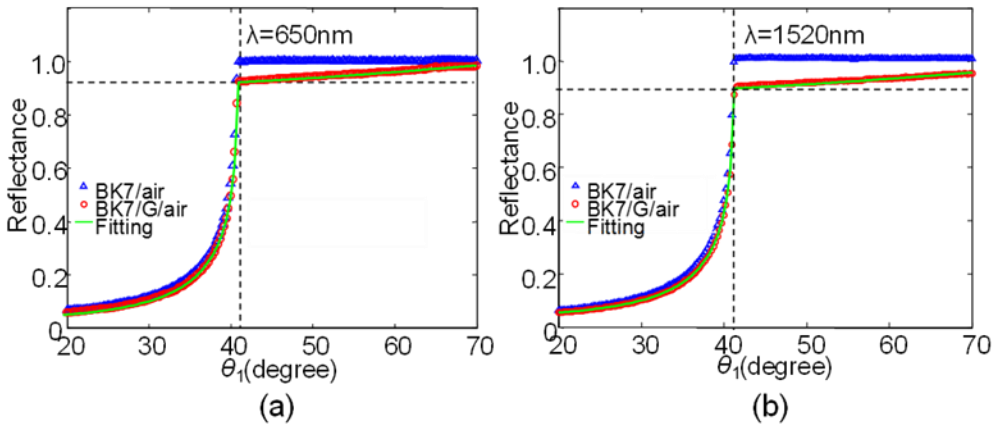

Figure 7.5 Reflectance of a reference BK7 glass slide (blue triangles), monolayer graphene (red circles), and numerical fit (green) with an s-polarized light (a) with wavelength of λ = 650 nm and (b) λ = 1520 nm. In the legend, "G" represents "graphene". "BK7/G/air" means the result with the BK7(prism)-graphene-air configuration. [205]

In each plot, both the reflectance curves are normalized by the average value of the total internal reflection part in the reference curve. Therefore, the red curve represents the reflectance of the monolayer graphene. At the critical angle, the absorption of the monolayer graphene can be calculated as A=1-R, which is 7.6% (at λ=650nm) and 9.8% (at λ=1520nm). The measured reflectance of the monolayer graphene is numerically fitted (green curve in Fig. 7.5) by calculating the reflectance through the three-layer structure based on the transfer matrix method (TMM) [197-199]. In the numerical fitting, the BK-7 medium has a refractive index of n=1.50 at λ=1520nm.

We use the dielectric constant of graphene (imaginary part) as the fitting parameter to approach the measured reflectance data. The result turns out that the dielectric constant of graphene ε_g= 1+j15.96 or surface conductivity σ_g=6.22×10^{-5}S at λ=1520nm. We attribute the discrepancy between the fitted value and the theoretical value calculated by Eq. (7.2) to the doping in graphene. A slightly smaller conductivity can also be fitted for the result measured at λ=650nm.

Based on the same sample and configuration, we also measured the absorption of graphene at longer wavelengths up to 1620nm. At the critical angle, the absorption of monolayer graphene is in the range of 7.6%-11.2%, which is 3~5 times stronger than the widely known absorption coefficient (~2.3%). When the incident angle is larger than the critical angle, the reflectance of graphene is observed to gradually increase and projected to be 100% at θ_1 = 90 º.

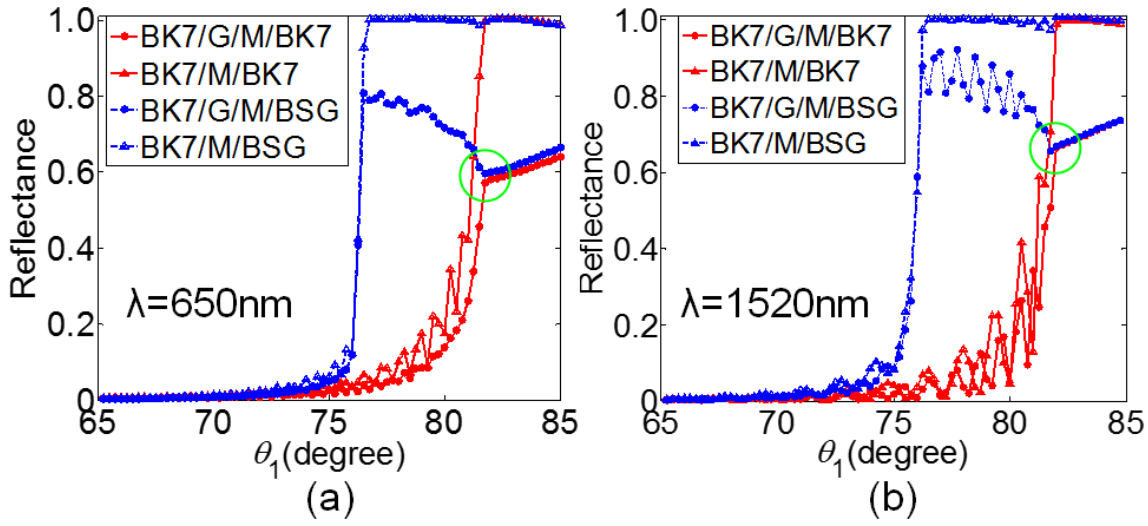

Figure 7.6 (a) Normalized measured reflectance of the monolayer graphene with M1.50 as substrate under s-polarized light incidence at λ=650nm. (b) Measured reflectance of the monolayer graphene with M1.50 as substrate under s-polarized light incidence at λ=1520nm. In both graphs, red curves represent the results when a BK7 deflector is used; blue curves represent the results when a BSG deflector is used. In the legend, "G" and "M" represent "graphene" and "matching liquid", respectively. "BK7/G/M/BK7" means the result for the BK7(prism)-graphene-M1.50(substrate)-BK7(deflector) configuration. [205]

The absorption of the monolayer graphene can be further enhanced when the refractive index of the substrate increases. In our work, a matching liquid with refractive index 1.50 (at λ=589.3nm according to the manufacturer; referred as "M1.50") is applied as the substrate of the graphene. Two different supporting glass deflectors, BK7 and borosilicate glass (BSG), are separately used to hold the substrate M1.50. In Fig. 7.6, triangle points are the control experiments measured by "removing" the graphene. Both the curves measured with graphene sample are normalized with the corresponding control curves.

In the control experiment with BK7 deflector, the total internal reflection occurs at the interface of the superstrate BK7 and the substrate M1.50, $\theta_C \approx 81.75°$. As shown in the red dot curve, at θ_C the absorption of monolayer graphene is measured as 42.7%, which is ~18 times stronger than the widely known absorption (~2.3%).

This result is further confirmed by replacing the BK7 deflector with the BSG deflector and repeating the measurement, as shown in the blue dot curves in Fig. 7.6(a), where the absorption is measure as 40.5%. In this configuration, there are two total internal reflections: first one occurs at the interface of the substrate M1.50 and BSG deflector with a critical angle $\theta_{C1} \approx 76.75°$, and the second one occurs at the interface of the superstrate BK7 and the substrate M1.50 with $\theta_{C2} \approx 81.75°$. Beyond θ_{C2}, the blue dot curve is in a good agreement with the red dot curve, and both indicate the reflectance of the monolayer graphene in the sandwich configuration. The oscillation of the blue triangle curve between the two angles θ_{C1} and θ_{C2} is due to the substrate M1.50 functioning as a cavity between the graphene and BSG deflector.

Similarly, R-θ_1 relation at different wavelengths is measured. Figure 7.6(b) shows the results for the measurement at λ=1520nm. The absorption is about 35.3% at the critical angle. When the wavelength varies from 650nm to 1620nm, the absorption gradually decreases from 40.5%

to 33.1% with the BSG deflector, and from 42.7% to 35.3% with the BK7 deflector. Thus, ultrabroad band enhanced light absorption is achieved. The variation of the absorption with the wavelength can be attributed to the dispersion of the superstrate BK7 and substrate M1.50. In particular, the absorption becomes more sensitive when n_1 and n_3 are close enough. When the substrate is replaced by M1.49 matching liquid, the absorption will considerably decrease, for example, dropping from 42.7% to 28% at λ=650nm.

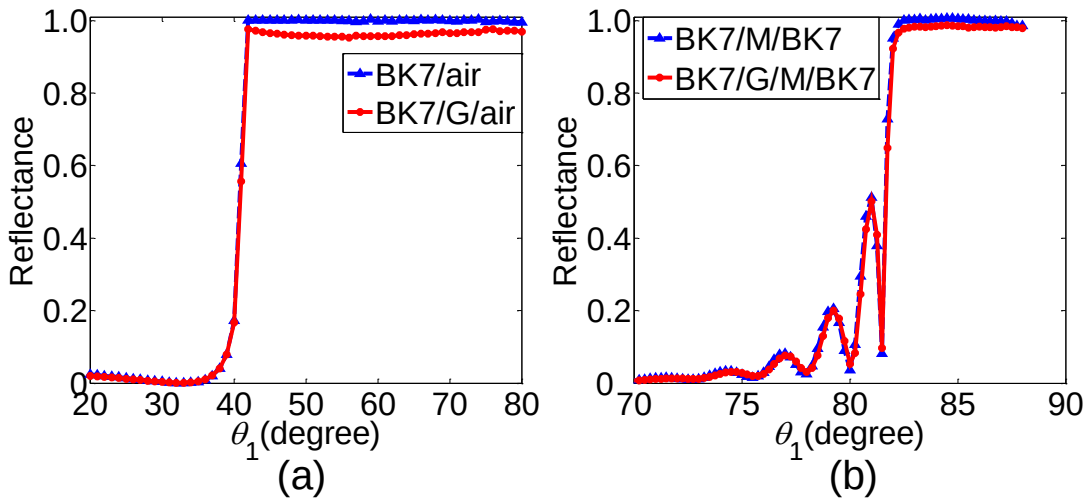

Figure 7.7 For 1520nm *p*-polarized light incidence, the normalized measured reflectance by the monolayer graphene sample as a function of incident angle when (a) the substrate is air, and (b) the substrate is M1.50. [205]

The enhanced absorption of graphene is shown to be very sensitive to the polarization of the incident light. Similar as previous experiments, we measured the reflectance of the monolayer graphene when the substrate is air and M1.50 separately with *p*-polarized incident light. As can be seen in Fig. 7.6, the maximum absorption does not occur at the critical angle and is not sensitive to the substrate refractive index. The minimum reflectance beyond the corresponding critical angle is 97.65% (when the substrate is air) or 97.7% (when the substrate is M1.50), respectively. Therefore, the absorption in both cases is calculated as ~2.3%, which is similar as the widely

known absorption coefficient. The reason is because the electric field in graphene for *p*-polarized incident light cannot be estimated by Eq. (7.3), instead

$$|E_2| = |E_{2t}| + |E_{2n}| \approx \left|\frac{2n_1 \cos\theta_1 E_i}{n_1 \cos\theta_3 + n_3 \cos\theta_1}\right| \sqrt{\left(|\cos\theta_3|^2 + \left|\frac{n_3}{n_2}\sin\theta_3\right|^2\right)}. \quad (7.5)$$

where E_{2t} and E_{2n} represents the tangential and normal components of the electric field in graphene. Therefore, when $\theta_1 = \theta_C = \sin^{-1}\left(\frac{n_3}{n_1}\right)$, $\cos\theta_3 = 0$ and $E_{2t} = 0$, which is opposite to that case for *s*-polarized light. In the latter case, $E_2 = E_{2t}$ gains its maximum when $\theta_1 = \theta_c$.

7.4 Conclusions

In this work, we have experimentally demonstrated that the absorption of monolayer graphene can be significantly enhanced over a broad spectral range, from visible to infrared, when the incident light is *s*-polarized. At the critical angle, the absorption is in the range of 7.6%-11.2%, when the substrate is air, and up to 42.7%, when the substrate is replaced by a medium with a closer refractive index compared to that of the superstrate. The enhanced absorption is not strongly dependent on the wavelength but very sensitive to the polarization of incoming light. The significantly enhanced absorption of monolayer graphene may have potential applications in broadband photodetectors and solar cells.

8 NANOSCALE ELECTRO-OPTIC MODULATORS BASED ON GRAPHENE

Research on graphene has revealed its remarkable electro-optic properties, which promise to satisfy the needs of future electro-optic modulators. However, its ultrasmall thickness, compared with operating light wavelength, downplays its role in an optoelectronic device. The key to achieve efficient electro-optic modulation based on graphene is to enhance its interaction with light. To this end, some novel waveguides and platforms will be employed to enhance the interaction. In this chapter, we will continue the work in Chapter 7 and present the recent exploration of graphene electro-optic modulators based on graphene sandwiched in dielectric or plasmonic waveguides [222]. With a suitable gate voltage, the dielectric constant of graphene can be tuned to be very small due to the effect of intraband electronic transition, resulting in "graphene-slot waveguides" and greatly enhanced absorption modes. Up to 3 dB modulation depth can be achieved within 800nm long silicon waveguides, or 120nm long plasmonic waveguides based on three-dimensional numerical simulations. They have the advantages of nanoscale footprints, small insertion loss, low power consumption, and potentially ultrahigh speed, as well as being CMOS-compatible.

8.1 Introduction

Surface plasmon polaritons (SPPs) are collective oscillations of electrons at the interface of dielectric/metal, which can be excited by photon or electron. Usually, noble metals (Au or Ag) are used as the plasmonic materials. However, high loss and non-tunability are the main disadvantages of the devices fabricated with these materials. As a rising star, graphene has been proposed as a new platform for plasmon waveguiding at infrared frequencies [68-74], and also considered as terahertz metamaterials [75]. SPPs excited in graphene have many promising

properties [72,276], for example, extremely strong confinement, tunability with electrical gating or chemical doping, and low loss. Hence, graphene is an attractive alternative to traditional plasmonic materials. Graphene as plasmonic material has been demonstrated in light harvesting [277], optical biosensing [278], and transformation optics [76]. The tunability of graphene-based plasmonic devices originates from its complex dynamic conductivity determined by the Kubo formula [73,76,77], which will be discussed in the following section of this chapter. Simply speaking, the imaginary part of the conductivity σ" may has a negative or positive value which depends on the chemical potential of graphene at different frequency ranges, and it plays an important role in supporting different types of surface waves. With a low chemical potential, graphene has a negative σ", leading to a semiconductor-like behavior, capable of guiding a proper TE surface wave. With a large chemical potential ($|\mu|>\hbar\omega/2$), σ" is positive and graphene will behave like metal and support a proper TM surface wave, which shows similar behavior as noble metals [279-282].

8.2 Intraband absorption of graphene

8.2.1 Surface conductivity model of graphene

Graphene can be modeled as an infinitesimally-thin, local two-sided surface characterized by a surface conductivity $\sigma(\omega, \mu_c, \Gamma, T)$, where ω is radian frequency, μ_c is chemical potential, Γ is scattering rate, and T is temperature. The conductivity of graphene can be expressed by the Kubo formula [73,76,77],

$$\sigma(\omega,\mu_c,\Gamma,T)=\frac{je^2(\omega-j2\Gamma)}{\pi\hbar^2}\left[\frac{1}{(\omega-j2\Gamma)^2}\int_0^\infty \varepsilon\left(\frac{\partial f_d(\varepsilon)}{\partial\varepsilon}-\frac{\partial f_d(-\varepsilon)}{\partial\varepsilon}\right)d\varepsilon-\int_0^\infty\frac{f_d(-\varepsilon)-f_d(\varepsilon)}{(\omega-j2\Gamma)^2-4(\varepsilon/\hbar)^2}d\varepsilon\right] \quad (8.1)$$

where e is the charge of an electron, $\hbar=h/2\pi$ is the reduced Planck's constant, $f_d(\varepsilon)=\left(e^{(\varepsilon-\mu_c)/k_BT}+1\right)^{-1}$ is the Fermi-Dirac distribution, and k_B is Boltzmann's constant. The local

conductivity is isotropic, where there is no external magnetic field is present. The first term in Eq. (8.1) is contributed by intraband absorption, and the second one by interband absorption.

From equation (8.1), the surface conductivity of graphene can be simplified as $\sigma = \sigma_{intra}(\omega, \mu_c, \Gamma, T) + \sigma_{inter}(\omega, \mu_c, \Gamma, T)$. The chemical potential μ_c is determined by the carrier density n_s

$$n_s = \frac{2}{\pi\hbar^2 v_F^2} \int_0^\infty \varepsilon \left(f_d(\varepsilon) - f_d(\varepsilon + 2\mu_c) \right) d\varepsilon, \tag{8.2}$$

where $v_F \approx 9.5E+5$ m/s is the Fermi velocity. By applying a gate voltage or chemical doping, the carrier density can be easily controlled. Thus, the conductivity of graphene can be dynamically tuned by gate voltage V_D in real time. Basically, when $\mu_c < \hbar\omega/2$, interband absorption dominates and graphene becomes absorptive; otherwise, quite transparent. Electrically switching on/off graphene interband absorption plays a key role in the modulator reported in Ref. [247].

The intraband term in Eq. (8.1) can be written as

$$\sigma_{intra}(\omega, \mu_c, \Gamma, T) = -j \frac{e^2 k_B T}{\pi\hbar^2(\omega - j2\Gamma)} \left(\frac{\mu_c}{k_B T} + 2\ln\left(e^{-\frac{\mu_c}{k_B T}} + 1 \right) \right), \tag{8.3}$$

and the interband term can be approximated for $k_B T \ll |\mu_c|$,

$$\sigma_{inter}(\omega, \mu_c, \Gamma, T) \approx \frac{-je^2}{4\pi\hbar} \ln\left(\frac{2|\mu_c| - (\omega - j2\Gamma)\hbar}{2|\mu_c| + (\omega - j2\Gamma)\hbar} \right). \tag{8.4}$$

The complex surface conductivity can be simply expressed as $\sigma = \sigma' + j\sigma''$, as mentioned in the introduction part, at low frequency regimes, a proper TE surface wave exists only if $\sigma'' > 0$ (associated with intraband absorption), and a proper TM surface wave exists for $\sigma'' < 0$ (associated with interband absorption) [283].

8.2.2 Intraband absorption

We found the intraband absorption can be equally important in a graphene absorption

modulator. Based on Eq. (8.1), we calculated the graphene conductivity at T = 300K (scattering rate, $\hbar\Gamma$ = 5 meV) [247]. Figures 8.1(a) and 1(b) plot the real and imaginary parts of the conductivity as a function of the chemical potential and wavelength in the near-infrared regime. In particular, the real part of conductivity is very sensitive to chemical potential; for example, at wavelength λ_0 = 1550nm, varying from nearly 60.85μS to 1.37μS when chemical potential rises from 0 to 0.6eV, as shown in Fig. 8.1(c). Figure 8.1(c) also shows how interband absorption and intraband absorption contribute to the graphene conductivity, respectively. Figure 8.1(d) plots the corresponding dielectric constant (real part, imaginary part, and magnitude), $\varepsilon_{eff}(\mu_c) = 1 - \frac{\sigma_v}{j\omega\varepsilon_0} = 1 - \frac{\sigma_g}{j\omega\varepsilon_0\Delta}$, where Δ = 0.7nm is the effective thickness of graphene [247]. The dielectric constant of graphene varies from ε_{eff} (0 eV) = 0.985 + j8.077 to ε_{eff}(0.6 eV) = −2.508 + j0.182 at λ_0 = 1.55μm. Note the sign of real part flips due to intraband absorption because the interband absorption and intraband absorption contribute to the imaginary part of conductivity with different signs, as shown in Fig. 8.1(c). As a result, there is a dip in the curve of dielectric constant magnitude, where "metallic graphene" is transforming to "dielectric graphene" with Ref{ε_{eff}} = 0. In this case, the "transition chemical potential" is μ_t = 0.515 eV and $|\varepsilon_{\text{eff}}(\mu_t)|$ = |− 0.048 + j0.323| = 0.327, which means the magnitude varies $|\varepsilon_{\text{eff}}(0)|/|\varepsilon_{\text{eff}}(\mu_t)| \approx 25$ times. Note this "epsilon-near-zero" [218,219,284] effect can be seen almost in any material at its plasma frequency; for example, Ag at λ_0 = 326nm. The uniqueness of graphene lies in that its plasma frequency can be tuned by electrical gating.

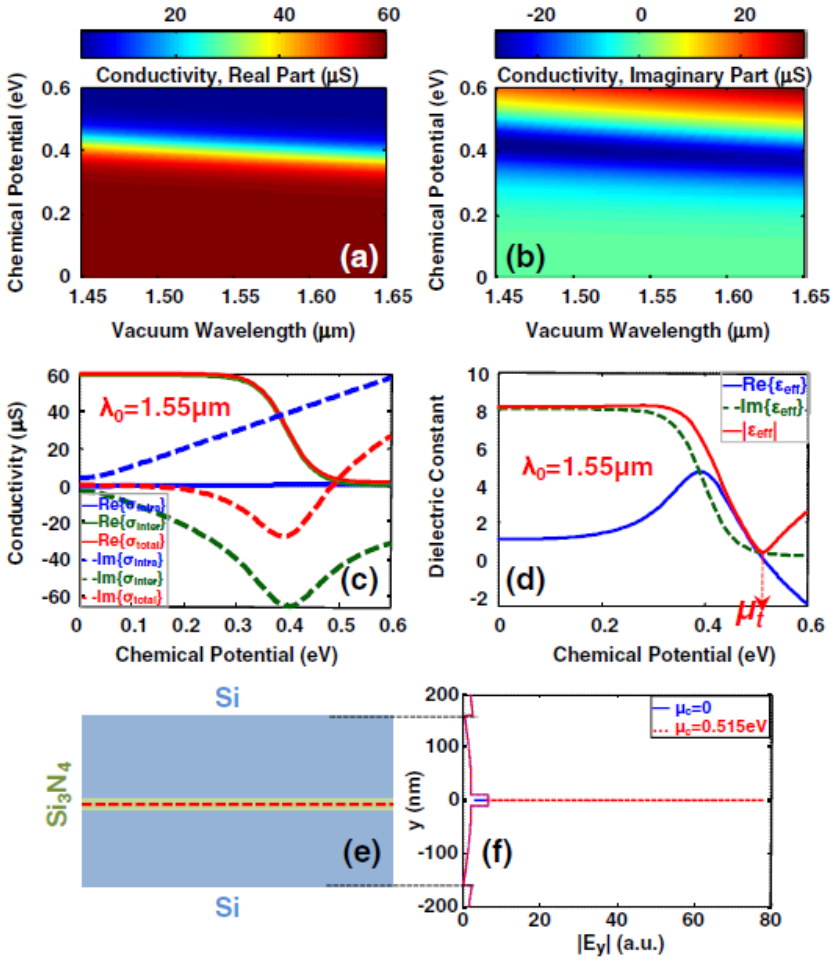

Figure 8.1 (a) Real part and (b) imaginary part of the graphene conductivity as a function of chemical potential and wavelength (T = 300K) based on the Kubo formula. (c) The graphene conductivity (real part and imaginary part), by interband transition and intraband transition, as the function of chemical potential at λ_0 = 1550nm. (d) The effective dielectric constant (real part, imaginary part, and magnitude) as a function of chemical potential at λ_0 = 1550nm. (e) The illustration of a 2D "graphene-slot waveguide" with a 10nm thick Si_3N_4 buffer layer on each side of graphene. (f) The plots of the transverse electric field magnitude across the waveguide at $\mu_c = 0$ and $\mu_c = \mu_t$, respectively. [222]

8.3 Design and modeling

8.3.1 Significantly enhanced absorption in graphene-slot waveguide

The effect of dielectric constant change is not very manifest when graphene is placed on top of a dielectric waveguide. Based on the change of dielectric constant, we solved the transverse magnetic (TM) modes of graphene on a 250nm by 600nm silicon waveguide with a 7nm Al_2O_3 buffer layer at λ_0 = 1.53μm when chemical potential is 0 and μ_t, respectively. The effective indices

are both 2.06, but the attenuation rates are significantly different, 0.134 dB/μm for $\mu_c = 0$ and 0.044 dB/μm for $\mu_c = \mu_t$. The mode profiles are shown in Fig. 8.2(a) and (b), respectively. The absorption can be further reduced when μ_c shifts from 0.515 eV to 0.6 eV or higher. The resulting modulation, 0.09 ~ 0.13 dB/μm, coincides with the recent experimental work [247].

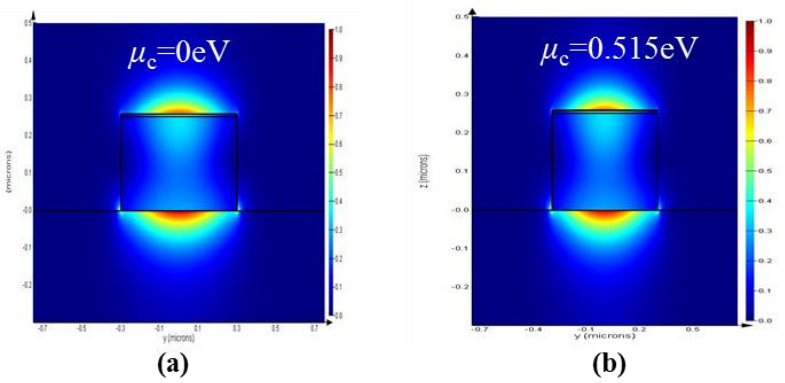

Figure 8.2 Mode profiles for graphene on top of dielectric waveguide. [247] (a) At $\mu_c = 0$, attenuation α= 0.134dB/μm, and (b) at $\mu_c = 0.515$ eV, attenuation α= 0.044dB/μm. Both figures are shown in normalized electric fields.

The absorption of a TM mode can be greatly enhanced when graphene is sandwiched inside the silicon waveguide, forming a "graphene-slot waveguide," as illustrated in Fig. 8.1(e). In a slot waveguide [285], the magnitude of transverse electric field $|E_y|$ is roughly inversely proportional to that of the dielectric constant. The power absorbed in a unit area, $p_d = \frac{1}{2} Re\{\sigma_g\} E^2 \propto \frac{1}{2} E \cdot Im\{\varepsilon_{eff}\} / |\varepsilon_{eff}|$, can be greatly enhanced at $\mu_c = \mu_t$ because (1) $|E_y|$ reaches its maximum, and (2) $\mathrm{Im}\{\varepsilon_{\mathrm{eff}}\}/|\varepsilon_{\mathrm{eff}}|$ nearly grows to its maximum at the same time, as shown in Fig. 8.1(d). To verify this, we first consider the multilayer stack, as illustrated in Fig. 8.1(e), where graphene is sandwiched in a silicon waveguide with a 10nm Si_3N_4 buffer layer on each side. Based on the transfer matrix method, we find the optimal silicon thickness to enhance light absorption is about 150nm. Figure 8.1(f) plots the $|E_y|$ profiles at $\mu_c = 0$ and $\mu_c = \mu_t$, respectively. The absorption is roughly proportional to $|E_y|$, with an enhancement about 25 times. In our case, $\mu_c = 0$ is the transparence

state, while $\mu_c = \mu_t$ is the absorption state, which are exactly opposite to the operation principle of the EO modulator reported in Ref. [247] as well as the graphene-sandwiched devices proposed in a recent review article [286]. In those devices, the electric field strength for the two states is at the same level and the imaginary part of graphene dielectric constant determines the absorption. Graphene has higher conductivity (and larger imaginary part of dielectric constant) at $\mu_c = 0$.

8.3.2 Mode profiles

Once the configuration of the graphene-slot waveguide is optimized, we use a three-dimensional (3D) mode solver to determine the optimal waveguide width based on the finite-difference time-domain (FDTD) method. Considering the fabrication tolerance, the optimal width of the waveguide is found to be 450nm. Figure 8.3(a) shows the mode profiles of the graphene-slot waveguide at different chemical potentials. There is only a slight shift in the effective index: 2.032 at $\mu_c = 0$, and 2.034 at $\mu_c = \mu_t$. In contrast, there is a huge change in the waveguide attenuation. At $\mu_c = 0$, the $|E_y|$ in the graphene is even lower than in the Si_3N_4 buffer layers, and the waveguide works at the low loss state with $\alpha_0 = 0.183$ dB/μm; at $\mu_c = \mu_t$, the $|E_y|$ in the graphene is many times higher than in the Si_3N_4 buffer layers, and the waveguide works at the high absorption state with $\alpha_v = 4.603$ dB/μm. As a result, modulation depth 4.42 dB/μm can be achieved, and 3 dB modulation depth only requires 679nm propagation distance. An 800nm propagation distance results in modulation depth 3.54 dB. Therefore, a graphene EO modulator can be made on the nanoscale. For the sake of easy fabrication, the silicon modulator can also take the form of an asymmetric slot waveguide, as shown in Fig. 8.3(b). There is only a slight change in the performance.

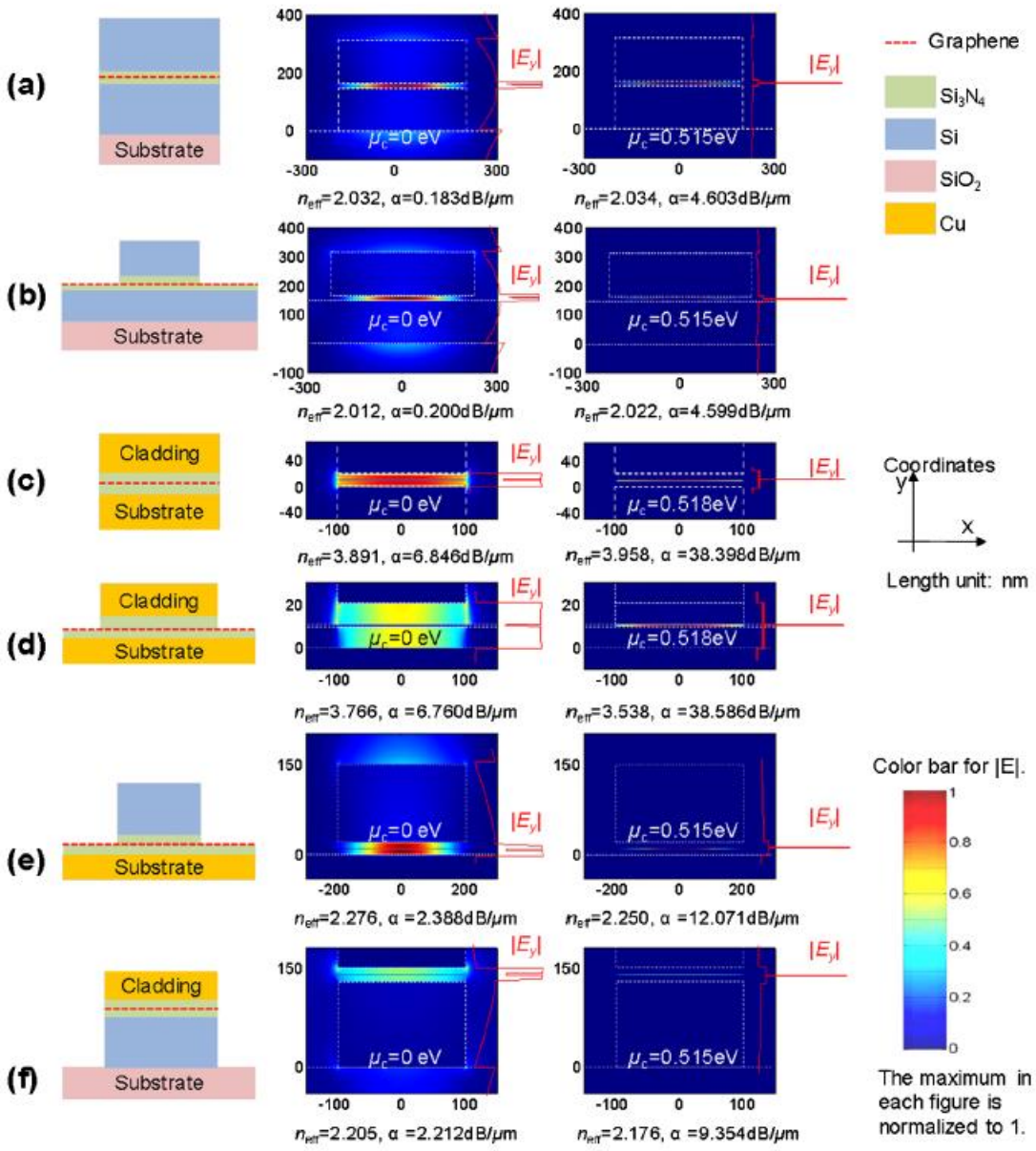

Figure 8.3 The transverse electric field profiles, effective indices, and propagation loss for different graphene-slot waveguides at $\mu_c = 0$ and $\mu_c = \mu_t$, respectively: (a) in a dielectric waveguide (Si waveguide is 450nm wide and 150nm thick for each layer); (b) in a dielectric strip waveguide (strip Si waveguide is 450nm wide and 150 nm thick for each layer); (c) in a metal-insulator-metal waveguide (waveguide is 200 nm wide); (d) in a metal strip waveguide (strip metal is 200nm wide); (e), (f) in photonic-plasmonic hybrid waveguides [waveguide is 400 nm wide in (e) and 200 nm wide in (f), Si layer is 130 nm thick for both structures]. All mode profiles are shown in normalized electric fields. The refractive indices of Si, Si_3N_4, and SiO_2 are assumed to be 3.47, 1.98, and 1.44, respectively. [222]

Furthermore, recent work shows that highly confined modes can be achieved in plasmonic waveguides [287]. Based on nanoplasmonic platforms, the dimensions of a graphene modulator

should be even smaller. Following the same approach, we investigated the interaction between graphene and various plasmonic modes. Figures 8.3(c) and 8.3(d) list the guided mode profiles, effective indices, and attenuation of graphene-slot waveguides based the metal-insulator-metal plasmonic platform. Because of the close interaction between metal and graphene, the chemical potential with highest absorption shifts to 0.518 eV. Figures 8.3(e) and 8.3(f) list the mode calculation of graphene-slot waveguides based on the hybrid plasmonic platform. Although Au or Ag may decrease the metal absorption of the plasmonic waveguides, CMOS-compatible metal, Cu, is used in all plasmonic modulators, and its dielectric constant is assumed to be $-67.86 + j10.01$. A 10nm thick Si_3N_4 buffer layer is designed on each side of graphene for all plasmonic waveguides shown in Figs. 8.3(c)–8.3(f). As can be seen in Fig. 8.3(d), a 3 dB (3.82 dB at 1550nm) EO modulator can be made within 120nm using the metal strip plasmonic waveguide, where the attenuations are 6.76 dB/μm at $\mu_c = 0$, and 38.59 dB/μm at $\mu_c = 0.518$ eV.

8.4 Performance analysis

8.4.1 Insertion loss

To evaluate the insertion loss of the EO modulators, we performed 3D FDTD simulations with the smallest mesh size down to 0.35nm. In the simulations, we assume the modulators are embedded in the same waveguide as themselves except without the sandwiched graphene. We first simulated the modulator based on the silicon waveguide platform, as shown in Fig. 8.4(a). The length of the graphene modulator is 800nm. Assume the thickness of the bottom silicon layer for electrical contact is negligible. Figures 8.4(b) and 8.4(c) show the power distribution in the waveguide at $\mu_c = 0$ and $\mu_c = 0.515$ eV, respectively. Simulation results demonstrate that the overall throughput is 92.0% at $\mu_c = 0$, and 42.5% at $\mu_c = 0.515$ eV. Note that the insertion loss is only 0.36 dB (92.0%). The achievable modulation depth, 3.4 dB, is slightly smaller than the one predicted

by the 3D mode solver. We also simulated EO modulators based on the guided modes listed in Figs. 8.3(b)–8.3(f). The results are similar as predicted in the mode solver. As one example, Figs. 8.4(e) and 8.4(f) show the simulation results at μ_c = 0 and μ_c = 0.518 eV for the plasmonic modulator illustrated in Fig. 8.4(d). The overall throughput is 81.04% at μ_c = 0, and 36.92% at μ_c = 0.518 eV. Note that the overall length is only 120nm, while the modulation depth is 3.4 dB.

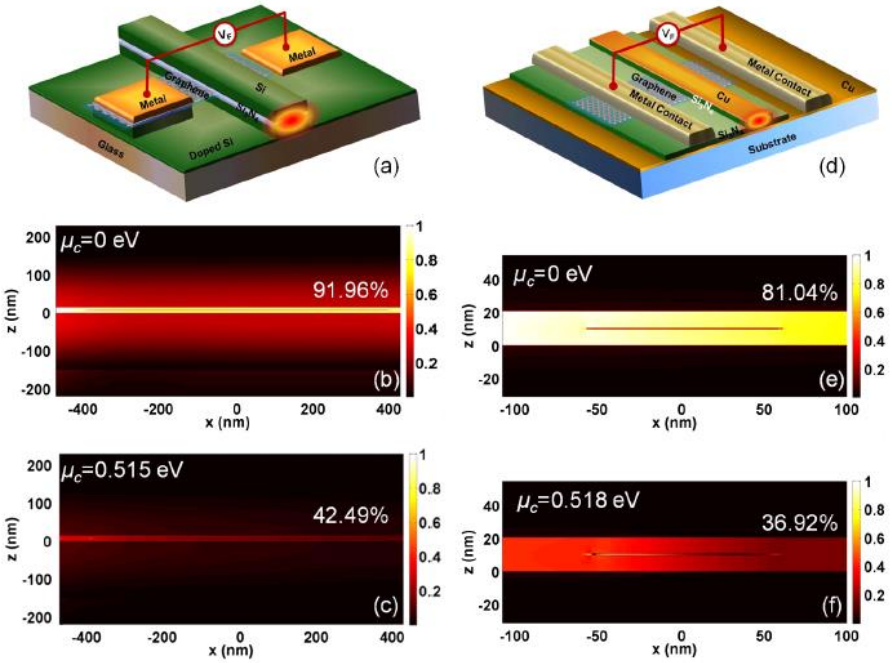

Figure 8.4 The illustration of a graphene EO modulator based on a silicon waveguide. (b), (c) The 3D simulation of light propagation between a silicon waveguide and the EO modulator at μ_c = 0 and μ_c = μ_t, respectively. (d) The illustration of a graphene EO modulator based on a metal strip plasmonic waveguide. (e), (f) The 3D simulation of light propagation between a metal strip plasmonic waveguide and the EO modulator at μ_c = 0 and μ_c = μ_t, respectively. Figures (b), (c), (e) and (f) are shown in normalized power distribution. [222]

8.4.2 Bandwidth

On-chip optical interconnects require a broad bandwidth. Although the conductivity of graphene only weakly depends on the working frequency, the effective dielectric constant, $\varepsilon_{eff}(\mu_c) = 1 - \frac{\sigma_g}{j\omega\varepsilon_0\Delta}$, is a function of working frequency. As a result, in terms of dielectric constant, graphene is a dispersive medium. Nevertheless, we found the effect of dispersion is not so obvious.

We studied the bandwidth of the EO modulators by solving the modes shown in Fig. 8.3 at different working wavelengths. Figure 8.5(a) shows the waveguide absorption as a function of wavelength in a silicon waveguide. As can be seen, the attenuation of the modulator at $\mu_c = 0$ nearly remains a constant, 0.18 − 0.20 dB/μm, while the attenuation at $\mu_c = 0.515$ eV decreases when the wavelength shifts away from 1550nm. In particular, the attenuations are 4.44dB/μm, 4.60dB/μm, and 4.45dB/μm at 1545nm, 1550nm, and 1555nm, respectively. Wavelength spanning from 1545nm to 1555nm, or 1.25THz bandwidth, only decreases modulation depth 0.16 dB/μm. For our 800nm silicon modulator, the decrease will be 0.14 dB. The prediction was further verified by 3D FDTD modeling. At $\mu_c = 0$, the overall throughput is 92% for both 1545nm and 1555nm; at $\mu_c = 0.515$ eV, the overall throughput is 43.7% and 43.6%, for 1545nm and 1555nm, respectively. Thus, this modulator has a 3 dB bandwidth at least 1.25 THz.

We also studied the bandwidth of our EO modulators based on plasmonic waveguides. Figure 8.5(b) shows the waveguide absorption as a function of wavelength in a metal strip plasmonic waveguide based on the 3D mode solver. As can be seen, when wavelength shifts ± 5nm away from 1550nm, the attenuation decreases about 1.9 dB/μm. Within 120nm, the modulation depth changes 0.23 dB, from 3.82 dB to 3.59 dB. Thus, this EO modulator also allows for over a terahertz bandwidth. The calculation was also further verified by 3D FDTD modeling. At $\mu_c = 0$, the overall throughput is 81% for both 1545nm and 1555nm; at $\mu_c = 0.518$ eV, the overall throughput is 37.84% and 37.58%, for 1545nm and 1555nm, respectively.

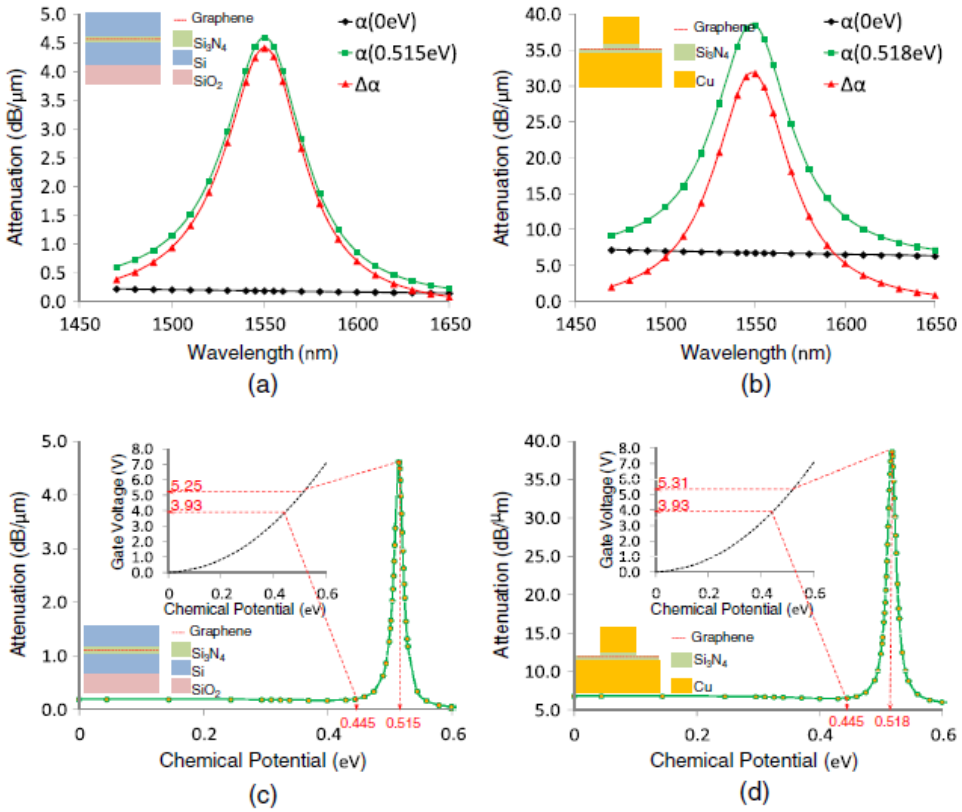

Figure 8.5 The attenuation of graphene-slot modulators as a function of working wavelength at $\mu_c = 0$ and $\mu_c = \mu_t$, respectively: (a) in a silicon waveguide; (b) in a metal strip waveguide. The attenuation of graphene-slot waveguides as a function of chemical potential and gate voltage at a wavelength of 1550nm; (c) in a silicon waveguide (450nm wide and 150nm thick for each layer); (d) in a metal strip plasmonic waveguide (strip metal is 200nm wide). [222]

8.4.3 Power consumption, modulation speed and thermal effect

The modulator footprint mostly comes from the electrical contacts and the overall footprint can be made about 2–3μm^2 with the corresponding capacitance ~0.02 pF (the dielectric constant of Si_3N_4 is assumed to be 7.5). Note the magnitude of graphene dielectric constant is nearly stable between 0 and 0.4 eV, as shown in Fig. 8.1(d). More accurately, significant output power decrease only occurs when the chemical potential varies from 0.445 eV to 0.515 eV, as shown in Figs. 8.5(c) and 8.5(d). When projecting the chemical potential to gate voltage across a 10nm Si_3N_4 buffer layer, the gate voltage change ΔV = (3.93−5.25) V. Thus, each bit only requires 0.12–0.13 pJ. Employment of doped graphene and a high-k (e.g., HfO_2) buffer layer can further decrease the

power consumption.

The proposed modulators can potentially work at an ultrahigh speed. Graphene has outstanding carrier mobility. In addition, intraband transition is much faster than interband transition [288]. The operation speed is mainly limited by the RC delay imposed by electric circuits. The submicrometer wide graphene may result in a very large resistance. Direct graphene–semiconductor contact may resolve this issue, as shown in Figs. 8.6(a) and 8.6(b), and the RC delay can potentially decrease to several picoseconds.

The thermal transport in the modulators was also considered. Although graphene has a superior thermal conductivity, most heat still transfers through the buffer layers. In this case, we treat graphene as a thermal source. Assume the photonic signal power P = 1 mW (which is huge for telecommunications) and half is absorbed by graphene. Silicon nitride has a thermal conductivity k = 29 W/mK. When applying the heat flux $\frac{P}{A} = \frac{0.5\ mW}{0.8\ \mu m \times 0.45 \mu m}$ in the silicon waveguide-based modulator, the resulting temperature gradient in the Si_3N_4 buffer layer will be ~0.048 ℃/nm. The 10nm buffer layer only results in temperature rise, 0.48 ℃.

All the theoretical analysis and numerical modeling in the preceding text are based on the small optical signal assumption, i.e., the change of the graphene conductivity due to the absorption of light is negligible. Because of the extremely enhanced light absorption, saturable absorption and other nonlinear effects may become obvious when the signal power increases to some level. Actually, this nonlinear effect will become obvious when the pump signal is not so strong. According to our calculation, bias voltage V_D = 5.3 V will result in μ_c = 0.518 eV across a 10nm Si_3N_4 buffer layer with $N_s = 2.2 \times 10^{13} cm^{-2}$. Absorption of light will give rise to excess carriers, which can be estimated by pump rate $R = \frac{P}{h\upsilon A}$ and carrier lifetime τ (~0.135 ps for graphene), i.e.,

$\Delta N_s = \frac{P}{h\upsilon A}\tau$. For the modulator simulated in Figs. 8.3(d)–8.3(f), P = 1 mW pump will result in $\Delta N_s = 4.4\times10^{12}$ cm^{-2} $\approx 0.20N_s$. Therefore, the modulator also provides us opportunities to study nonlinear optical effects at a low power level. One important application is all-optic modulators, where one weak optical signal (λ_s) may be switched on/off by another strong optical pump (λ_p) based on the graphene-slot plasmonic waveguide, where a DC bias voltage results in the maximum absorption of λ_p.

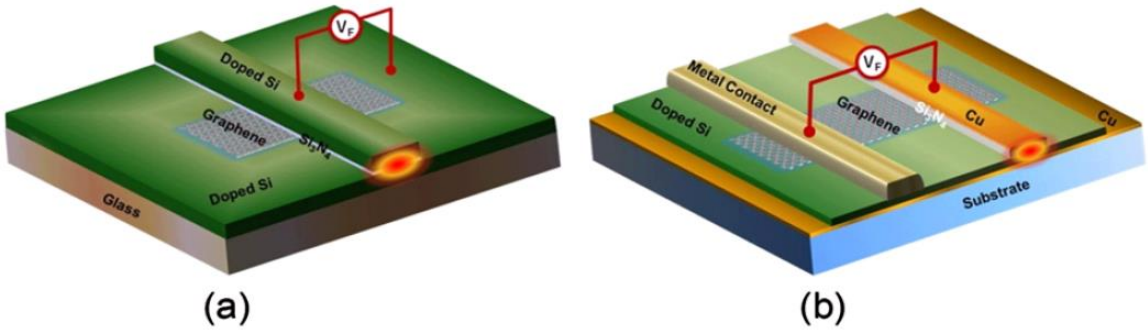

Figure 8.6 The illustration of nanoscale graphene modulators containing direct graphene-semiconductor contacts based on (a) dielectric strip waveguide, and (b) metal strip waveguide. [222]

8.5 Conclusions

To summarize, we studied the optical conductivity and dielectric constant of graphene under different chemical potentials in the near-infrared regime. Because of the effect of intraband absorption, the magnitude of graphene dielectric constant (and hence the attenuation of a graphene-slot waveguide) can be dynamically tuned in a large range by electrical gating. We proposed and modeled a series of graphene EO modulators based on graphene-slot waveguides. Nanoscale graphene EO modulators can be developed based on both silicon and plasmonic platforms. These modulators promise to remove the technical bottleneck in on-chip optical interconnects with the advantages of nanoscale footprints, small insertion loss, low power consumption, and potential ultrahigh speed, as well as being CMOS-compatible.

9 CONCLUSIONS

In this dissertation, several different types of novel metamaterials have been investigated and explored analytically, numerically and experimentally for the applications of subwavelength waveguiding, imaging and modulation. The novel metamaterials studied are not limited to man-made structures, also included naturally existing materials, for example, graphene and TCOs, which have been proven to have superior properties at some specific spectral regimes. The research topics covered in this dissertation concentrated on improving the performance of the devices by taking the advantages of the metamaterials, such as minimizing the footprints of optical modulators to be on nanometer-scale, enhancing resolution of an imaging system that is beyond the diffraction limit, etc.

9.1 Designer surface plasmonics (DSP) and indefinite metamaterials

Chapter 2 and 3 explored the possibility of achieving deep subwavelength imaging via metamaterials with periodic structures. Chapter 2 focused on the experimental demonstration at microwave frequency, which is mimicking surface plasmons with structured metal surfaces. The spacing and the size of the grooves can be readily controlled on scales in GHz and even to THz regime, which enables to engineer a surface plasmon at almost any arbitrary frequency (as long as metals could be treated as nearly perfect conductors). Chapter 3 examined optical properties of a metamaterial consisting of alternating thin layers of metal and dielectric. A slab of this metamaterial can form images with subwavelength sizes, at some specific positions related to the frequency of interest. Two factors will affect the quality of the image formed: the absorption of the materials in the alternating layered structure and the finite thickness of the layers. The combination of the subwavelength imaging with the fact that at specific positions to achieve the

images suggested this layered metamaterial may have very useful applications, for example, enhancing the resolution of lithography.

Both works presented in Chapter 2 and 3 are governed by the effective medium theory (EMT), where the metamaterials can be modeled as homogeneous media. This effective medium is a helpful simplification in terms of understanding and simulating, especially in simulations only macroscopic parameters – permittivity tensors, need to be considered. This theory requires the periodicity of the metamaterials to be much smaller than the wavelength, so the incident radiation cannot resolve the individual feature.

The work in Chapter 2 is the first time microwave near-field microscopy has been used to study designer surface plasmons experimentally. The super Talbot effect shown in Chapter 3 is based upon bulk plasmon without diffraction limit, unlike the plasmon Talbot effect discussed in other works.

9.2 Tunable metamaterials

The work presented in Chapter 4 – Chapter 8 concentrated on the tunable metamaterials and their applications in active devices. All the metamaterials – gallium, ITO and graphene – are naturally existing materials, unlike the artificially designed man-made counterparts proposed in Chapter 2 and 3. The dielectric constants of these materials will be significantly different under some specific conditions, for example, shining light or applying external voltages. Besides the extraordinary properties of the materials themselves, novel waveguide structures also play key roles to achieve the promising results. For example, in Chapter 4, the metal-dielectric-metal plasmonic structure provides a restrictive geometry that allows the surface-mediated effect of gallium to happen, which induces the phase transition of the metal and hence the modulation phenomenon can be observed when external stimulus is applied on the waveguide. In Chapter 6

and 8, a slot-waveguide structure is employed, where the sandwiched thin slot can further enhance the absorption of either ITO or graphene, which paves the way for achieving nanoscale EO modulators.

In Chapter 5 and 7, transfer matrix method (TMM) and Kretchmann ATR experimental setup have been used to explore the modulation effect based on ITO in a planar multilayer structure and the enhanced absorption of monolayer graphene, respectively. In the ITO-based planar modulators presented in Chapter 5, a new material – electrolyte gel is used to form electric double layer at the interface with ITO, where the strong electric field attracts more carriers in ITO to get larger modulation depth. Comparing the modulation depth of ~9% with traditional dielectric (SiO_2, Al_2O_3, etc.), up to 38.8% of the modulation depth can be achieved with electrolyte gel. **The fundamental study of the optical property of monolayer graphene, which is presented in Chapter 7, has shown that greatly enhanced light absorption up to 42.7% could be achieved over a broad spectral range.** This promising result is observed based on a simple ATR setup, without any further process, like patterning or integrating graphene to other devices.

9.3 Future work

The work presented in the dissertation is concentrated on the three important applications of metamaterials: subwavelength waveguiding, imaging and modulation. There is certainly a huge scope for further development on several aspects of the work. Below are some directions which could be followed up:

1. Graphene photodetector, which may be one of the potential applications of the significantly enhanced absorption by graphene presented in Chapter 7. The wavelength-independent absorption enables graphene to be used for a wide spectral range from ultraviolet to infrared.

Another advantage of graphene is its high operating bandwidth, which makes it suitable for high speed data communication. There are several ways to improve the sensitivity of graphene-based photodetectors, for example, integrating it with a waveguide to increase the light – graphene interaction, or using plasmonic nanostructures to enhance the local electric field.

2. Graphene solar cells. The supreme properties of graphene makes it fulfill multiple functions in photovoltaic devices: 1) transparent conductor window, 2) photoactive material, 3) channel for charge transport, and 4) catalyst. Plasmonic structures can be integrated to the graphene solar cells, combing with the significant light absorption by graphene, the efficiency of the photovoltaic devices can be further improved.

3. ITO-based multilayer modulators with high-*k* material. In Chapter 5, a modulation depth up to 38.8% was experimentally demonstrated when electrolyte gel was used in the planar waveguide. In the fabrication process of the modulator, the electrolyte gel was manually applied to the structure. A new material with a comparable or even higher dielectric constant as well as CMOS-compatible is desirable. Ferroelectronic $BaTiO_3$ (BTO) may be a good candidate to replace the electrolyte gel, due to its high refractive index ($n_o \approx 2.224 \pm 0.001$ and $n_e \approx 2.219 \pm 0.001$ at 1539nm [289]), which can be grown by RF sputtering process.

10 PUBLICATIONS

10.A Peer reviewed journals:

1. **W. Zhao**, K. Shi, and Z. Lu, "Greatly Enhanced Ultrabroad Band Light Absorption by Monolayer Graphene," *Opt. Lett.* **38,** 4342(2013).
2. Z. Lu, and **W. Zhao**, "Nanoscale electro-optic modulators based on graphene-slot waveguides," *J. Opt. Soc. Am. B* **29**, 1490(2012).
3. Z. Lu, **W. Zhao**, and K. Shi, "Ultracompact electro-absorption modulators based on tunable epsilon-near-zero-slot waveguides," *IEEE Photonics Journal* **4,** 735(2012).
4. **W. Zhao**, and Z. Lu, "Nanoplasmonic optical switch based on Ga-Si3N4-Ga waveguide," *Opt. Eng.* **50**, 074002(2011).
5. **W. Zhao**, X. Huang, and Z. Lu, "Super Talbot effect in indefinite metamaterial," *Opt. Exp.* **19**, 15297(2011).
6. **W. Zhao**, O. M. Eldaiki, R. Yang, and Z. Lu, "Deep subwavelength waveguiding and focusing based on designer surface plasmons," *Opt. Exp.* **18,** 21498(2010).
7. **W. Zhao**, and Z. Lu, "Negative Refraction Imaging by Three-Dimensional Metamaterial at Microwave Frequencies," *Microw. Opt. Technol. Lett.* **52,** 2253(2010).

10.B Conferences:

1. **W. Zhao**, and Zhaolin Lu, "Transparent Conducting Oxides Based Nanoscale Electro-Optic Modulators," *Frontiers in Optics/Laser Science XXVIII (FiO/LS),* 2012.

2. **W. Zhao**, X. Huang, and Z. Lu, "Demonstration of self-imaging effect without paraxial approximation," *Proceedings of SPIE* Vol. 8269, 82692B, 2012.

3. **W. Zhao**, and Zhaolin Lu, “Applications of Transparent Conducting Oxides in Plasmonic/Optical Modulators,” *ICPEPA-8*, 2012.

4. R. Yang, **W. Zhao**, R. A. Soref, and Z. Lu, "Semiconductor-coated deep subwavelength spoof surface plasmonic waveguide for THz and MIR applications," *Proceedings of SPIE* Vol. 7938, 79380A, 2011.

5. **W. Zhao**, O. M. Eldaiki, R. Yang, and Z. Lu, "Experimental demonstration of linear deep subwavelength spoof surface plasmonic waveguides," *Proceedings of SPIE* Vol. 7946, 794620, 2011.

6. **W. Zhao**, X. Huang, Z. Lu, "Demonstration of super self-imaging in indefinite anisotropic metamaterial," *Proceedings of SPIE* Vol. 8093, 80932J, 2011.

7. R. Yang, **W. Zhao**, and Z. Lu, “Silicon-Coated Deep Subwavelength Spoof Plasmonic Waveguides for THz Applications,” *Frontiers in Optics*, 2010.

8. E. M. Omar, **W. Zhao**, R. Yang, and Z. Lu, “Experimental Demonstration of Deep Subwavelength Waveguiding Based on Designer Surface Plasmons,” *Frontiers in Optics*, 2010.

11 REFERENCES

1. J. B. Pendry, D. Schurig, and D. R. Smith, “Controlling Electromagnetic Fields,” *Science* **312**, 1780(2006).

2. R. Liu, C. Ji, J. J. Mock, J. Y. Chin, T. J. Cui, and D. R. Smith, “Broadband Ground-Plane Cloak,” *Science* **323**, 366(2009).

3. T. Ergin, N. Stenger, P. Brenner, J. B. Pendry, M. Wegener, “Three-Dimensional Invisibility Cloak at Optical Wavelengths,” *Science* **328**, 337(2010).

4. J. B. Pendry, "Negative Refraction Makes a Perfect Lens," *Phys. Rev. Lett.* **85**, 3966(2000).

5. N. Fang, H. Lee, C. Sun, and X. Zhang, “Sub-Diffraction-Limited Optical Imaging with a Silver Superlens,” *Science* **308**, 534(2005).

6. A. Grbic and G. V. Eleftheriades, “Overcoming the Diffraction Limit with a Planar Left-Handed Transmission-Line Lens,” *Phys. Rev. Lett.* **92**, 117403(2004).

7. T. Taubner, D. Korobkin, Y. Urzhumov, G. Shvets, R. Hillenbrand, “Near-Field Microscopy Through a SiC Superlens,” *Science* **313**, 1595(2006).

8. Metamaterial. http://en.wikipedia.org/wiki/Metamaerial

9. Z. Lu, J. A. Murakowski, C. A. Schuetz, S. Shi, G. J. Schneider, and D. W. Prather, “Three-dimensional subwavelength imaging by a photonic-crystal flat lens using negative refraction at microwave frequencies,” *Phys. Rev. Lett.* **95**, 153901(2005).

10. V. Veselago, “The electrodynamics of substances with simultaneously negative values of ε and μ,” *Sov. Phys. USPEKHI.* **10**, 509(1968).

11. J. B. Pendry, A. J. Holden, W. J. Stewart, and I. Youngs, "Extremely low frequency plasmons in metallic mesostructures," *Phys. Rev. Lett.* **76**, 4773(1996).

12. J. B. Pendry, A. J. Holden, D. J. Robbins, and W. J. Stewart, “Magnetism from Conductors and Enhanced Nonlinear Phenomena,” *IEEE Trans. Microwave Theory Tech.* **47**, 2075(1999).

13. N. Liu, H. C. Guo, L. W. Fu, S. Kaiser, H. Schweizer, and H. Giessen, “Three-dimensional photonic metamaterials at optical frequencies,” *Nat. Mater.* **7**, 31(2008).

14. D. R. Smith, J. B. Pendry, and M. C. K. Wiltshire, "Metamaterials and Negative Refractive Index," *Science* **305**, 788(2004).

15. R. A. Shelby, D. R. Smith, and S. Schultz, “Experimental verification of a negative index of refraction,” *Science* **292**, 77-79(2001).

16. H. Chen, W. J. Padilla, J. M. O. Zide, A. C. Gossard, A. J. Taylor, and R. D. Averitt, “Active terahertz metamaterial devices,” *Nature* **444**, 597(2006).

17. H. Tao, A. C. Strikwerda, M. Liu, J. P. Mondia, E. Ekmekci, K. Fan, D. L. Kaplan, W. J. Padilla, X. Zhang, R. D. Averitt, and F. G. Omenetto, “Performance enhancement of terahertz metamaterials on ultrathin substrates for sensing applications,” *Appl. Phys. Lett.* **97**, 261909(2010).

18. W. Chen, A. Totachawattana, K. Fan, J. L. Ponsetto, A. C. Strikwerda, X. Zhang, R. D. Averitt, and W. J. Padilla, “Single-layer terahertz metmaterials with bulk optical constants,” *Phys. Rev. B* **85**, 035112(2012).

19. Y. Gao, J. P. Huang, Y. M. Liu, L. Gao, K. W. Yu, and X. Zhang, “Optical Negative Refraction in Ferrofluids with Magnetocontrollability,” *Phys. Rev. Lett.* **104**, 034501(2010).

20. J. Valentine, S. Zhang, T. Zentgraf, E. Ulin-Avila, D. A. Genov, G. Bartal, and X. Zhang, “Three-dimensional optical metamaterial with a negative refractive index,” *Nature* **455**, 376(2008).

21. A. Degiron, J. J. Mock, and D. R. Smith, “Modulating and tuning the response of metamaterials at the unit cell level,” *Opt. Express* **15**, 1115(2007).

22. D. J. Cho, W. Wu, E. Ponizovskaya, P. Chaturvedi, A. M. Bratkovsky, S. Wang, X. Zhang, F. Wang, and Y. R. Shen, “Ultrafast modulation of optical metamaterials,” *Opt. Express* **17**, 17652(2009).

23. M. A. Noginov, L. Gu, J. Livenere, G. Zhu, A. K. Pradhan, R. Mundle, M. Bahoura, Y. A. Barnakov, and V. A. Podolskiy, "Transparent conductive oxides: Plasmonic materials for telecom wavelengths," *Appl. Phys. Lett.* **99**, 021101(2011).

24. E. Feigenbaum, K. Diest, and H. A. Atwater, "Unity-Order Index Change in Tranparent Conducting Oxides at Visible Frequencies," *Nano Lett.***10**, 2111(2010).

25. G. V. Naik, J. Kim, and A. Boltasseva, “Oxides and nitrides as alternative plasmonic materials in the optical range,” *Opt. Mat. Express* **1**, 1090(2011).

26. D. R. Smith, and D. Schurig, “Electromagnetic Wave Propagation in Media with Indefinite Permittivity and Permeability Tensors,” *Phys. Rev. Lett.* **90**, 077405(2003).

27. X. Zhang, and Z. Liu, "Superlenses to overcome the diffraction limit," *Nature* **7**, 435(2008).

28. W. Cai, D. A. Genov, and V. M. Shalaev, “Superlens based on metal-dielectric composites,” *Phys. Rev. B: Condens. Matter* **72**, 193101(2005).

29. R. Nielsen, M. Thoreson, W. Chen, A. Kristensen, J. Hvam, V. Shalaev, and A. Boltasseva, "Toward superlensing with metal-dielectric composites and multilayers, " *Appl. Phys. B: Lasers and Optics* **100**, 93(2010).

30. P. A. Belov, and Y. Hao, "Subwavelength imaging at optical frequencies using a transmission device formed by a periodic layered metal-dielectric structure operating in the canalization regime," *Phys. Rev. B: Condens. Matter* **73**, 113110(2006).

31. K. J. Webb and M. Yang, "Subwavelength imaging with a multilayer silver film structure," *Opt. Lett.* **31**, 2130(2006).

32. Y. Xiong, Z. Liu, and X. Zhang, "Two-Dimensional Imaging by Far-Field Superlens at Visible Wavelengths," *Appl. Phys. Lett.* **93**, 111116(2008).

33. C. H. Gan and P. Lalanne, "Well-confined surface plasmon polaritons for sensing applications in the near-infrared," *Opt. Lett.* **35**, 610(2010).

34. A. Fang, T. Koschny, and C. M. Soukoulis, "Optical anisotropic metamaterials: Negative refraction and focusing," *Phys. Rev. B* **79**, 245127(2009).

35. B. Wood, J. B. Pendry, and D. P. Tsai, "Directed subwavelength imaging using a layered metal-dielectric systems," *Phys. Rev. B* **74**, 115116(2006).

36. M. G. Silveirinha, P. A. Belov, and C. R. Simovski, "Subwavelength imaging at infrared frequencies using an array of metallic nanorods," *Phys. Rev. B* **75**, 035108(2007).

37. Y. Liu, G. Bartal, and X. Zhang, "All-angle negative refraction and imaging in a bulk medium made of metallic nanowires in the visible region," *Opt. Express* **16**, 15439(2008).

38. D. Bergman, "The dielectric constant of a composite material—A problem in classical physics," *Phys. Rep.* **43**, 377(1978).

39. E. D. Palik, *Handbook of Optical Constants of Solids* (Academic Press, London, 1985).

40. Plasmonic Metamaterials. http://en.wikipedia.org/wiki/Plasmonic_metamaterials

41. H. Atwater, "The promise of PLASMONICS," *A. Sci. Am.* **296**, 56(2007).

42. W. L. Barnes, A. Dereux, and T. W. Ebbesen, "Surface plasmon subwavelength optics," *Nature* **424**, 824-830(2003).

43. G. Goubau, "Surface Waves and Their Application to Transmission Lines," *J. Appl. Phys.* **21**, 1119(1950).

44. J. R. Krenn, A. Dereus, J. C. Weeber, E. Bourillot, Y. Lacroute, J. P. Goudonnet, G. Schider, W. Gotschy, A. Leitner, F. R. Aussenegg, and C. Girard, "Squeezing the Optical Near-

Field Zone by Plasmon Coupling of Metallic Nanoparticles," *Phys. Rev. Lett.* **82**, 2590(1999).

45. L. Yin, V. K. Vlasko-Vlasov, J. Pearson, J. M. Hiller, J. Hua, U. Welp, D. E. Brown, and C. W. Kimball, "Subwavelength focusing and guiding of surface plasmons," *Nano Lett.* **5**, 1399(2005).

46. S. I. Bozhevolnyi, V. S. Volkov, E. Devaus, and T. W. Ebbesen, "Channel plasmon-polariton guiding by subwavelength metal grooves," *Phys. Rev. Lett.* **95**, 046802(2005).

47. D. M. Koller, A. Hohenau, H. Ditlbacher, N. Galler, F. Reil, F. R. Aussenegg, A. Leitner, E. J. W. List, and J. R. Krenn, "Organic plasmon-emitting diode," *Nat. Photonics* **2**, 684(2008).

48. S. I. Bozhevolnyi, V. S. Volkov, E. Devaux, J. Y. Laluet, and T. W. Ebbesen, "Channel plasmon subwavelngth waveguide components including interferometers and ring resonators," *Nature* **440**,508(2006).

49. L. Tang, S. E. Kocabas, S. Latif, A. K. Okyay, D. Ly-Gagnon, K. C. Saraswat, and D. A. B. Miller, "Nanometre-scale germanium photodetector enhanced by a nearinfrared dipole antenna," *Nat. Photonics* **2**, 226(2008).

50. E. Berhagen, M. Spasenovic, A. Polman, and L. K. Kuipers, "Nanowire plasmon excitation by adiabatic mode transformation," *Phys. Rev. Lett.* **102**, 203904(2009).

51. F. De Angelis, G. Das, P. Candeloro, M. Patrini, M. Galli, A. Bek, M. Lazzarino, I. Maksymov, C. Liberale, L. C. Andreani, and E. Di Fabrizio, "Nanoscale chemical mapping using three-dimensional adiabatic compression of surface plasmon polaritons," *Nat. Nanotechnol.* **5**, 67(2010).

52. D. L. Mills, and A. A. Maradudin, "Surface corrugation and surface-polariton binding in the infrared frequency range," *Phys. Rev. B. Condens. Matter* **39**, 1569(1989).

53. F. J. Garcia-Vidal, L. Martín-Moreno, and J. B. Pendry, "Surfaces with holes in them: new plasmonic metamaterials," *J. Opt. A, Pure Appl. Opt.* **7**, S97(2005).

54. J. B. Pendry, L. Martín-Moreno, and F. J. Garcia-Vidal, "Mimicking Surface Plasmons with Structured Surfaces," *Science* **305**, 847(2004).

55. F. J. de Abajo, and J. J. Sáenz, "Electromagnetic surface modes in structured perfect-conductor surfaces," *Phys.Rev. Lett.* **95**, 233901(2005).

56. A. P. Hibbins, B. R. Evans, and J. R. Sambles, "Experimental verification of designer surface plasmons," *Science* **308**, 670(2006).

57. C. R. Williams, S. R. Andrews, S. A. Maier, A. I. Fernández-Dominguez, L. Martín-Moreno, and F. J. García-Vidal, "Highly confined guiding of terahertz surface plasmon polariton on structured metal surfaces," *Nat. Photonics* **2**, 175(2008).

58. W. Zhu, A. Agrawal, and A. Nahata, "Planar plasmonic terahertz guided-wave devices," *Opt. Express* **16**, 6126(2008).

59. S. A. Maier, S. R. Andrews, L. Martín-Moreno, and F. J. García-Vidal, "Terahertz surface plasmon-polariton propagation and focusing on periodically corrugated metal wires," *Phys. Rev. Lett.* **97**, 176805(2006).

60. A. I. Fernández-Dominguez, E. Moreno, L. Martín-Moreno, and F. J. García-Vidal, "Guiding terahertz waves along subwavelength channels," *Phys. Rev. B.* **79**, 233104(2009).

61. A. I. Fernández-Dominguez, E. Moreno, L. Martín-Moreno, and F. J. García-Vidal, "Terahertz wedge plasmon polaritons," *Opt. Lett.* **34**, 2063(2009).

62. M. L. Nesterov, D. Martin-Cano, A. I. Fernández-Dominguez, E. Moreno, and F. J. García-Vidal, "Geometrically induced modification of surface plasmons in the optical and telecom regimes," *Opt. Lett.* **35**, 423(2010).

63. D. Martin-Cano, M. L. Nesterov, A. I. Fernández-Dominguez, F. J. García-Vidal, L. Martín-Moreno, and E. Moreno, "Domino plasmons for subwavelength terahertz circuitry," *Opt. Express* **18**, 754(2010).

64. K. S. Novoselov, V. I. Fal'ko, L. Colombo, P. R. Gellert, M. G. Schwab, and K. Kim, "A roadmap for graphene," *Nature* **490**, 7419(2012).

65. P. Blake, P. D. Brimicombe, R. R. Nair, T. J. Booth, D. Jiang, F. Schedin, L. A. Ponomarenko, S. V. Morozov, H. F. Gleeson, E. W. Hill, A. K. Geim, and K. S. Novoselov, "Graphene-Based Liquid Crystal Device," *Nano Lett.* **8**, 1704-1708(2008).

66. Y. Hernandez, V Nicolosi, M. Lotya, F. M. Blighe, Z. Sun, S. De, I. T. McGovern, B. Holland, M. Byrne, Y. K. Gun'Ko, J. J. Boland, P. Niraj, G. Duesberg, S. Krishnamurthy, R. Goohhue, J. Hutchison, V. Scardaci, A. C. Ferrari, and J. N. Coleman, "High-yield production of graphene by liquid-phase exfoliation of graphite," *Nat. Nanotech.* **3**, 563-568(2008).

67. H. C. Schniepp, J. Li, M. J. McAllister, H. Sai, M. Herrera-Alonso, D. H. Adamson, R. K. Prud'homme, R. Car, D. A. Saville, and I. A. Aksay, "Functionalized Single Graphene Sheets Derived from Splitting Graphite Oxide," *J. Phys. Chem. B* **110**, 8535-8539(2006).

68. A. Reina, X. Jia, J. Ho, D. Nezich, H. Son, V. Bulovic, M. S. Dresselhaus, and J. Kong, "Large Area, Few-Layer Graphene Films on Arbitrary Substrates by Chemical Vapor Deposition," *Nano Lett.* **9**, 30-35(2009).

69. S. Amini, J. Garay, G. Liu, A. A. Balandin, and R. Abbaschian, "Growth of large-area graphene films from metal-carbon melts," *J. Appl. Phys.* **108**, 094321(2010).

70. S. Mikhailov, K. Ziegler, "New Electromagnetic Mode in Graphene," *Phys. Rev. Lett.* **99**, 016803(2007).

71. M. Jablan, H. Buljan, M. Soljačić, “Plasmonics in Graphene at Infrared Frequencies,” *Phys. Rev. B* **80**, 245435(2009).

72. F. H. L. Koppens, D. E. Chang, F. J. Garc á de Abajo, “Graphene Plasmonics: A Platform for Strong Light-Matter Interactions,” *Nano Lett.* **11**, 3370-3377(2011).

73. G. W. Hanson, “Dyadic Green’s Functions and Guided Surface Waves for a Surface Conductivity Model of Graphene,” *J. Appl. Phys.* **103**, 064302(2008).

74. A. Y. Nikitin, F. Guinea, F. Garc á-Vidal, L. Mart ń-Moreno, “Edge and Waveguide Terahertz Surface Plasmon Modes in Graphene Microribbons,” *Phys. Rev. B* **84**, 161407(2011).

75. L. Ju, B. Geng, J. Horng, C. Girit, M. Martin, Z. Hao, H. A. Bechtel, X. Liang, A. Zettl, Y. R. Shen, and F. Wang, “Graphene Plasmonics for Tunable Terahertz Metamaterials,” *Nat. Nanotechnol.* **6**, 630-634(2011).

76. A. Vakil, N. Engheta, “Transformation Optics Using Graphene,” *Science* **332**, 1291-1294(2011).

77. V. P. Gusynin, S. G. Sharapov, and J. P. Carbotte, “Magneto-optical conductivity in graphene,” *J. Phys. Conens. Matter* **19**, 026222(2007).

78. D. R. Andersen, “Graphene-based long-wave infrared TM surface plasmon modulator,” *J. Opt. Soc. Am. B* **27**, 818-823(2010).

79. M. Liu, X. B. Yin, E. Ulin-Avila, B. S. Geng, T. Zentgraf, L. Ju, F. Wang, and X. Zhang, "A graphene-based broadband optical modulator," *Nature* **474**, 64(2011).

80. M. Liu, X. Yin, X. Zhang, “Double-Layer Graphene Optical Modulator,” *Nano Lett.* **12**, 1482-1485(2012).

81. G. Reed, G. Mashanovich, F. Gardes, D. Thomson, “Silicon Optical Modulators,” *Nat. Photonics* **4**, 518-526(2010).

82. J. Liu, M. Beals, A. Pomerene, S. Bemardis, R. Sun, J. Cheng, L. C. Kimerling, and J. Michel, “Waveguide-Integrated, Ultralow-Energy Gesi Electro-absorption Modulators,” *Nat. Photonics* **2**, 433-437(2008).

83. Transparent conducting oxides, http://en.wikipedia.org/wiki/Transparent_conducting_oxide#Transparent_conducting_oxides

84. N. Liu, L. W. Fu, H. C. Guo, S. Kaiser, H. Schweizer, H. Giessen, “Three-dimensional metamaterials at opical frequencies,” *Lasers and Electro-Optics, 2008 and 2008*

Conference on Quantum Electronics and Laser Science. CLEO/QELS 2008. Conference on, vol., no., pp. 1,2, 4-9 May 2008

85. W. Zhao, O. M. Eldaiki, R. Yang, and Z. Lu, "Deep subwavelength waveguiding and focusing based on designer surface plasmons," *Opt. Exp.* **18**, 21498(2010).

86. W. Zhao, and Z. Lu, "Negative Refraction Imaging by Three-Dimensional Metamaterial at Microwave Frequencies," *Microw. Opt. Technol. Lett.* **52**, 2253(2010).

87. D. Schurig, J. J. Mock, B. J. Justice, S. A. Cummer, J. B. Pendry, A. F. Starr, and D. R. Smith, "Metamaterial Electromagnetic Cloak at Microwave Frequency," *Science* **314**, 977(2006).

88. H-T Chen, H. Yang, R. J. Singh, J. F. O'Hara, A. K. Azad, S. A. Trugman, Q. X. Jia, and A. J. Taylor, "Tuning the Resonance in High-Temperature Superconducting Terahertz Metamaterials," *Phys. Rev. Lett.* **105**, 247402(2010).

89. K. S. Novoselov, D. Jiang, F. Schedin, T. J. Booth, V. V. Khotkevich, S. V. Morozov, and A. K. Geim, "Two-dimensional atomic crystals," *PNAS* **102**, 10451(2005).

90. Y. Lee, S. Bae, H. Jang, S. Jang, S. Zhu, S. Sim, Y. Song, B. Hong, and J. Ahn, "Wafer-Scale Synthesis and Transfer of Graphene Films," *Nano Lett.* **10**, 490-493(2010).

91. Q. Yu, J. Lian, S. Siriponglert, H. Li, Y. Chen, and S. Pei, "Graphene segregated on Ni surfaces and transferred to insulators," *Appl. Phys. Lett.* **93**, 113103(2008).

92. X. Li, W. Cai, J. An, S. Kim, J. Nah, D. Yang, R. Piner, A. Velarmakanni, I. Jung, E. Tutuc, S. K. Banerjee, L. Colombo, R. S. Ruoff, "Large-Area Synthesis of High-Quality and Uniform Graphene Films on Copper Foils," *Science* **324**, 1312-1314(2009).

93. A. N. Obraztsov, E. A. Obraztsova, A. V. Tyurnina, A. A. Zolotukhin, "Chemical vapor deposition of thin graphite films of nanometer thickness," *Carbon* **45**, 2017-2021(2007).

94. P. Sutter, "How silicon leaves the scene," *Nature Mat.* **8**, 171-172(2009).

95. J. Robinson, X. Weng, K. Trumbull, R. Cavalero, M. Wetherington, E. Frantz, M. Labella, Z. Hughes, M. Fanton, and D. Snyder, "Nucleation of Epitaxial Graphene on SiC(0001)," *ACS Nano* **4**, 153-158(2010).

96. M. Choucair, P. Thordarson, and J. A. Stride, "Gram-scale production of graphene based on solvothermal synthesis and sonication," *Nature Nanotechnol.* **4**, 30-33(2009).

97. X. Li, X. Wang, L. Zhang, S. Lee, and H. Dai, "Chemically Derived, Ultrasmooth Graphene Nanoribbon Semiconductors," *Science* **319**, 1229-1232(2008).

98. Q. Bao, H. Zhang, B. Wang, Z. Ni, C. Lim, Y. Wang, D. Tang, and K. Loh, "Broadband graphen polarizer," *Nat. Photonics* **5**, 411(2011).

99. X. S. Li, Y. W. Zhu, W. W. Cai, M. Borysiak, B. Y. Han, D. Chen, R. D. Piner, L. Colombo, and R. S. Ruoff, "Transfer of Large-Area Graphene Films for High-Performance Transparent Conductive Electrodes," *Nano Lett.* **9**, 4359(2009).

100. K. S. Kim, Y. Zhao, H. Jang, S. Y. Lee, J. M. Kim, S. S. Kim, J. H. Ahn, P. Kim, J. Y. Choi, and B. H. Hong, "Large-scale pattern growth of graphene films for stretchable transparent electrodes," *Nature* **457**, 706(2009).

101. J. Hodkiewicz, "Characterizing Graphene with Raman Spectroscopy," http://www.thermoscientific.fr/eThermo/CMA/PDFs/Product/productPDF_56769.PDF

102. M. Wall, "Raman Spectroscopy Optimizes Graphene Characterization," http://www.asminternational.org/static/Static%20Files/IP/Magazine/AMP/V170/I04/amp17004p35.pdf?authtoken=c0b38dd8f73c4f89830e6e18410a0e38017076ba

103. I. Hamberg, and C. G. Granqvist, "Evaporated Sn-doped In2O3 films: Basic optical properties and applications to energy-efficient windows," *J. Appl. Phys.* **60**, 123-159(1986).

104. K. Ellmer and R. Mientus, "Carrier transport in polycrystalline ITO and ZnO: Al II: The influence of grain barriers and boundaries," *Thin Soild Films* **516**, 5829-5835(2008).

105. J. M. Zhou, M. S. Thesis "Indium Tin Oxide (ITO) Deposition, Patterning, and Schottky Contact Fabrication," 2005.

106. F. C. Lai, L. M. Lin, R. Q. Gai, Y. Z. Lin, and Z. G. Huang, "Determination of optical constants and thickness of In_2O_3: Sn films from transmittance data," *Thin Solid Films* **515**, 7387-7392(2007).

107. P. R. West, S. Ishii, G. V. Naik, N. K. Emani, V. M. Shalaev, and A. Boltasseva, "Searching for better plasmonic materials," *Laser Photon. Rev.***4**, 795-808(2010).

108. A. Taflove and S. C. Hagness, "Computational Electromagnetics: The Finite-Difference Time-Domain Method," *Artech House*, Norwood (2005).

109. K. S. Yee, "Numerical solution of initial boundary value problems involving Maxwell's equations," *IEEE Trans. Antennas Propag.* **14**, 302-307(1966).

110. Y. Hao and R. Mittra, *FDTD Modeling of Metamaterials.* Artech house, 2009

111. B. Hecht, H. Bielefeldt, L. Novotny, Y. Inouye, and D. W. Pohl, "Local excitation, scattering, and interference of surface plasmons," *Phys. Rev. Lett.* **77**, 1889-1892(1996).

112. S. A. Maier, *Plasmonics: Fundamentals and Applications*, (Springer Verlag, 2007).

113. S. I. Bozhevolnyi, V. S. Volkov, E. Devaux, J. Y. Laluet, and T. W. Ebbesen, "Channel plasmon subwavelength waveguide components including interferometers and ring resonators," *Nature* **440**, 508-511(2006).

114. L. Tang, S. E. Kocabas, S. Latif, A. K. Okyay, D. Ly-Gagnon, K. C. Saraswat, and D. A. B. Miller, "Nanometre-scale germanium photodetector enhanced by a nearinfrare dipole antenna," *Nat. Photonics* **2**, 226-229(2008).

115. C. R. Williams, S. R. Andrews, S. A. Maier, A. I. Fernndez-Domnguez, L. Mart ń-Moreno, and F. J. Garcia-Vidal, "Highly confined guiding of terahertz surface plasmon polaritons on structured metal surfaces," *Nat. Photonics* **2**, 175-179(2008).

116. W. Nomura, M. Ohtsu, and T. Yatsui, "Nanodot coupler with a surface plasmon polariton condenser for optical far/near-field conversion," *Appl. Phys. Lett.* **86**, 181108(2005).

117. Z. Lu, C. Chen, C. A. Schuetz, S. Shi, J. A. Murakowski, G. J. Schneider, and D. W. Prather, "Sub-wavelength imaging by a flat cylindrical lens using optimized negative refraction," *Appl. Phys. Lett.* **87**, 091907(2005).

118. Z. Lu, C. A. Schuetz, S. Shi, C. Chen, G. P. Behrmann, and D. W. Prather, "Experimental demonstration of self-collimation in low index contrast photonic crystals in the millimeter wave regime," *IEEE Trans. Microw. Theory Tech.* **53**, 1362-1368(2005).

119. B. Hecht, H. Bielefeldt, Y. Inouye, D. W. Pohl, and L. Novotny, "Facts and artifacts in near-field optical microscopy," *J. Appl. Phys.* **81**, 2492(1997).

120. R. Yang, W. Zhao, R. A. Soref, and Z. Lu, "Semiconductor-coated deep subwavelength spoof surface plasmonic waveguide for THz and MIR applications," *Proceedings of SPIE*, vol. 7938, no. 1, pp. 79 380A-79 380A-6, Feb. 2011.

121. W. Zhao, X. Huang, and Z. Lu, "Super Talbot effect in indefinite metamaterial," *Opt. Exp.* **19**, 15297(2011).

122. O. Benson, "Assembly of hybrid photonic architectures from nanophotonic constituents," *Nature* **480**, 193-199(2011).

123. H. F. Talbot, "Facts relating to optical science," *Philos. Mag.* **9**, 401-407(1836).

124. L. Rayleigh, "On copying diffraction gratings and on some phenomenon connected therewith," *Philos. Mag.* **11**, 196-205(1881).

125. J. M. Cowley and A. F. Moodie, "Fourier images I. The point source," *Proc. Phys. Soc.* **70**, 486-496(1957).

126. J. M. Cowley and A. F. Moodie, “Fourier images II. The out-of-focus patterns,” *Proc. Phys. Soc.* **70**, 497-504(1957).

127. J. M. Cowley and A. F. Moodie, “Fourier images III. Finite sources,” *Proc. Phys. Soc.* **70**, 505-513(1957).

128. J. M. Cowley and A. F. Moodie, “Fourier images IV. The phase grating,” *Proc. Phys. Soc.* **76**, 378-384(1960).

129. G. L. Rogers, “Interesting paradox in Fourier images,” *J. Opt. Soc. Am.* **62**, 917-918(1972).

130. http://en.wikipedia.org/wiki/Talbot_effect

131. J. W. Goodman, Introduction to Fourier Optics (McGraw-Hill, New York, 1968).

132. D. Mehuys, W. Streifer, R. G. Waarts, and D. F. Welch, “Modal analysis of linear Talbot-cavity semiconductor lasers,” *Opt. Lett.* **16**, 823-825(1991).

133. J. Azaña, “Spectral Talbot phenomena of frequency combs induced by cross-phase modulation in optical fibers,” *Opt. Lett.* **30**, 227-229(2005).

134. K. Patorski, “The self-imaging phenomenon and its applications,” *Prog. Opt.* **27**, 1-108(1989).

135. L. Liu, “Lau cavity and phase locking of laser arrays,” *Opt. Lett.* **14**, 1312-1314(1989).

136. J. M. Cowley, Diffraction Physics (North-Holland, Amsterdam, 1995).

137. M. S. Chapman, C. R. Ekstrom, T. D. Hammond, J. Schmiedmayer, B. E. Tannian, S. Wehinger, and D. E. Pritchard, “Near-field imaging of atom diffraction gratings: the atomic Talbot effect,” *Phys. Rev. A* **51**, R14-R17(1995).

138. R. Iwanow, D. A. May-Arrioja, D. N. Christodoulides, G. I. Stegeman, Y. Min, and W. Sohler, “Discrete Talbot effect in waveguide arrays,” *Phys. Rev. Lett.* **95**, 053902(2005).

139. Y. Wang, K. Zhou, X. Zhang, K. Yang, Y. Wang, Y. Song, and S. Liu, “Discrete plasmonic Talbot effect in subwavelength metal waveguide arrays,” *Opt. Lett.* **35**, 685-687(2010).

140. J. A. Conway, S. Sahni, and T. Szkopek, “Plasmonic interconnects versus conventional interconnects: a comparison of latency, crosstalk and energy costs,” *Opt. Express* **15**, 4474(2007).

141. M. R. Dennis, N. I. Zheludev, and F. Javier Garcia de Abajo, "The plasmon Talbot effect," *Opt. Express* 15, 9692-9700(2007).

142. W. Zhang, C. Zhao, J. Wang, and J. Zhang, "An experimental study of the plasmonic Talbot effect," *Opt. Express* **17**, 19757-19762(2009).

143. J. Winthrop and C. R. Worthington, "Theory of Fresnel images. I. Plane periodic objects in monochromatic light," *J. Opt. Sco. Am.* **55**, 373(1965).281

144. P. A. Belov, Y. Hao, and S. Sudhakaran, "Subwavelength microwave imaging using an array of parallel conducting wires as a lens," *Phys. Rev. B* **73**, 033198(2006)

145. H. Masuda and K. Fukuda, "Ordered metal nanohole arrays made by a two-step replication of honeycomb structures of anodic alumina," *Science* **268**, 1466-1468(1995).

146. H. J. Fan, P. Werner, and M. Zacharias, "Semiconductor nanowires: from self-organization to patterned growth," *Small* **2**, 700-717(2006).

147. S. Rahman and H. Yang, "Nanopillar arrays of glassy carbon by anodic aluminum oxide nanoporous templates," *Nano Lett.* **3**, 439-442(2003).

148. S. Shoji and S. Kawata, "Photofabrication of three-dimensional photonic crystal by multibeam laser interference into a photopolymerizable resin," *Appl. Phys. Lett.* **76**, 2668(2000).

149. N. Zheludev, "Nonlinear optics on the nanoscale," *Contemp. Phys.* **43**, 365-377(2002).

150. W. Zhao, and Z. Lu, "Nanoplasmonic optical switch based on Ga-Si_3N_4-Ga waveguide," *Optical Engineering* **50**, 074002(2011).

151. R. Soref, "The Past, Present, and Future of Silicon Photonics," *IEEE J. Sel. Top. Quantum Electron.* **12**, 1678-1687(2006).

152. B. Jalali, S. Fathpour, "Silicon Photonics," *J. Lightwave Technol.* **24**, 4600-4615(2006).

153. M. Lipson, "Guiding, Modulating, and Emitting Light on Silicon – Challenges and Opportunities," *J. Lightwave Technol.* **23**, 4222-4238(2005).

154. A. V. Krasavin, and N. I. Zheludev, "Active plasmonics: Controlling signals in Au/Ga waveguide using nanoscale structural transformations," *Appl. Phys. Lett.* **84**, 1416(2004).

155. K. F. MacDonald, V. A. Fedotov, and N. I. Zheludev, "Optical nonlinearity resulting from a light-induced structural transition in gallium nanoparticles," *Appl. Phys. Lett.* **82**, 1087(2003).

156. V. A. Fedotov, M. Woodford, I. Jean, and N. I. Zheludev, "Photoconductivity in confined gallium," *Appl. Phys. Lett.* **80**, 1297(2002).

157. L. Bosio, "Crystal structures of Ga(II) and Ga(III)," *J. Chem. Phys.* **68**, 1211-1223(1978).

158. V. Albanis, S. Dhanjal, V. I. Emelyanov, V. A. Fedotov, K. F. MacDonald, P. Petropoulos, D. J. Richardson, and N. I. Zheludev, "Nanosecond dynamics of a gallium mirror's light-induced reflectivity change," *Phys. Rev. B* **63**, 165207(2001).

159. K. MacDonald, V. A. Fedotov, R. W. Eason, N. I. Zheludev, A. V. Rode, B. L.-Davies, and V. I. Emelyanov, "Light-induced metallization in laser-depostied gallium films," *J. opt. Soc. Am. B.* **18**, 331-334(2001).

160. A. Rode, M. Samoc, B. Luther-Davies, E. G. Gamaly, K. F. MacDonald, and N. I. Zheludev, "Dynamics of light-induced reflectivity switching in gallium films deposited on silica by pulsed laser ablation," *Opt. Lett.* **26**, 441(2001).

161. R. Kofman, P. Cheyssac, and J. Richard, "Optical properties of Ga monocrystal in the 0.3-5-ev range," *Phys. Rev. B* **16**, 5216-5244(1977).

162. E. D. Palik, ed., *Handbook of Optical Constants of Solids Academic*, New York (1984).

163. G. Veronis and S. Fan, "Theoretical investigation of compact couplers between dielectric slab waveguides and two-dimensional metal-dielectric-metal plasmonic waveguides," *Opt. Express* **15**, 1211-1221(2007).

164. J. Jin, "The Finite Element Method," in *Electromagnetics*, Wiley, New York, 2002.

165. R. A. Wshsheh, Z. Lu, and M. A. G. Abushagur, "Nanoplasmonic couplers and splitters," *Opt. Express* **17**, 19033(2009).

166. Y. Shen and G. Wang, "Optical bistability in metal gap waveguide nanocavities," *Opt. Express* **16**, 8421-8426(2008).

167. P. Alpuim, L. M. Goncalves, E. S. Marins, T. M. R. Viseu, S. Ferdov, and J. E. Bourée, "Deposition of silicon nitride thin films by hot-wire CVD at 100 ℃ and 250 ℃," *Thin Solid Films* **517**, 3503-3506(2009).

168. A. V. Rode, M. Samoc, B. Luther-Davies, E. G. Gamaly, K. F. MacDonald, and N. I. Zheludev, "Dynamics of light-induced reflectivity switching in gallium films deposited on silica by pulsed laser ablation," *Opt. Lett.* **26**, 441-443(2001).

169. K. F. MacDonald, V. A. Fedotov, S. Pochon, K. J. Ross, G. C. Stevens, N. I. Zheludev, W. S. Brocklesby, and V. I. Emel'yanov, "Optical control of gallium nanoparticle growth," *Appl. Phys. Lett.* **80**, 1643-1645(2002).

170. V. A. Fedotov, K. F. MacDonald, N. I. Zheludev, and V. I. Emel'yanov, "Light-controlled growth of gallium nanoparticles," *J. Appl. Phys.* **93**, 3540-3544(2003).

171. J. Tian, S. Yu, W. Yan, and M. Qiu, "Broadband high-efficiency surface-plasmon-polariton coupler with silicon-metal interface," *Appl. Phy. Lett.* **95**, 013504(2009).

172. Z. Han, A. Elezzabi, and V. Van, "Experimental realization of subwavelength plasmonic slot waveguides on a silicon platform," *Opt. Lett.* **35**, 502-504(2010).

173. H. Lu, X. Liu, L. Wang, Y. Gong, and D. Mao, "Ultrafast all-optical switching in nanoplasmonic waveguide with Kerr nonlinear resonator" *Opt. Express* **19**, 2910-2915(2011).

174. H. Lu, X. Liu, Y. Gong, D. Mao, and L. Wang, "Optical bistability in metal-insulator-metal plasmonic Bragg waveguides with Kerr nonlinear defects," *Appl. Opt.* **50**, 1307-1311(2011).

175. S. A. Maier and H. A. Atwater, "Plasmonics: Localization and guiding of electromagnetic energy in metal/dielectric structures," *J. Appl. Phys.* **98**, 011101(2005).

176. S. A. Maier, P. G. Kik, H. A. Atwater, S. Meltzer, E. Harel, B. E. Koel, and A. A. G. Requicha, "Local detection of electromagnetic energy transport below the diffraction limit in metal nanoparticle plasmon waveguides," *Nat. Mater.* **2**, 229-232(2003).

177. S. I. Bozhevolnyi, V. S. Volkov, E. Devaux, J. Y. Laluet, and T. W. Ebbesen, "Channel plasmon subwavelength waveguide components including interferometers and ring resonantors," *Nature* **440**, 508-511(2006).

178. N. Fang and X. Zhang, "Imaging properties of a metamaterial superlens," *Appl. Phys. Lett.* **82**, 161-163(2003).

179. D. Schurig, J. J. Mock, B. J. Justice, S. A. Cummer, J. B. Pendry, A. F. Starr, and D. R. Smith, "Metamaterial Electromagnetic Cloak at Microwave Frequencies," *Science* **314**, 977-980(2006).

180. U. Leonhardt, "Optical Conformal Mapping," *Science* **312**, 1777-1780(2006).

181. J. B. Pendry, D. Schurig, and D. R. Smith, "Controlling Electromagnetic Fields," *Science* **312**, 1780(2006).

182. A. V. Kildishev and V. M. Shalaev, "Engineering space for light via transformation optics," *Opt. Lett.* **3**, 43-45(2008).

183. D. Schurig, J. B. Pendry, and D. R. Smith, "Transformation-designed optical elements," *Opt. Exp.* **15**, 14772-14782(2007).

184. Y. Xiong, Z. Liu, and X. Zhang, "A simple design of flat hyperlens for lithography and imaging with half-pitch resolution down to 20 nm," *Appl. Phys. Lett.* **94**, 203108(2009).

185. A. N. Sudarkin and P. A. Demkovich, "Excitation of surface electromagnetic waves on the boundary of a metal with an amplifying medium," *Sov. Phys. Tech. Phys.* **34**, 764-766(1989).

186. C. Sirtori, C. Gmachl. F. Capasso, J. Faist, D. L. Sivco, A. L. Hutchinson, and A. Y. Cho, "Long-wavelength ($\lambda \approx$ 8-11.5 μm) semiconductor lasers with waveguides based on surface plasmons," *Opt. Lett.* 23, 1366-1368 (1998).

187. M. P. Nezhad, K. Tetz, and Y. Fainman, "Gain assisted propagation of surface plasmon polaritons on planar metallic waveguides," *Opt. Express* **12**, 4072-4079(2004).

188. K. H. Kim, K. C. Park, and D. Y. Ma, "Structural, electrical and optical properties of aluminum doped zinc oxide films prepared by radio frequency magnetron sputtering," *J. Appl. Phys.* **81**, 7764-7772(1997).

189. A. J. Hoffman, L. Alekseyev, S. S. Howard, K. J. Franz, D. Wasserman, V. A. Podolskiy, E. E. Narimanov, D. L. Sivco, and C. Gmachl, "Negative refraction in semiconductor metamaterials," *Nat. Mater.* **6**, 946-950(2007).

190. P. F. Robusto and R. Braunstein, "Optical Measurements of the Surface Plasmon of Indium-Tin Oxide," *Phys. Stat. Sol. A* **119**, 155-168(1990).

191. M.Y. C. Xu, M. Z. Alam, A. J. Zilkie, K. Zeaiter, and J. S. Aitchison, "," *in: Proceedings of the Conference on Lasers and Electro-Optics/Quantum Electronics and Laser Science Conference, San Jose, CA, USA, 2008, IEEE, pp.* 2135-2136.

192. F. Michelotti, L. Dominici, E. Descrovi, N. Danz, and F. Menchini, "Thickness dependence of surface plasmon polariton dispersion in transparent conducting oxide films at 1.55 μm," *Opt. Lett.* **34**, 839-841(2009).

193. R. G. Gordon, "Criteria for Choosing Transparent Conductors," *MRS Bull.* **25**, 52-57(2000).

194. T. J. Coutts, D. L. Young, and X. Li, "Characterization of Transparent Conducting Oxides," *MRS Bull.* **25**, 58-65(2000).

195. C. Rhodes, S. Franzen, J. Maria, M. Losego, D. N. Leonard, B. Laughlin, G. Duscher, and S. Weibel, "Surface plasmon resonance in conducting metal oxides," *J. Appl. Phys.***100**, 054905(2006).

196. M. A. Noginov, L. Gu, J. Livenere, G. Zhu, A. K. Pradhan, R. Mundle, M. Bahoura, Yu. A. Barnakov, and V. A. Podolskiy, "Transparent conductive oxides: Plamsonic materials for telecom wavelengths," *Appl. Phys. Lett.* **99**, 021101(2011).

197. P. Yeh, A. Yariv, and C. S. Hong, "Electromagnetic propagation in periodic stratified media. I. General theory,"*J. Opt. Soc. Am* **67**, 423-438(1977).

198. B. E. A. Saleh and M. C. Teich, "Fundamentals of Photonitcs, Second Edition," Chapter 7, John Wiley&Sons, Inc., 2007.

199. http://en.wikipedia.org/wiki/Transfer-matrix_method_%28optics%29

200. B. E. A. Saleh and M. C. Teich, "Photonic-Crystal Optics," in *Fundamentals of Photonics*, 2nd ed. Hoboken, NJ: Wiley-Interscience, 2007, pp. 246–253.

201. P. Drude, "Zur Elektronentheorie der metalle," *Annalen der Physik* **306**, 566, 1900.

202. P. Drude, "Zur Elektronentheorie der metalle; II. Teil. Galvanomagnetische und thermomagnetis che Effecte," *Annalen der Physik* **308**, 369, 1900.

203. M. Fox, "Free electrons," in *Optical Properties of Solids*, Oxford University Press, 2001, pp. 154-157.

204. E. Kretschmann, and H. Raether, "Radiative Decay of Non Radiative Surface Plasmons Excited by Light," *Z. Nathurforsch* **23**, 2135-2136(1968).

205. W. Zhao, K. Shi, and Z. Lu, "Greatly Enhanced Ultrabroad Band Light Absorption by Monolayer Graphene," *Opt. Lett.* **38**, 4342-4345(2013).

206. D. Nilsson, N. Robinson, M. Berggren, and R. Forchheimer, "Electrochemical Logic Circuits," *Adv. Mater.* **17**, 353-358(2005).

207. C. Lu, Q. Fu, S. Huang, and J. Liu, "Polymer Electrolyte-Gated Carbon Nanotube Field-Effect Transistor," *Nano Lett.* **4**, 623-627(2004).

208. X. Gan, R. Shiue, Y. Gao, K. Mak, X. Yao, L. Li, A. Szep, D. Walker, J. Hone, T. F. Heinz, and D. Englund, "High-Contrast Electrooptic Modulation of a Photonic Crystal Nanocavity by Electrical Gating of Graphene," *Nano Lett.* **13**, 691-696(2013).

209. E. L. Wooten, K. M. Kissa, A. Yi-Yan, E. J. Murphy, D. A. Lafaw, P. F. Hallemeier, D. Maack, D. V. Attanasio, D. J. Fritz, G. J. McBrien, D. E. Bossi, "A review of lithium niobate modulators for fiber-optic communications systems" *IEEE J. Sel. Top. Quantum Electron.* **6**, 69(2000).

210. A. Liu, R. Jones, L. Liao, D. Samara-Rubio, D. Rubin, D. Cohen, R. Nicolaescu and M. Paniccia, "A high-speed silicon optical modulator based on a metal-oxide-semiconductor capacitor," *Nature* **427**, 615-618(2004).

211. R. S. Jacobsen, K. N. Andersen, P. I. Borel, J. Fage-Pedersen, L. H. Frandsen, O. Hansen, M. Kristensen, A. V. Lavrinenko, G. Moulin, H. Ou, C. Peucheret, B. Zsigri, and A. Bjarklev, "Strained silicon as a new electro-optic material," *Nature* **441**, 199-202(2006).

212. Q. Xu, B. Schmidt, S. Pradhan, and M. Lipson, "Micrometre-scale silicon electro-optic modulator," *Nature* **435**, 325-327(2005).

213. Y. Kuo, Y. Lee, Y. Ge, S. Ren, J. E. Roth, T. I. Kamins, D. A. B. Miller, and J. S. Harris, "Strong quantum-confined Stark effect in germanium quantum-well structures on silicon," *Nature* **437**, 1334-1336(2005).

214. R. A. Shelby, D. R. Smith, and S. Schultz, "Experimental verification of a negative index of refraction," *Science* **292**, 77-79(2001).

215. S. Enoch, G. Tayeb, P. Sabouroux, N. Gu ́erin, and P. Vincent, "A metamaterial for directive emission," *Phys. Rev. Lett.* **89**, 213902(2002).

216. N. Garcia, E. V. Ponizovskaya, and J. Q. Xiao, "Zero permittivity materials: Band gaps at the visible," *Appl. Phys. Lett.* **80**, 1120(2002).

217. R. W. Ziolkowski, "Propagation in and scattering from a matched metamaterial having a zero index of refraction," *Phys. Rev. E, Statist. Nonlinear Soft Matter Phys*. **70**, 046608(2004).

218. M. Silveirinha and N. Engheta, "Tunneling of electromagnetic energy through subwavelength channels and bends using ε-near-zero materials," *Phys. Rev. Lett.* **97**, 157403(2006).

219. R. Liu, Q. Cheng, T. Hand, J. J. Mock, T. J. Cui, S. A. Cummer, and D. R. Smith, "Experimental demonstration of electromagnetic tunneling through an epsilon-near-zero metamaterial at microwave frequencies," *Phys. Rev. Lett.* **100**, 023903(2008).

220. M. Silveirinha and N. Engheta, "Design of matched zero-index metamaterials using nonmagnetic inclusions in epsilon-near-zero materials," *Phys. Rev. B. Condens. Matter Mater. Phys.* **75**, 075119(2007).

221. A. Alù, M. Silveirinha, A. Salandrino, and N. Engheta, "Epsilon-Near-Zero (ENZ) metamaterials and electromagnetic sources: Tailoring the radiation phase pattern," *Phys. Rev. B* **75**, 155410(2007).

222. Z. Lu, and W. Zhao, "Nanoscale electro-optic modulators based on graphene-slot waveguides," *J. Opt. Soc. Am. B* **29**, 1490-1496(2012).

223. H. Brewer and S. Franzen, "Calculation of the electronic and optical properties of indium tin oxide by density functional theory," *Chem. Phys.* **300**, 285-293(2004).

224. A. Melikyan, N. Lindenmann, S. Walheim, P. M. Leufke, S. Ulrich, J. Ye, P. Vincze, H. Hahn, Th. Schimmel, C. Koos, W. Freude, J. Leuthold, "Surface plasmon polariton absorption modulator," *Optics Express* **19**, 8855-8869(2011).

225. V. E. Babicheva, A. V. Lavrinenko, "Plasmonic Modulator Optimized by Patterning of Active Layer and Tuning Permittivity," arXiv:1202.6559v1

226. S. Zhu, G. Q. Lo, and D. L. Kwong, "Electro-absorption modulation in horizontal metal-insulator-silicon-insulator-metal nanoplasmonic slot waveguides," *Appl. Phys. Lett.* **99**, 151114(2011).

227. Z. Lu, W. Zhao, and K. Shi, "Ultracompact electro-absorption modulators based on tunable epsilon-near-zero-slot waveguides," *IEEE Photonics Journal* **4**, 735(2012).

228. G. V. Naik and A. Boltasseva, "A comparative study of semiconductor-based plasmonic metamaterials," *Metamaterials* **5**, 1-7(2011).

229. K. S. Novoselov, A. K. Geim, S. V. Morozov, D. Jiang, Y. Zhang, S. V. Dubonos, I. V. Grigorieva, and A. A. Firsov, "Electric Field Effect in Atomically Thin Carbon Films," *Science* **306**, 666-669(2004).

230. K. S. Novoselov, A. K. Geim, S. V. Morozov, D. Jiang, M. I. Katsnelson, I. V. Grigorieva, S. V. Dubonos, and A. A. Firsov, "Two-dimensional gas of massless Dirac fermions in graphene," *Nature* **438**, 197-200(2005).

231. A. K. Geim, and K. S. Novoselov, "The rise of graphene," *Nat. Materials* **6**, 183-191(2007).

232. X. Du, I. Skachko, A. Barker, and E. Y. Andrei, "Approaching ballistic transport in suspended graphene," *Nat. Nanotechnol.* **3**, 491-495(2008).

233. A. A. Balandin, S. Ghosh, W. Bao, I. Calizo, D. Teweldebrhan, F. Miao, and C. N. Lau, "Superior thermal conductivity of single layer graphene," *Nano Lett.* **8**, 902-907(2008).

234. C. Lee, X. D. Wei, J. W. Kysar, and J. Hone, "Measurement of the elastic properties and intrinsic strength of monolayer graphene," *Science* **321**, 385-388(2008).

235. A. S. Mayorov, R. V. Gorbachev, S. V. Morozov, L. Britnell, R. Jalil, L. A. Pnomarenko, P. Blake, K. S. Novoselov, K. Watanabe, T. Taniguchi, and A. K. Geim, "Micrometer-Scale Ballistic Transport in Encapsulated Graphene at Room Temperature," *Nano Lett* **11**, 2396-2399(2011).

236. Y. M. Lin, C. Dimitrakopoulos, K. A. Jenkins, D. B. Farmer, H. Y. Chiu, A. Grill, and Ph. Avouris, "100-GHz Transistors from Wafer-Scale Epitaxial Graphene," *Science* **327**, 662-662(2010).

237. K. I. Bolotin, K. J. Sikes, Z. Jiang, M. Klima, G. Fudenberg, J. Hone, P. Kim, H. L. Stormer, "Ultrahigh electron mobility in suspended graphene," *Solid State Commun.***146**, 351-355(2008).

238. M. Y. Han, B. Özyilmaz, Y. B. Zhang, and P. Kim, "Energy band-gap engineering of graphene nanoribbons," *Phys. Rev. Lett.* **98**, 206805-206808(2007).

239. Z. Chen, Y. M. Lin, M. J. Rooks, and P. Avouris, "Graphene nano-ribbon electronics," *Physical E* **40**, 228-232(2007).

240. F. N. Xia, D. B. Farmer, Y. M. Lin, and P. Avouris, "Graphene Field-Effect Transistors with High On/Off Current Ratio and Large Transport Band Gap at Room Temperature," *Nano Lett.***10**, 715-718(2010).

241. M. Kim, N. S. Safron, E. Han, M. S. Arnold, and P. Gopalan, "Fabrication and Characterization of Large-Area, Semiconducting Nano perforated Graphene Materials," *Nano Lett.* **10**, 1125-1131(2010).

242. X. G. Liang, Y. S. Jung, S. W. Wu, A. Ismach, D. L. Olynick, S. Cabrini, and J. Bokor, "Formation of bandgap and subbands in graphene nanomeshes with sub-10 nm ribbon width fabricated via nanoimprint lithography," *Nano Lett.* **10**, 2454-2460(2010).

243. J. W. Bai, X. Zhong, S. Jiang, Y. Huang, and X. F. Duan, "Graphene nanomesh," *Nature Nanotechnol.* **5**, 190-194(2010).

244. F. Wang, Y. Zhang, C. Tian, C. Girit, A. Zettl, M. Crommie, and Y. Shen, "Gate-Variable Optical Transitions in Graphene," *Science* **320**, 206-209(2008).

245. F. Xia, T. Mueller, Y. Lin, A. V. Garcia, and P. Avouris, "Ultrafast graphene photodetector," *Nat. Nanotechnol.* **4**, 839-843(2009).

246. T. Ando, Y. Zheng, and H. Suzuura, "Dynamical Conductivity and Zero-Mode Anomaly in Honeycomb Lattices," *J. Phys. Soc. Jpn*, **71**, 1318-1324(2002).

247. M. Liu, X. Yin, E. Ulin-Avila, B. Geng, T. Zentgraf, L. Ju, F. G. Wang, and X. Zhang, "A graphene-based broadband optical modulator," *Nature* **474**, 64-67(2011).

248. M. Furchi, A. Urich, A. Pospischil, G. Lilley, K. Unterrainer, H. Detz, P. Klang, A. M. Andrews, W. Schrenk, G. Strasser, and T. Mueller, "Microcavity-Integrated Graphene Photodetector," *Nano Lett.***12**, 2773-2777(2012).

249. R. R. Nair, P. Blake, A. N. Grigorenko, K. S. Novoselov, T. J. Booth, T. Stauber, N. M. R. Peres, A. K. Geim, "Fine Structure Constant Defines Visual Transparency of Graphene," *Science* **320**, 1308(2008).

250. V. P. Gusynin, S. G. Sharapov, and J. P. Carbotte, "Anomalous Absorption Line in the Magneto-Optical Response of Graphene," *Phys. Rev. Lett.* **98**, 157402-157405(2007).

251. K. Mak, M. Sfeir, Y. Wu, C. Liu, J. A. Misewich, and T. F. Heinz, "Measurement of the Optical Conductivity of Graphene," *Phys. Rev. Lett.* **101**, 196405-196408(2008).

252. F. Bonaccorso, Z. Sun, T. Hasan, and A. C. Ferrari, "Graphene photonics and optoelectronics," *Nature Photonics* **4**, 611-622(2010).

253. X. Wang, L. Zhi, N. Tsao, Z. Tomovic, J. Li, and K. Müllen, "Transparent Carbon Film as Electrodes in Organic Solar Cells," *Angew. Chem.* **47**, 2990-2992(2008).

254. L. G. D. Aroc, Y. Zhang, C. W. Schlenker, K. Ryu, M. E. Thompson, and C. Zhou, "Continuous, Highly Flexible, and Transparent Graphene Films by Chemical Vapor Deposition for Organic Photovoltaic," *ACS Nano* **4**, 2865-2873(2010).

255. V. Yong, J. M. Tour, "Theoretical Efficiency of Nanostructured Graphene-Based Photovoltaics," *Small* **6**, 313-318(2010).

256. N. Yang, J. Zhai, D. Wang, Y. Chen, and L. Jiang, "Two-dimensional graphene bridges enhanced photoinduced charge transport in dye-sensitized solar cells," *ACS Nano* **4**, 887-894(2010).

257. A. B. Kuzmenko, E. Van Heumen, F. Carbone, and D. van der Marel, "Universal Optical Conductance of Graphite," *Phys. Rev. Lett.* **100**, 117401-117404(2008).

258. E. J. H. Lee, K. Balasubramanian, R. T. Weitz, M. Burghard, and K. Kern, "Contact and edge effects in graphene devices," *Nat. Nanotechnol.* **3**, 486-490(2008).

259. F. Xia, T. Mueller, R. G. Mojarad, M. Freitag, Y. Lin, J. Tsang, V. Perebeinos, and P. Avouris, "Photocurrent Imaging and Efficient Photon Detection in a Graphene Transistor," *Nano Lett.* **9**, 1039-1044(2009).

260. T. Mueller, F. Xia, M. Freitag, J. Tsang, and P. Avouris, "Role of contacts in graphene transistors: A scanning photocurrent study," *Phys. Rev. B* **79**, 245430-245435(2009).

261. T. Mueller, F. Xia, and P. Avouris, "Graphene photodetectors for high-speed optical communications," *Nat. Photonics* **4**, 297-301(2010).

262. V. P. Gusynin, and S. G. Sharapov, "Transport of Dirac quasiparticles in graphene: Hall and optical conductivities," *Phys. Rev. B* **73**, 245411(2006).

263. S. Ryu, C. Mudry, A. Furusaki, and A. W. W. Ludwig, "Landauer conductance and twisted boundary conditions for Dirac fermions in two space dimensions," *Phys. Rev. B* **75**, 205344(2007).

264. M. Koshino, and T. Ando, "Magneto-optical properties of multilayer graphene," *Phys. Rev. B* **77**, 115313(2008).

265. T. J. Echtermeyer, L. Britnell, P. K. Jasnos, A. Lombardo, R. V. Gorbachev, A. N. Grigorenko, A. K. Geim, A. C. Ferrari, and K. S. Novoselov, "Strong plasmonic enhancement of photovoltage in graphene," *Nan. Commun.* **2**, 458(2011).

266. Y. Liu, R. Cheng, L. Liao, H. L. Zhou, J. W. Bai, G. Liu, L. X. Liu, Y. Huang, and X. F. Duan, "Plasmon resonance enhanced multicolour photodetection by graphene," *Nat. Commun.* **2**, 579(2011).

267. S. Thongrattanasir, F. H. L. Koppens, and F. J. G. de Abajo, "Complete Optical Absorption in Periodically Patterned Graphene," *Phys. Rev. Lett.* **108**, 047401(2012).

268. H. G. Yan, X. S. Li, B. Chandra, G. Tulevski, Y. Q. Wu, M. Freitag, W. J. Zhu, P. Avouris, and F. N. Xia, "Tunable infrared plasmonic devices using graphene/insulator stack," *Nat. Nanotechnol.* **7**, 220-224(2012).

269. X. Gan, K. F. Mak, Y. Gao, Y. You, F. Hatami, J. Hone, T. F. Heinz, and D. Englund, "Strong Enhancement of Light-Matter Interaction in Graphene Coupled to a Photonic Crystal Nanocavity," *Nano Lett.* **12**, 5626-5631(2012).

270. G. Pirruccio, L. M. Moreno, G. Lozano, and J. G. Rivas, "Coherent and Broadband Enhanced Optical Absorption in Graphene," *ACS Nano* **7**, 4810 (2013).

271. J. M. Dawlaty, S. Shivaraman, J. Strait, P. George, M. Chandrashekhar, F. Rana, M. G. Spencer, D. Veksler, and Y. Chen, "Measurement of the optical absorption spectra of epitaxial graphene from terahertz to visible," *Appl. Phys. Lett*. **93**, 131905 (2008).

272. C. H. Gan, “Analysis of surface plasmon excitation at terahertz frequencies with highly doped graphene sheets via attenuated total reflection,” *Appl. Phy. Lett.* **101**, 111609 (2012).

273. Q. Y., J. Wang, Z. Liu, Z. Deng, X. T. Kong, F. Xing, X. Chen, W. Zhou, C. Zhang, and J. Tian, “Polarization-dependent optical absorption of graphene under total internal reflection,” *Appl. Phy. Lett.* **102**, 021912 (2012).

274. http://grapheneplatform.com/

275. A. C. Ferrari, J. C. Meyer, V. Scardaci, C. Casiraghi, M. Lazzeri, F. Mauri, S. Piscanec, D. Jiang, K. S. Novoselov, S. Roth, and A. K. Geim, “Raman Spectrum of Graphene and Graphene layers,” *Phys. Rev. Lett.* **97**, 187401(2006).

276. J. Christensen, A. Manjavacas, S. Thongrattanasiri, F. H. L. Koppens, F. J. Garc á de Abajo, “Graphene Plasmon Waveguiding and Hybridization in Individual and Paired Nanoribbons,” *ACS Nano* **6**, 431-440(2012).

277. S. Thongrattanasiri, F. H. L. Koppens, and F. J. Garc á de Abajo, “Total Light Absorption in Graphene,” *Arxiv preprint* DOI: arXiv:1106.4460, 2011.

278. L. Wu, H. Chu, W. Koh, E. Li, “Highly Sensitive Graphene Biosensors Based on Surface Plasmon Resonance,” *Opt. Express* **18**, 14395-14400(2010).

279. S. Mikhailov, K. Ziegler, “Nonlinear Electromagnetic Response of Graphene: Frequency Multiplication and the Self-Consistent-Field Effects,” *J. Phys.: Condens. Matter* **20**, 384204(2008).

280. Q. Bao, H. Zhang, Z. Ni, Y. Wang, L. Polavarapu, Z. Shen, Q. H. Xu, D. Y. Tang, K. P. Loh, “Monolayer Graphene as a Saturable Absorber in a Mode-Locked Laser,” *Nano Res.* **4**, 297-307(2011).

281. Q. Bao, H. Zhang, Y. Wang, Z. Ni, Y. Yan, Z. X. Shen, K. P. Loh, and D. Y. Tang, “Atomic-Layer Graphene as a Saturable Absorber for Ultrafast Pulsed Lasers,” *Adv. Funct. Mater.* **19**, 3077-3083(2009).

282. Z. P. Sun, T. Hasan, F. Torrisi, D. Popa, G. Privitera, F. Q. Wang, F. Bonaccorso, D. M. Basko, and A. C. Ferrari, “Graphene Mode-Locked Ultrafast Laser,” *ACS Nano* **4**, 803-810(2010).

283. Q. Bao, K. P. Loh, “Graphene Photoncs, Plasmonics, and Broadband Optoelectronic Devices,” *ACS Nano* **6**, 3677-3694(2012).

284. M. G. Silveirinha and N. Engheta, "Theory of supercoupling, squeezing wave energy, and field confinement in narrow channels and tight bends using ε-near-zero metamaterials," *Phys. Rev. B* **76**, 245109(2007).

285. Q. Xu, V. R. Almeida, and M. Lipson, "Experimental demonstration of guiding and confining light in nanometer-size low-refractive-index material," *Opt. Lett.* **29**, 1626-1628(2004).

286. K. Kim, J. Y. Choi, T. Kim, S. H. Cho, and H. J. Chung, "A role for graphene in silicon-based semiconductor devices," *Nature* **479**, 338-344(2011).

287. R. Yang, M. A. Abushagur, and Z. Lu, "Efficiently squeezing near infrared light into a 21 nm-by-24 nm nanospot," *Opt. Express* **16**, 20142(2008).

288. M. Breusing, C. Ropers, and T. Elsaesser, "Ultrafast carrier dynamics in graphite," *Phys. Rev. Lett.* **102**, 086809(2009).

289. F. Leroy, A. Rousseau, S. Payan, E. Dogheche, D. Jenkins, D. Decoster, and M. Maglione, "Guided-wave electro-optic characterization of $BaTiO_3$ thin films using the prism coupling technique," *Opt. Lett.* **38**, 1037(2013).